

COMPUTATION METHODS FOR APPLIED MECHANICS PROBLEM

Hanfeng Zhai

*Department of Mechanics,
School of Mechanics and Engineering Science, Shanghai University
Shanghai 200444, PRC*

E-mail: Hanfeng.Zhai@outlook.com

This paper contains a series of papers/scientific reports carried out by the author(s) with partial assistantships from other professors/scholars. The paper covers a wide application of studying mechanics with computation methods. For solid mechanics, we study chip mechanical distribution of thermal field based on analytical solutions shown in SECTION I. We thence form the computational algorithms of composite's constitutive model in SECTION II. We also design composite material with high mechanical behavior based on microstructure of enamel and nacre in SECTION III. In SECTION IV, we study how crack propagate on dentin's microstructure. For fluid mechanics problem, we mainly focus on applications of machine learning methods. We predict airfoil noise of NACA 0012 based on decision tree in SECTION V. We also predict the water emptying time of the water discharge problem with neural network in SECTION VI.

CONTENTS

Solid Mechanics Problems

Smartphone chipset estimation in Multiphysics field: **SECTION I**

Constitutive model algorithm for composites: **SECTION II**

Bioinspired structural design of composite materials: **SECTION III**

Fracture study of dentin microstructure: **SECTION IV**

Fluid Mechanics Problems

Machine learning methods on airfoil noise: **SECTION V**

Neural network algorithms for water discharge rate: **SECTION VI**

SECTION I

Thermal estimation of smartphone chipset: mechanical distribution of chipset in Multiphysics field

Abstract

Chipset, a key essence that espouses the function of smartphone. The concentration of this study was to evaluate the thermal effect that was implemented to the chip. Chipset was modeled as a thin plate and bonded by fixed support in the study. The governing equation was reasoned and demonstrated from the eigen-strain in Multiphysics field and constitutive equation. The boundary conditions of the chipset are given according to the physical circumstance in smartphones. Accordingly, coefficients and parameters was given by considering the real materials used in manufacturing. The stresses σ_{xx} and σ_{yy} , and displacements u_{xx} and u_{yy} distribution along the x and y axis is obtained and featured as graphs. The stresses are increasing successively along the x and y axis on chip. The displacements are increasing successively along the x and y axis. The deformed shape of chip under thermal effect is kindred to a trapezoid. A graphical distribution and numeral solution could be obtained by using finite element method. The stresses and displacements generally unevenly distributed in chip based on the simulation. Several possible optimization methods is discussed. These insights could provide guidelines for engineering and manufacturing of smartphone chip.

Keywords: smartphone chip; Multiphysics problem; finite element method; thermal analysis; stress field

Introduction

Smartphones are widely used and applied nowadays. With the growing trends of pursuing higher running speed with bigger storage, high functional and integrative chipset is required. Howbeit if the demand beyond the limitation of Strong heat flux and thermal displacement might seriously nullify the chip. Therefore, estimate the thermal effect that has implemented on chipset in smartphones' mechanical field is extremely important.

The thermal effect of chip has long been discussed and studied by scholars. Tang *et al.* [1] studied the thermal effect of chip's power enlarging functions observed through infrared rays. Liao *et al.* [2] concluded that Performance is affected by both temperature and supply voltage because of the temperature and voltage dependence of circuit delay through study the factors that may induce thermal runaway and leakage power and estimated the possible effects. Qian *et al.* [3] did an accurate and efficient thermal analysis for a VLSI chip is crucial, both for sign-off reliability verification and for design-time circuit optimization. Liang *et al.* [4] carried out a hybrid random walk method is proposed for the thermal analysis of integrated circuits.

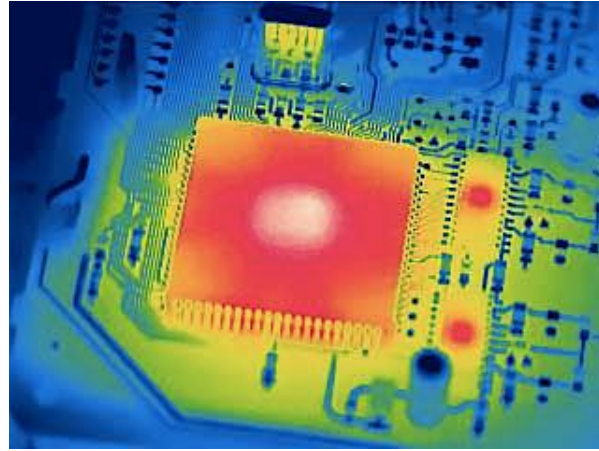


Fig. 1 Thermal image of chip under thermal field.

While when it comes to the mathematical estimation and simulation of the thermal loading on chip, Guo *et al.* [5] Aiming at the problem of local high-temperature thermal effects in large-scale IC chips, and developed a technique for thermal analysis of the chip using a random walk algorithm is proposed. Tang *et al.* [6] presented a present a hybrid algorithm to compute the convex hull of points in three or higher dimensional spaces through uses a GPU-based interior point filter to cull away many of

the points that do not lie on the boundary. Plus, Ma *et al.* [7] also Aiming at the problem of local high-temperature thermal effects in large-scale IC chips, howbeit they proposed a grid-based random walk method to analyze the steady-state temperature distribution. Their algorithm only calculates the points near the heat source, thus the method greatly reduced the amount of calculation. Also, techniques based on the domain decomposition method (DDM) are presented for the 3-D thermal simulation of nonrectangular IC thermal model including heat sink and heat spreader by Yu *et al.* [8]. Zhan *et al.* [9] present three highly efficient thermal simulation algorithms for calculating the on-chip temperature distribution in a multilayered substrate structure.

Moreover, many scientists and scholars tried to experimentally analysis of the chip thermal process. Yu *et al.* [10] studied smartphone chipset's thermal performance not only by finite element simulation but also carried out experiments to reflect the thermal process of chip. Le *et al.* [11] describe the implementation of the IBM POWER6™ microprocessor, a two-way simultaneous multithreaded (SMT) dual-core chip whose key features include binary compatibility with IBM POWER5™ microprocessor-based systems. They tested several properties of the chip and concluded that Key extensions to the coherence protocol enable POWER6 microprocessor-based systems to achieve better SMP scalability while enabling reductions in system packaging complexity and cost. In fine, the thermal effect of smartphone chip is at the central topic which attracted many scholars and studies.

Method

1. Mathematical Model

When loaded under Multiphysics field, the particle is undergoing both mechanical and non-mechanical effects. Therefore, estimating both these effects on materials requires both mechanics and physics field governing equations. In this problem, the chipset is modelled as a thin plate loaded under thermal field and bounded at the bottom side. The chipset model is simplified as below, where the heat is caused by battery.

Initially, converting the thermal effect into mechanical effect requires a mechanical tensor called the eigen-strain, which includes both the effects of volumetric and expansion strain due to physic field. Consequently, the thermal boundary conditions could be deduced and substitute it into the heat equation could reason the curvature of the plate. Subsequently, given the mechanical boundary conditions and substitute it

into the Constitutive equation could reason the form of stress and displacement. By superpose the eigen-strain into the solution, the form of stresses and displacements are concluded.

1) Eigen-strain:

Eigen-strain consists of two parts: volumetric strain and expansion strain. Volumetric strain: the materials' volume change under free-standing condition

$$\varepsilon_V = \frac{\Delta V}{V_0} = \alpha(T - T_0)$$

Where α is called the volumetric thermal expansion coefficient. T_0 is the initial temperature.

Expansion strain: the materials' expansion or shrink caused by change of temperature.

$$\varepsilon_{11} = \alpha_{11}(T - T_0), \quad \varepsilon_{ij} = \alpha_{ij}(T - T_0).$$

for isotropic material: $\alpha_{11} = \alpha_{22} = \alpha_{33} = \frac{1}{3}\alpha$. We may name these strains induced by physical variables other than the stress the eigen-strain, denoted by ε^* , ε_{ij}^* . It is the strain caused by physical changes under stress-free condition.

2) Heat equation:

For thermal field, the relationship between temperature and time is

$$\frac{\partial T}{\partial t} - \frac{k}{\rho c_p} \nabla^2 T = 0$$

where c_p is the specific heat capacity, ρ is the mass density of the material and k is the thermal conductivity.

In this case, the temperature boundary condition of chipset could be given

- i) Temperature on boundary: $T = -5000 \cdot y + 345.15$ [K] on S
- ii) Heat flux boundary condition: $\frac{\partial T}{\partial n} = 0$, on S

iii) Convection boundary condition (Newton boundary condition):

$$\frac{\partial T}{\partial n} = h(T - T_0) \text{ on } S, \text{ where } h \text{ is film coefficient, } T_0 = 295.15\text{K}$$

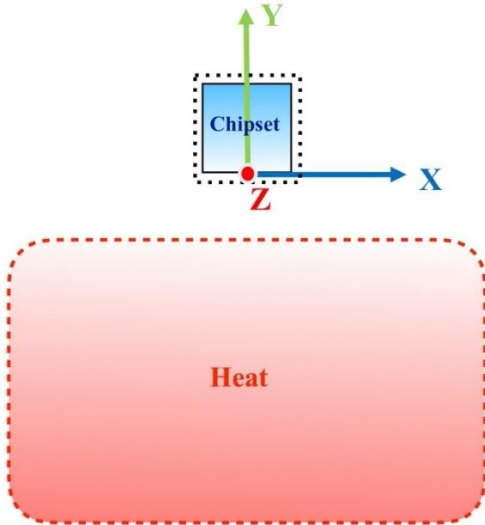


Fig. 2 The mechanical model of smartphone chipset physics, where the heat is created by the exothermic process of battery. In the mechanical model, the battery thermal field is considered as a semi-infinite heating source.

3) Constitutive equations

Considering the Multiphysics field, Hooke's law for elastic mechanical displacements needs to be generalized to consider eigen-strain which is caused by other physical variables.

For smartphones' chipset, a thin plate is loaded in multiaxial state, where

$$\sigma_{ij} \neq 0 \quad (i,j = 1,2,3)$$

$$\left\{ \begin{array}{l} \varepsilon_{11} = \frac{1}{E} \sigma_{11} - \frac{1}{E} \sigma_{22} - \frac{1}{E} \sigma_{33} + \frac{1}{3} \alpha(T - T_0) \\ \varepsilon_{22} = \frac{1}{E} \sigma_{22} - \frac{1}{E} \sigma_{11} - \frac{1}{E} \sigma_{33} + \frac{1}{3} \alpha(T - T_0) \\ \varepsilon_{33} = \frac{1}{E} \sigma_{33} - \frac{1}{E} \sigma_{22} - \frac{1}{E} \sigma_{11} + \frac{1}{3} \alpha(T - T_0) \\ \varepsilon_{12} = \frac{1}{2G} \sigma_{12} \\ \varepsilon_{13} = \frac{1}{2G} \sigma_{13} \\ \varepsilon_{23} = \frac{1}{2G} \sigma_{23} \end{array} \right.$$

which could be simplified as

$$\varepsilon_{ij} = \frac{1+\nu}{E} \sigma_{ij} + \frac{\nu}{E} \sigma_{kk} \delta_{ij} + \varepsilon_{ij}^*$$

where $\varepsilon_{ij}^* = \frac{1}{3} \alpha(T - T_0) \delta_{ij}$.

Thence, substitute strain and eigen-strain into Hooke's law, one could obtain the stress components in terms of strain components:

$$\sigma_{ij} = 2G(\varepsilon_{ij} - \varepsilon_{ij}^*) + \frac{Ev}{(1+\nu)(1-2\nu)} (\varepsilon_{kk} - \varepsilon_{kk}^*)$$

Boundary Condition:

Mechanical condition:

- i) Displacement boundary condition: $u_i = 0$ on S_n
- ii) Traction boundary condition: $\sigma_{ji} n_j = 0$ on S_n

The simplified model of the chipset is shown as below in Figure 3.

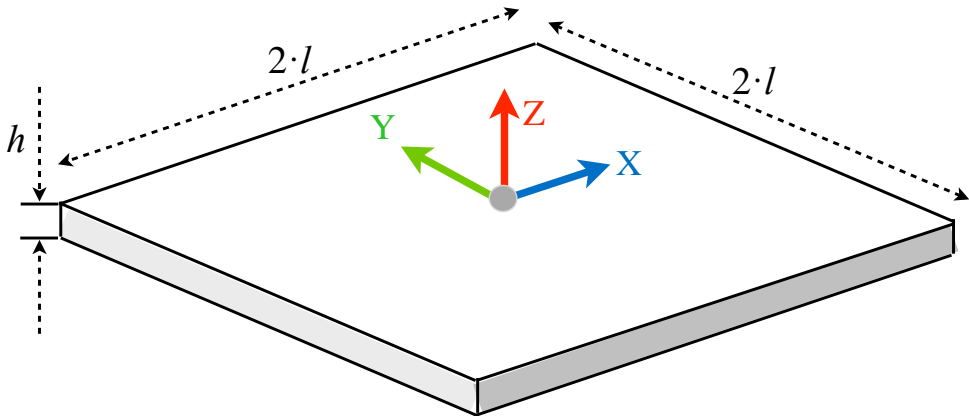


Fig. 3 The size parameters and three-dimensional simplified model of the chipset, where $l=0.005\text{m}$, $h=0.001\text{m}$.

Based on the given boundary conditions, it could be induced that in thermal field:

$$\sigma_{yy} \neq \sigma_{xx} \neq 0;$$

$$\sigma_{zz} = \sigma_{xy} = \sigma_{yz} = \sigma_{xz} = 0;$$

Therefore, the eigenstrain could be deduced:

$$\varepsilon_{zz} = -\frac{\nu}{E}\sigma_{xx} - \frac{\nu}{E}\sigma_{yy} + \varepsilon_{zz}^*$$

$$\varepsilon_{xx} = \varepsilon_{x0} + \kappa y$$

$$\varepsilon_{yy} = \varepsilon_{y0} + \kappa y$$

Thence, we could give the form of σ_{xx} and σ_{yy} :

$$\begin{aligned}\sigma_{xx} &= \frac{E}{1+\nu}(\varepsilon_{xx} - \varepsilon_{xx}^*) + \frac{Ev}{(1+\nu)(1-2\nu)}(2\varepsilon_{xx} - \frac{\nu}{E}\sigma_{xx} - \frac{\nu}{E}\sigma_{yy} - 2\varepsilon_{xx}^*) \\ \sigma_{yy} &= \frac{E}{1+\nu}(\varepsilon_{yy} - \varepsilon_{yy}^*) + \frac{Ev}{(1+\nu)(1-2\nu)}(2\varepsilon_{yy} - \frac{\nu}{E}\sigma_{xx} - \frac{\nu}{E}\sigma_{yy} - 2\varepsilon_{yy}^*)\end{aligned}$$

Consequently, we substitute the above simultaneous equations:

$$\begin{aligned}\sigma_{xx} &= \frac{E - Ev - Ev^2}{(1-\nu^2)(1-2\nu)}(\varepsilon_{xx} - \varepsilon_{xx}^*) - \frac{Ev^2}{(1-\nu^2)(1-2\nu)}(\varepsilon_{yy} - \varepsilon_{yy}^*) \\ \sigma_{yy} &= \frac{E - Ev - Ev^2}{(1-\nu^2)(1-2\nu)}(\varepsilon_{yy} - \varepsilon_{yy}^*) - \frac{Ev^2}{(1-\nu^2)(1-2\nu)}(\varepsilon_{xx} - \varepsilon_{xx}^*)\end{aligned}$$

Based on the strains, one could also obtain the displacement:

$$u_{ij} = \int \varepsilon_{ij} dx_i$$

Subsequently, in order to simplified the calculation process, we name $\frac{E-Ev-Ev^2}{(1-\nu^2)(1-2\nu)}$ as A , $\frac{Ev^2}{(1-\nu^2)(1-2\nu)}$ as B .

The traction-free boundary conditions on two side faces have been satisfied automatically. Since we focus on the eigen-strain induced stress which does not include the effect of external mechanical loading the end of plate is mechanically free and the mechanical boundary conditions could be specified as

$$\int_{-l}^l \sigma_{xx} dy = 0, \int_{-l}^l \sigma_{yy} dy = 0$$

$$\int_{-l}^l \sigma_{yy} y dy = 0$$

Substitute the above form of σ_{xx} and σ_{yy} into the boundary conditions:

$$A \cdot 2l \cdot \varepsilon_{y0} - A \cdot \int_{-l}^l \varepsilon_{yy}^* dz - B \cdot 2l \cdot \varepsilon_{x0} + B \cdot \int_{-l}^l \varepsilon_{xx}^* dz = 0$$

$$A \cdot 2l \cdot \varepsilon_{x0} - A \cdot \int_{-l}^l \varepsilon_{yy}^* dz - B \cdot 2l \cdot \varepsilon_{y0} + B \cdot \int_{-l}^l \varepsilon_{xx}^* dz = 0$$

$$A \cdot \int_{-l}^l (\varepsilon_{y0} + \kappa y) y dy - A \cdot \int_{-l}^l \varepsilon_{yy}^* y dy - B \cdot \int_{-l}^l (\varepsilon_{x0} + \kappa y) y dy + B \cdot \int_{-l}^l \varepsilon_{xx}^* y dy = 0$$

In order to simplify the calculation process, we elicit the given forms:

$$A \cdot 2h = m, B \cdot 2h = n$$

By solving the above equations, we could obtain the parameters in the equations:

$$\varepsilon_{x0} = \frac{A - B}{m - n} \left(\int_{-l}^l \varepsilon_{xx}^* dy + \int_{-l}^l \varepsilon_{yy}^* dy \right) - \varepsilon_{y0}$$

$$\begin{aligned} \varepsilon_{x0} &= \frac{A - B}{m - n} \left(\int_{-l}^l \varepsilon_{xx}^* dy + \int_{-l}^l \varepsilon_{yy}^* dy \right) - \frac{A}{m + n} \int_{-l}^l \varepsilon_{yy}^* dy \\ &\quad + \frac{B}{m + n} \int_{-l}^l \varepsilon_{xx}^* dy - \frac{(A - B)n}{m^2 - n^2} \left(\int_{-l}^l \varepsilon_{xx}^* dy + \int_{-l}^l \varepsilon_{yy}^* dy \right) \end{aligned}$$

$$\varepsilon_{y0} = \frac{A}{m + n} \cdot \int_{-l}^l \varepsilon_{yy}^* dy - \frac{B}{m + n} \int_{-l}^l \varepsilon_{xx}^* dy + \frac{(A - B)n}{m^2 - n^2} \left(\int_{-l}^l \varepsilon_{xx}^* dy + \int_{-l}^l \varepsilon_{yy}^* dy \right)$$

$$\kappa = \frac{3(A \cdot \int_{-l}^l \varepsilon_{yy}^* y dy - B \cdot \int_{-l}^l \varepsilon_{xx}^* y dy)}{(A - B) \cdot 2h^3}$$

Hence, the stress σ_{xx} and σ_{yy} is obtained.

Now we substitute the eigen-strain $\varepsilon_{xx}^*(z) = \frac{1}{3} \alpha T(z)$, $\varepsilon_{yy}^*(z) = \frac{1}{3} \alpha T(z)$, we have

$$\varepsilon_{x0} = \frac{\alpha}{3h} \int_{-l}^l T(y) dy + \frac{\alpha(B-A)}{6h(A+B)} \int_{-l}^l T(y) dy - \frac{\alpha B}{3h(A+B)} \int_{-l}^l T(y) dy$$

$$\varepsilon_{y0} = \frac{\alpha(A-B)}{6h(A+B)} \cdot \int_{-l}^l T(y) dy + \frac{\alpha B}{3h(A+B)} \int_{-l}^l T(y) dy$$

$$\kappa = \frac{\alpha \cdot \int_{-l}^l T(y) y dy}{2h^3}$$

Therefore, the final form of the stress is reasoned by substitute ε_{x0} , ε_{y0} , κ into the equation of stress and displacement.

Subsequently, substitute the given temperature and coefficients into the stress and displacement.

Temperature: $T(y) = -5000y + 345.15$ [K]

Volumetric thermal expansion coefficient: $\alpha(\text{Si}) = 5.8 \times 10^{-7}$ [1/K]

For silicon (100) and (110), Young's modulus varies from 130.2 GPa to 187.5 GPa, Poisson's ratio varies from 0.064 to 0.361. Therefore, we let $E(\text{Si}) = 150$ [GPa] and $\nu(\text{Si}) = 0.1$.

The results is obtained by substituting these coefficients.

2. Finite Element Simulation

To analyzing this problem more comprehensively and better observing the mechanical change of the chipset, operating a numerical simulation based on ANSYS could offer a reference on the given calculation. To estimate the details more accurately, I model the major structures of battery, screen, and circuit board to bond with the chipset. In the modelling, the material for battery is Copper; the material for circuit board is High Polymer (a kind of plastic); the material for screen is glass; the material for chipset is Silicon. The model is shown in Figure 4.

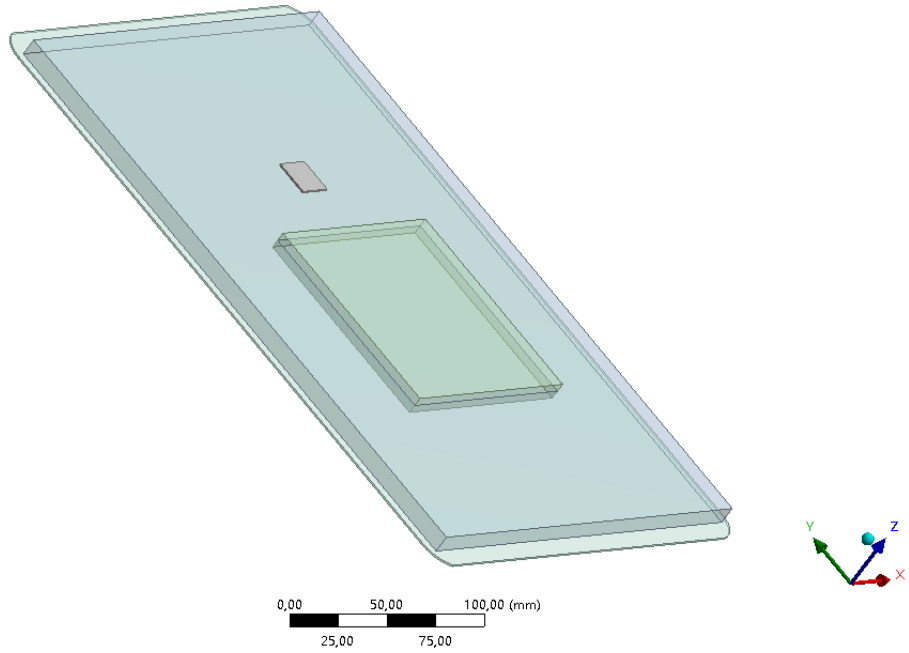


Fig. 4 The modelling of the chipset and its corresponding parts in smartphone. The bottom part is smartphone's screen. The large cuboid is the circuit board. The small cuboid is the battery. The small slice is the chipset.

Results

1. Mechanical Variables

As it is shown in the former chapter, after substituting the results of strain, eigenstrain and curvature into the form of the stress and displacement, the final results of these mechanical variables is deduced. Howbeit due to the form of the results is complex and cannot be written as algorithm forms, featuring these variables as graphs is more intuitive and clearheaded.

Initially, the high temperature of the battery in the smartphone is considered as a semi-infinite thermal field. For areas surround the chipset, the thermal field is considered as a successively decreasing temperature, where the schematic diagram is shown in Figure 5, the graph is shown in Figure 6.

After substitute the temperature equations into the stress and displacement equations, graphical features and the two stresses σ_{xx} and σ_{yy} along the y axis is shown in Figure 8(a), and the separate graphs of each stresses is shown in Figure 8(b).

Temperature Distribution

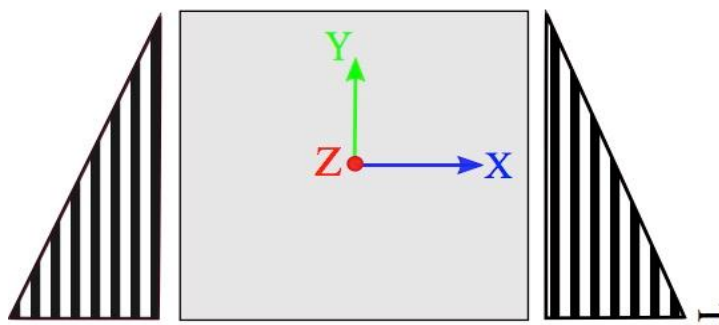


Fig. 5 The temperature distribution along the chipset when loaded under the thermal effect of smartphone battery. In this problem, the temperature function is considered as a linear equation ($T(y) = -5000 \cdot y + 345.15$ [K]) of y axis to temperature.

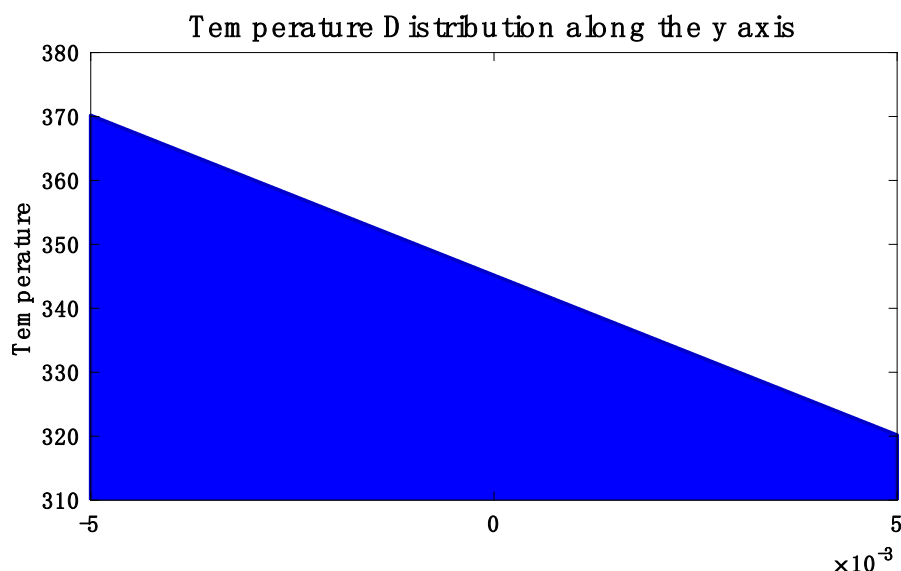


Fig. 6 The plotted graph of y axis to temperature.

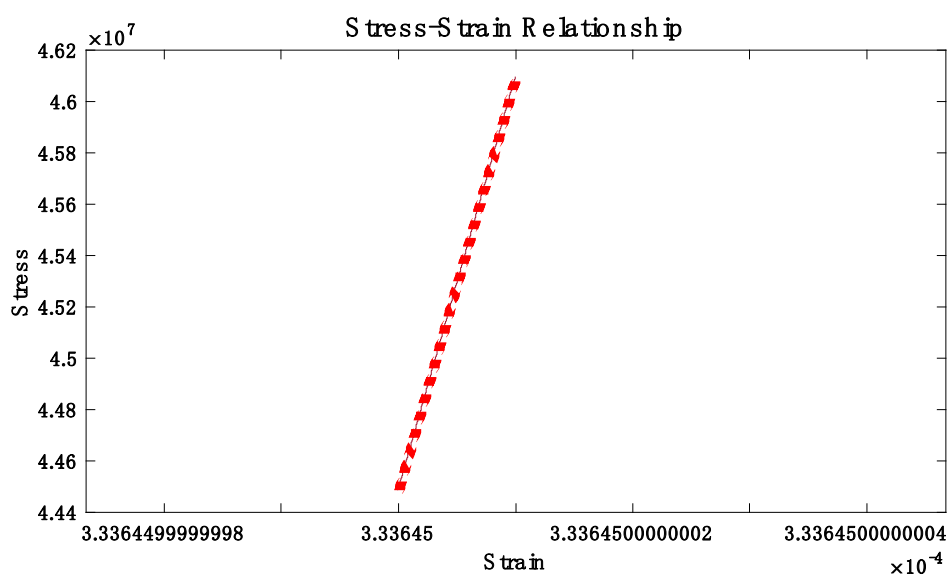


Fig. 7 The stress-strain diagram representing the constitutive equation.

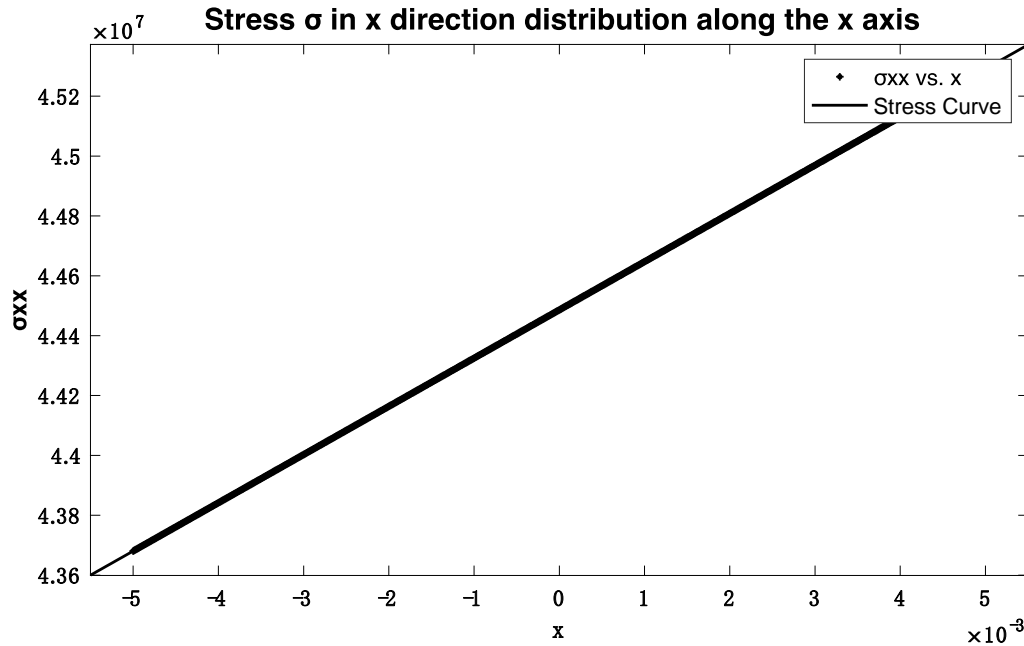


Fig. 8 (a) Relationship of stress σ_{xx} to x axis.

As it is shown in Figure 8(a) and (b), the stress shows a linear relation with the distribution axis, which shows that stress is growing along the chip.

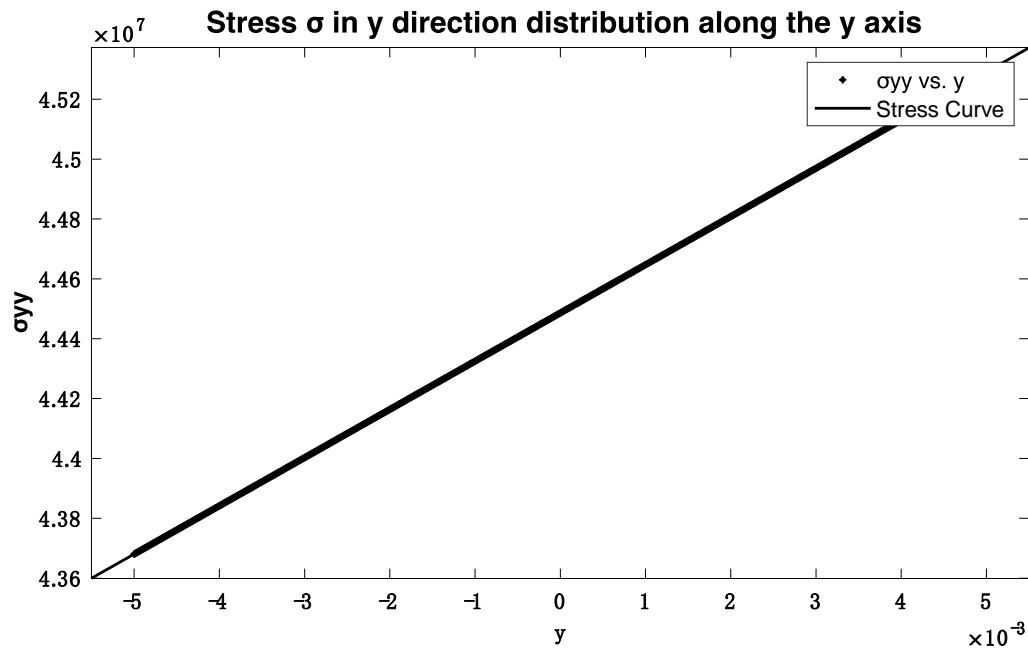


Fig. 8 (b) Relationship of stress σ_{yy} to y axis.

Stress σ_{xx} distribution along the chip

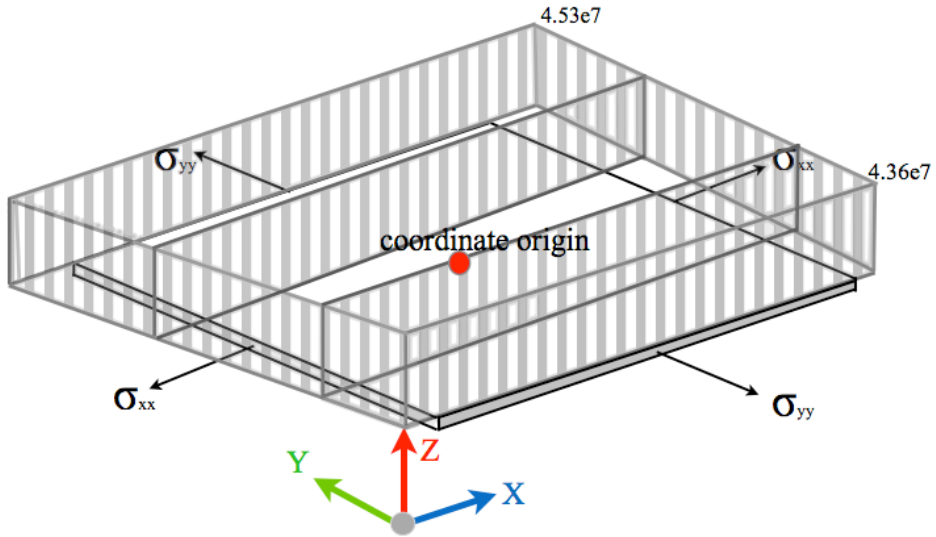


Fig. 8 (c) The distribution of stress σ_{xx} on smartphone chip.

Stress σ_{yy} distribution along the chip

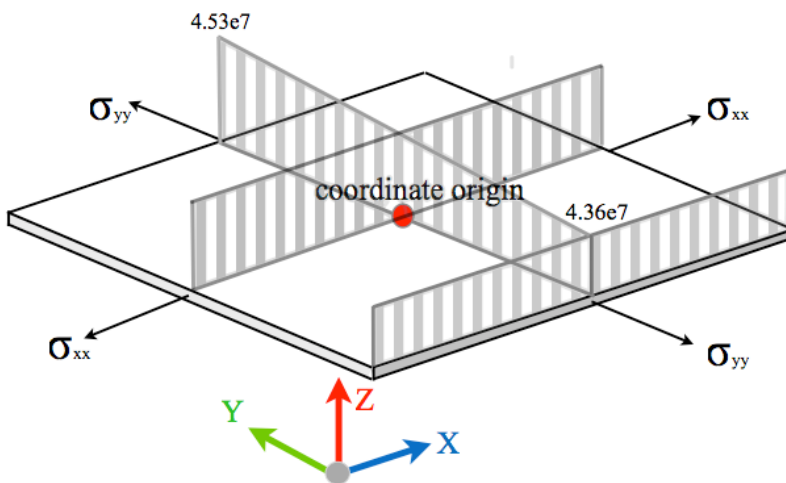


Fig. 8 (d) The distribution of stress σ_{yy} on smartphone chip.

From the figures obtained one can deduce that the stresses σ_{xx} and σ_{yy} along the y axis are both increasing successively. In the shown graphs and calculated equations, one knows that stress σ_{xx} and σ_{yy} remains a constant on x axis and satisfy a linear relation with the y axis. From the obtained diagram one could plot the stress σ_{xx} and σ_{yy} distribution on the smartphone chip, respectively [Figure 8(c) and Figure 8(d)].

Similar to the stresses, the displacement could also be calculated through substituting the strain into strain-displacement relation $u_{ij} = \int \varepsilon_{ij} dx_i$. The graphical feature of the two displacements are shown as below. Based on equation given above: $\varepsilon_{xx} = \varepsilon_{x0} + \kappa y$, $\varepsilon_{yy} = \varepsilon_{y0} + \kappa y$. We obtain that the both the strain in x direction and y direction satisfies a linear relation with variable y. Thence through integration we deduce that the displacement in x direction is a function consists of both variables x and y. Simultaneously, the displacement in y direction obeys a quadratic relation. By featuring the two displacements u_{xx} and u_{yy} one could deduce that the two displacements are following the same trend. They both initiated with the negative values and values zero at the central point and increasing successively.

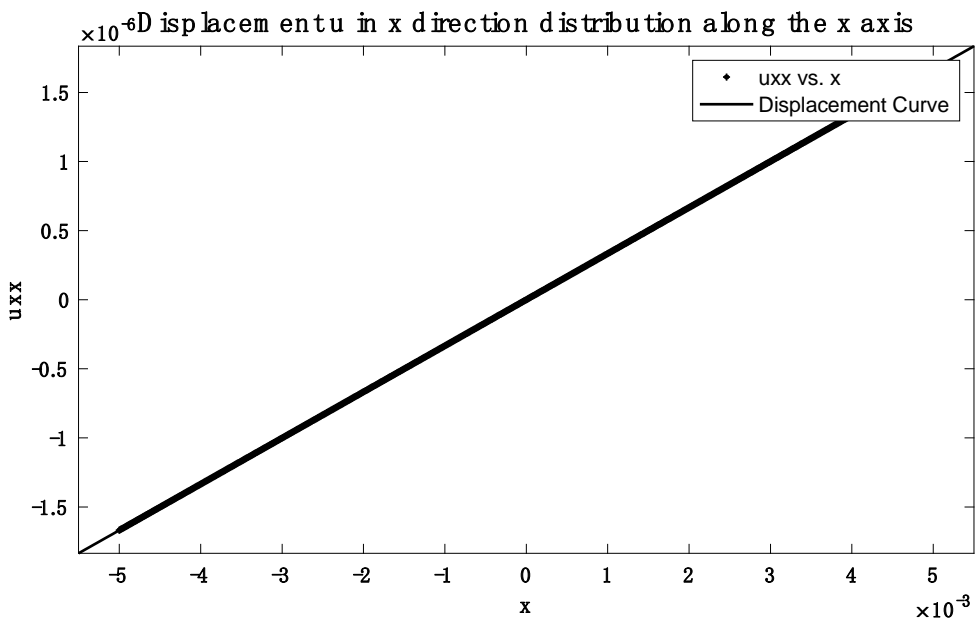


Fig. 9 (a) Relationship of stress u_{xx} to x axis.

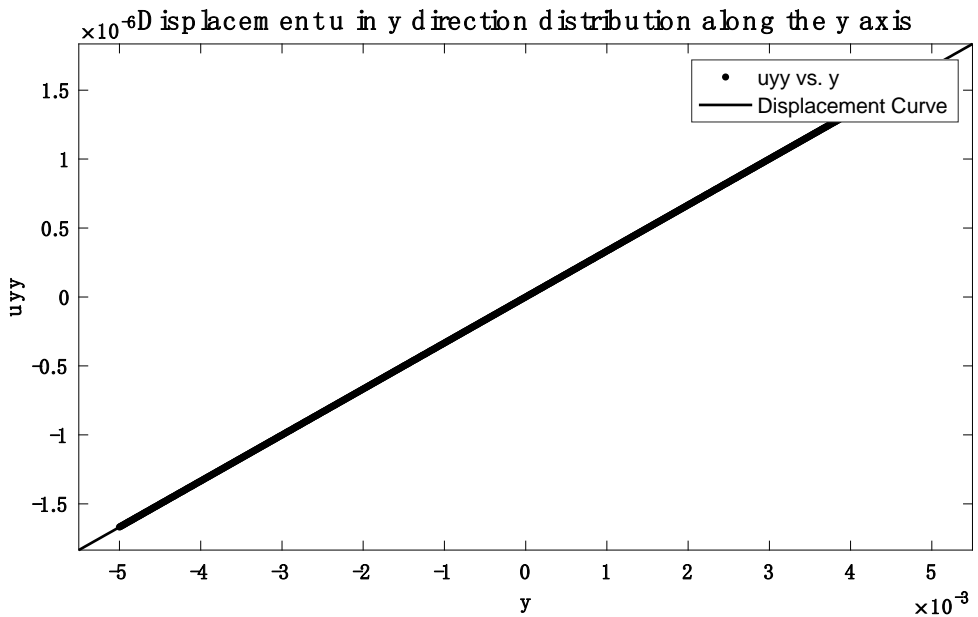
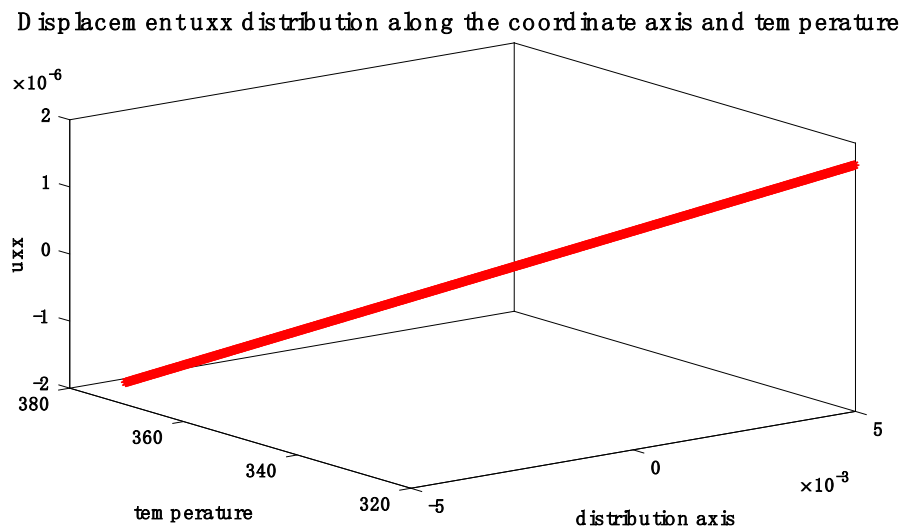
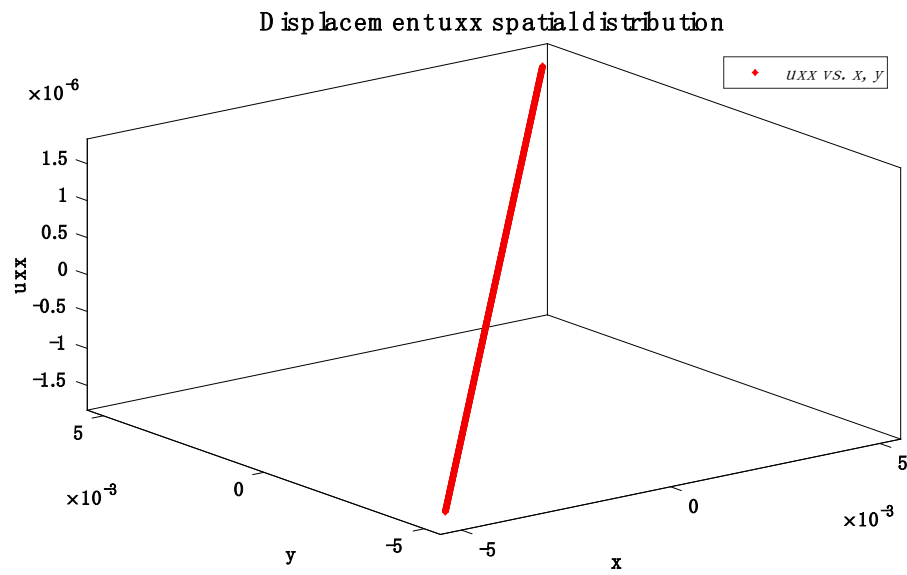


Fig. 9 (b) Relationship of stress u_{yy} to y axis.

Based on the equation calculated from the integration and deducing mentioned before one could plot the displacement diagrams as shown in Figure 9(a) and (b). Plus, a three-dimensional relation of the displacements to the axis and temperature [Figure 9(c)] and displacements to the two axes [Figure 9(d)].

**Fig. 9 (c)** Relationships between displacement to the distribution axis (x or y) and temperature.

ture.

Fig. 9 (d) The spatial distribution of the displacement u_{xx} .

Based on the plot diagrams containing relations between displacement u_{xx} and u_{yy} to the two axes we could build schematic view of displacement distribution on the smartphone chip as shown in Figure 9(e) and Figure 9(f).

Displacement u_{xx} distribution along the chip

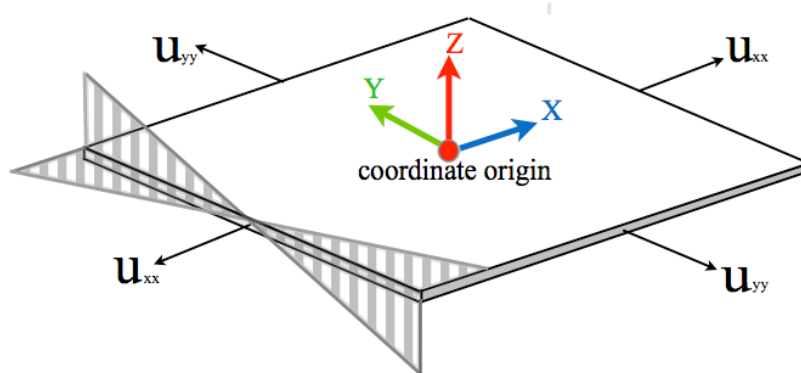


Fig. 9 (e) The distribution of displacement u_{xx} on smartphone chip.

Displacement u_{yy} distribution along the chip

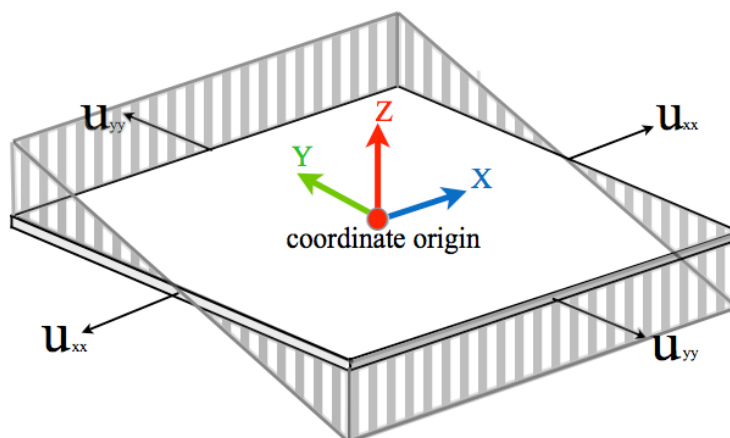


Fig. 9 (f) The distribution of displacement u_{yy} on smartphone chip.

2. Finite Element Estimation

As it is modelled in Figure 4, we set the temperature of the battery is 70°C (345.15K) and simulate both the temperature field, stress and displacement field. The results is shown is Figure 10(a), Figure 10(b), Figure 10(c).

According to the simulation results shown above, one could obtain that from the interaction of the temperature, the chip temperature is generally higher than its surrounding circuit board. The temperature of the chip is around 25°C to 30°C, which is not a high considering the heat of the battery.

From the result of stress, one could observe that the stress is not evenly distributed along the chip, where the central part has generally higher stress value than the chip's edge. Along the y axis, the stress on lower part is trivially higher than the stress on higher part, which correspond perfectly to the calculation results. The stress value is around 2.3×10^7 Pa.

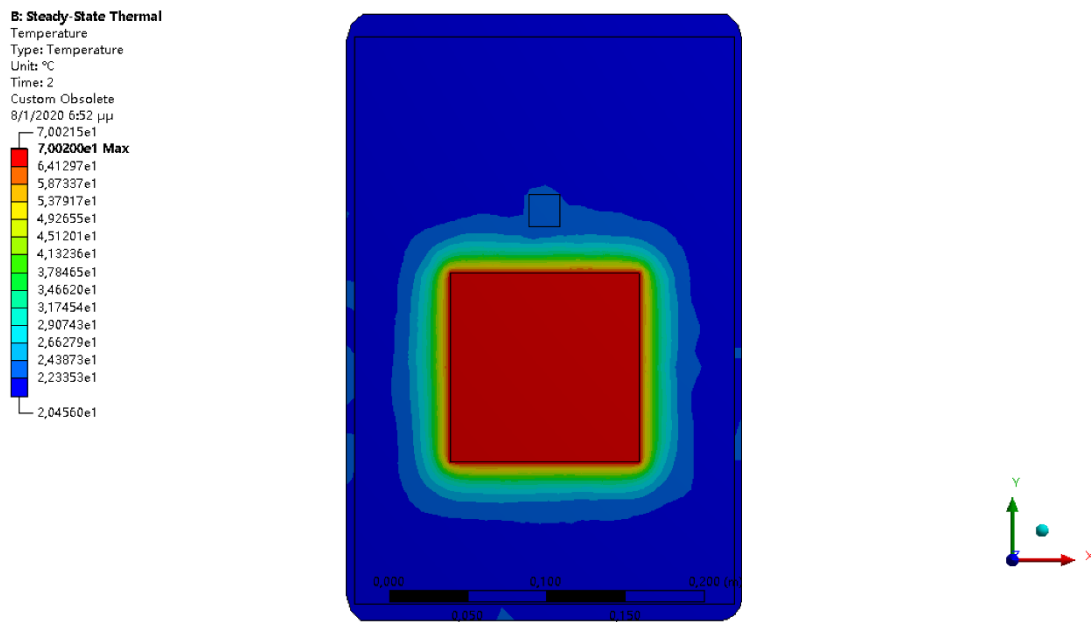


Fig. 10 (a) The temperature distribution of simulation in smartphones when battery is set to be at 345.15K.

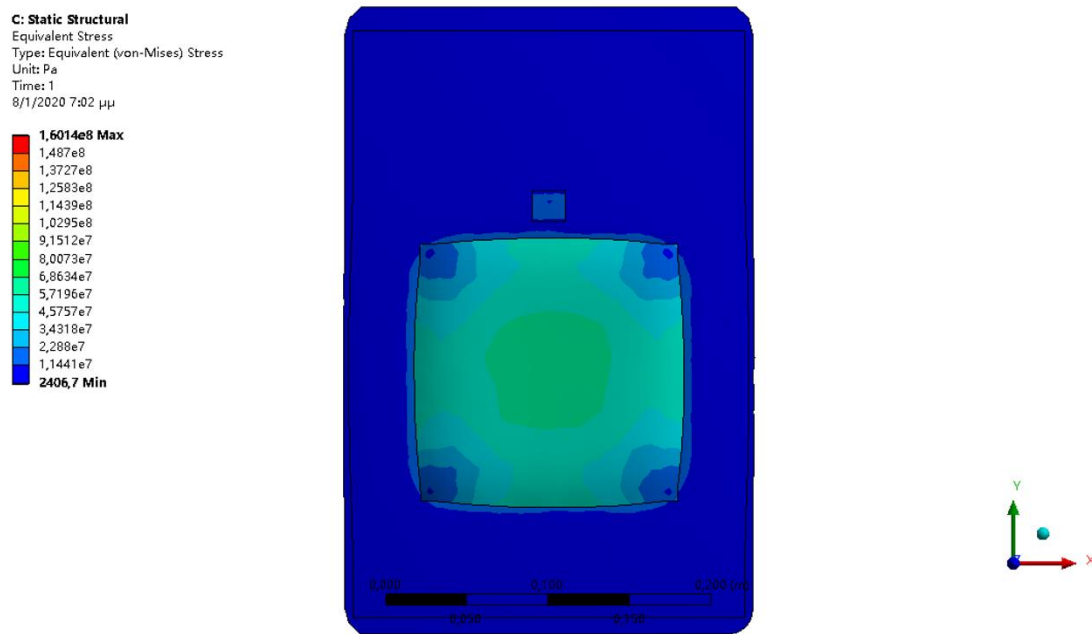


Fig. 10 (b) The stress distribution of simulation in smartphones when battery is set to be at 345.15K.

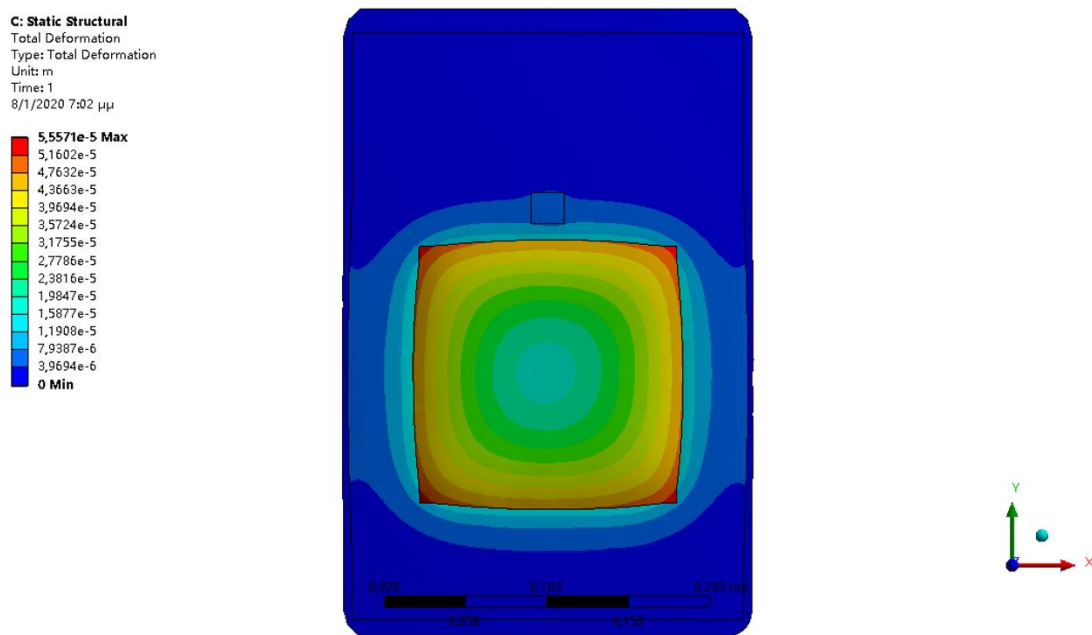


Fig. 10 (c) The displacement distribution of simulation in smartphones when battery is set to be at 345.15K.

From the displacement results, one can obtain that the displacement is not uniformly distributed along the y axis, where the value is around 3.96×10^{-6} m. The deformed shape looks like a trapezoid, which shows that the chip tends to extend its volume when encounters higher temperature.

Conclusion

In determining the stress and displacement of smartphone chipset, I assume the temperature distribution is a linear equation along the y axis, where the equation is $T = -5000 \cdot y + 345.15$ [K]. The mathematical solution of the stresses and displacement is obtained through substitute the strain and eigen-strain into the heat equation and constitutive equation. By implementing the thermal load into the stress and displacement results calculated, one could plot the stress-x, stress-y and displacement-x, displacement-y diagrams [Figure 8(a), (b). Figure9(a), (b)]. Furthermore, schematic view of stresses distribution on smartphone chip is given based on graphs [Figure 8(c), (d)]. A spatial distribution of displacement u_{xx} to temperature and axis [Figure 9(c)] and the spatial distribution of u_{xx} [Figure 9(d)] can be plotted. Similarly, schematic views showing the displacements distribution on smartphone chip is given based on the calculated results [Figure 9(e) and Figure 9(f)].

From the simulation, one could model the chip bonded with circuit board and battery, screen. The simulation results shows that chip temperature is approximately 25–30°C when battery is 70°C.

Based on the simulation results, the stress is not uniformly distributed along the y axis on chip, which corresponds to the mathematical result. the stress value on chip is approximately 2.3×10^7 Pa [Figure 10(b)]. The displacement is also not uniformly distributed along the y axis, where the displacement value is approximately 3.96×10^{-6} m [Figure 10(c)]. Through enlarging the schematic view of the chip, one could observe that the deformed shape of the chip is kindred to a trapezoid.

Discussion

In real situation, there are a significant amount of nanoscale or microscale circuits, including memory cells and sensing circuitry that carved on the chip. These connections proffer the hardware to support the smartphone functions. What's more, these circuits are extremely sensitive for changes of its physical circumstances.

Based on stress results, one could observe that stresses increase successively along the x and y axis following a linear relation. To prevent dysfunction caused by the relatively high temperature, several optimizations could be carried out for chip such as adding a thermal segregation layer in chip, using materials that resist suppression on x axis howbeit resist extension on y axis, etc.

Based on displacement results, one could observe that displacements also increase successively along the x and y axis, in which the displacement in x direction satisfy a linear relation and displacement in y direction satisfy a quadratic relation. Similar to stress estimation, one could also carry out several actions to optimize the chip such as make small changes on the original shape of chip to prevent possible displacement caused by temperature change, using anisotropic materials as mentioned in the last paragraph, etc.

Eventually, specific optimization method should be advised from people who expert in electronic engineering based on these results. From the mechanic's perspective, I could only offer reasonable conjecture based on the results. These results could provide reference in smartphones' chips design and manufacturing.

References

- [1] Tang Sha, Wang Zhihe, Chen Yongfan. Discussion on infrared thermal analysis of power amplifier chip. Reliability and Environmental Tests of Electronic Products, 2019, 37(05):63-67.
- [2] Weiping Liao, Lei He, K.M. Lepak Temperature and supply Voltage aware performance and power modeling at microarchitecture level. IEEE Transactions on Computer-Aided Design of Integrated Circuits and Systems, 2005, Vol.24 (7), pp.1042-1053
- [3] Haifeng Qian, Sachin S. Sapatnekar, Eren Kursun. Fast poisson solvers for thermal analysis. ACM Transactions on Design Automation of Electronic Systems (TODAES). 2012(3)
- [4] Liang Yuan,Yu Wenjian,Qian Haifeng. A hybrid random walk algorithm for 3D thermal analysis of integrated circuits. Proc of Asia and South Pacific Design Automation Conference. 2014
- [5] Guo Jun, Dong Sheqin. Application of Random Walk Algorithm in Thermal Analysis of IC Chip[J]. Journal of Computer-Aided Design and Computer Graphics, 2010, 22(04):689-694.
- [6] Min Tang, Jie-yi Zhao, Ruo-feng Tong, Dinesh Manocha. GPU accelerated convex hull computation[J]. Computers & Graphics, 2012, 36(5).
- [7] Ma.J, Xu.N. Research on GPU Thermal Analysis Method Based on GPU[J]. Application Research of Computers, 2018, 35(03):773-776.
- [8] Yu Wenjian, Zhang Tao,Yuan Xiaolong,et al. Fast 3D thermal simulation for integrated circuits with domain decomposition method. IEEE Transcations on Computer Aided Design of Integrated Circuits and Systems. 2013
- [9] Zhan, Yong, Sapatnekar, Sachin S. High-efficiency green function-based thermal simulation algorithms.IEEE Transactions on Computer Aided Design of Integrated Circuits and Systems. 2007
- [10] Youmin Yu, Nader Nikfar, Todd Sutton, Impact of Chipset Configuration on Thermal Performance of Smartphones, 2018 17th IEEE Intersociety Conference on Thermal and Thermomechanical Phenomena in Electronic Systems (ITherm)
- [11] Le, Hung Q,Starke, William J.,Fields, J. Stephen,O'Connell, Francis P.,Nguyen, Dung Q.,Ronchetti, Bruce J.,Sauer, Wolfram M.,Schwarz, Eric M.,Vaden, Michael T. IBM POWER6 microarchitecture. IBM Journal of Research and Development . 2007

SECTION II

Formulation and application of rate-independent stress update algorithm of hydrostatic pressure: elastoplastic yielding in composite

Abstract

The stress update algorithm is widely adopted in the analysis of the plastic mechanism of materials. The Drucker-Prager criterion is a yield function dependent on both hydrostatic pressure and deviatoric stress. Applied with the Drucker-Prager criterion, here, we develop a stress update algorithm depicting such a process by adopting the post-yield behavior given by An. The fiber-reinforced composite is widely applied in manufacturing nowadays. The plastic effect of the matrix to the composite under tensile loading is investigated in the article, for which the Drucker-Prager criterion is adopted to delineate the mechanical behavior of the matrix. A matrix deflection mechanical effect is also taken into consideration by studying the stress-strain distribution variances. The results show that the stress is centrally concentrated while growing evenly distributed and concentrated on the fiber's 1-directional edge with the ongoing load. The strain also exhibits similar distribution at the beginning albeit concentrated at the fiber's tangential surface with the loading. With the deflection of the matrix, the 2-directional stress exhibits higher values in the local deflection region, indicating a higher possibility of the local failure in the composite. Also, the local deflection does not influence the plastic strain distribution.

Keywords: plasticity; stress update algorithm; Drucker-Prager criterion; composite materials; fiber-reinforced composite

Introduction

Plasticity is a general nature of materials. To depict such nature, one applies a model described by a constitutive equation which can be delineated by the stress algorithm [1]. The stress update algorithm could be applied to different materials, with regards to the evolution of the internal variables and the determination of the yield function ([2], [3], [4]). The rate-independent isotropic hardening plasticity is described by details such that a parametric form function k is applied to depict the update algorithm, which can be distinguished as swift, voce and swift-voce [5]. Based on such, an example of a uniaxial tensile loading acting on a cubic is presented to illustrate the application of stress-update algorithm [6] and a finite difference method in which a homogenous anisotropic hardening model used is given as illustrating the yielding process [7]. An elastoplastic model calculated by stress update is applied to the mechanical calculation of clay [8].

The stress update algorithm could be used for the estimation of materials mechanical properties. An *et al.* presented works using the plasticity theory to depict the mechanical properties of biomaterials ([9], [10], [11], [12], [13]). Among many yield functions, with consideration of the hydrostatic pressure, the Drucker-Prager criterion could be representative. Plus, such yield function could also be applied for the explanation of the mechanisms of dentin fracture properties ([12], [13]). The mathematical basis for such a model is elucidated [14]. Furthermore, the depiction of the stress update algorithm could be applied by MATLAB code ([15], [16]).

The composite is widely adopted for manufacturing due to its spectacular mechanical properties. Also, the composite materials exhibit special elastic-plastic response with microscopic structures [17]. To delineate such, the strength of the steel-concrete composite is calculated showing plastic stress distribution method can yield significantly unconservative strength predictions, especially for encased composite members with high steel yield strengths and high steel ratios [18]. The mechanism of the particulate composite is elucidated through numerical finite element method, in which different modelling is adopted [19]. Similarly, the hierarchical structured composite's mechanical behavior is tested through different loading simulations, indicating temperature has the significant effects on the performances of 3D braided composites [20]. The rate-dependent plastic yielding of fiber-reinforced composite has also been studied by many scholars with regards to the mesoscale modelling [21], which is concentrated and studied in this paper.

Method

Analytical Solution

The strain is split into an elastic and a plastic part

$$\boldsymbol{\varepsilon} = \boldsymbol{\varepsilon}^e + \boldsymbol{\varepsilon}^p \quad (1)$$

i.e. the elastic strain is

$$\boldsymbol{\varepsilon}^e = \boldsymbol{\varepsilon} - \boldsymbol{\varepsilon}^p \quad (2)$$

Therefore, the constitutive equation for stress

$$\boldsymbol{\sigma} = \mathbf{C} : (\boldsymbol{\varepsilon} - \boldsymbol{\varepsilon}^p) \quad (3)$$

Where \mathbf{C} is the fourth-order isotropic stiffness tensor taking the form

$$\mathbf{C} = 2G\mathbf{1}\mathbf{1} + \left(K - \frac{2}{3}G\right)\mathbf{1}\otimes\mathbf{1} \quad (4)$$

The yield function is given by Drucker-Prager criterion:

$$f(\boldsymbol{\sigma}, c) = \sqrt{\frac{3}{2}s_{ij}s_{ij}} + \frac{1}{3}\sigma_{kk}\tan\beta - c \quad (5)$$

In which c denotes the cohesion force under uniaxial compression:

$$c = (1 + \tan\beta)\sigma_y \quad (6)$$

Where σ_y is the uniaxial tensile yield stress. Based on the previous study of the constitutive model of cordial bone conducted by An [10], a power law strain hardening is employed to characterize the post-yield behavior

$$\sigma_y = \sigma_0 \left(1 + \frac{\varepsilon^p}{\varepsilon^0}\right)^n$$

In the study, to simplify the reasoning, the strain hardening exponent: $n = 7$ (7)

Where J_1 and J_2 yield surface at

$$f(\boldsymbol{\sigma}, c) = \sqrt{\frac{3}{2}\|\mathbf{s}\|} + \tan\beta\|\mathbf{p}\| - c = 0 \quad (8)$$

Consider the case where the yield function defines plastic potential, the flow rule of rate-independent plasticity is given by:

$$\dot{\boldsymbol{\varepsilon}}^p = \lambda h_{ij} = \lambda \frac{\partial f}{\partial \boldsymbol{\sigma}} = \lambda \hat{\boldsymbol{n}} \quad (9)$$

Where $\dot{\boldsymbol{\varepsilon}}^p$ is plastic strain, λ is an indeterminate is an indeterminate positive quantity when $f = 0$ and $\left(\frac{\partial f}{\partial \boldsymbol{\sigma}}\right) \dot{\boldsymbol{\sigma}} = 0$, and is zero otherwise.

In either case, $\dot{\lambda}$ and f can easily be seen to obey the Kuhn–Tucker conditions of optimization theory. Thus, the loading/unloading condition is:

$$\dot{\lambda}f = 0, \quad \dot{\lambda} \geq 0, \quad f \leq 0 \quad (10)$$

In which the flow vector $\hat{\boldsymbol{n}}$ is given by

$$\hat{\boldsymbol{n}} = \frac{\partial f}{\partial \sigma_{kl}} = \frac{\partial \sqrt{\frac{3}{2} s_{ij} s_{ij}}}{\partial \sigma_{kl}} + \frac{\partial \frac{1}{3} \sigma_m \tan \beta}{\partial \sigma_{kl}} - \frac{\partial c}{\partial \sigma_{kl}}$$

$$\hat{\boldsymbol{n}} = \frac{\partial \sqrt{3 J_2}}{\partial J_2} \frac{\partial J_2}{\partial \sigma_{kl}} + \frac{\tan \beta}{3} \frac{\partial \sigma_m}{\partial \sigma_{kl}} \quad (11)$$

$$\hat{\boldsymbol{n}} = \frac{\sqrt{3}}{2} J_2^{-\frac{1}{2}} s_{kl} + \frac{\tan \beta}{3} \delta_{kl} \quad (12)$$

...
(13)

$$\hat{\boldsymbol{n}} = \frac{\sqrt{6}}{4} \frac{\mathbf{s}}{\|\mathbf{s}\|} + \frac{\tan \beta}{3} \mathbf{1} \quad (14)$$

Where the flow vector could be divided into

$$\hat{\boldsymbol{n}}^s = \frac{\sqrt{6}}{4} \frac{\mathbf{s}}{\|\mathbf{s}\|}, \quad \hat{\boldsymbol{n}}^p = \frac{\tan \beta}{3} \mathbf{1} \quad (15)$$

Thence, the form of consistency can be written as

$$\dot{f}(\boldsymbol{\sigma}, c) = \hat{\boldsymbol{n}} : \left(\sqrt{\frac{3}{2}} \dot{\mathbf{s}} + p \tan \beta \right) - \dot{c} \quad (16)$$

In which

$$\dot{\mathbf{s}} = 2\mu\dot{\mathbf{e}}, \quad \dot{p} = K\dot{\varepsilon}_V, \quad \dot{\mathbf{c}} = (1 + \tan\beta)\sigma_0 \left(1 + \frac{\dot{\boldsymbol{\varepsilon}}^p}{\varepsilon^0} \right)$$

Thenceforth, the consistency condition takes the form

$$\dot{f} = \frac{\partial f}{\partial \boldsymbol{\sigma}} : \dot{\boldsymbol{\sigma}} - (1 + \tan\beta)\sigma_0 \left(1 + \frac{\dot{\boldsymbol{\varepsilon}}^p}{\varepsilon^0} \right) \quad (18)$$

Which can be reduced into:

$$\dot{f} = \frac{\partial f}{\partial \boldsymbol{\sigma}} : \dot{\boldsymbol{\sigma}} - (1 + \tan\beta)\sigma_0 \left(1 + \frac{\lambda \hat{\mathbf{n}}}{\varepsilon^0} \right) \quad (19)$$

Given that

$$\hat{\mathbf{n}} : \dot{\boldsymbol{\sigma}} = \hat{\mathbf{n}} : \dot{\mathbf{s}} + \hat{\mathbf{n}} : \dot{p} \quad (20)$$

The equation can be decomposed into

$$\dot{f} = \frac{\partial f}{\partial \mathbf{s}} : \dot{\mathbf{s}} + \frac{\partial f}{\partial p} : \dot{p} \mathbf{1} - (1 + \tan\beta)\sigma_0 \left(1 + \frac{\lambda \hat{\mathbf{n}}}{\varepsilon^0} \right) \quad (21)$$

In which

$$\frac{\partial f}{\partial \boldsymbol{\sigma}} : \dot{\boldsymbol{\sigma}} = \frac{\partial f}{\partial \mathbf{s}} : \dot{\mathbf{s}} + \frac{\partial f}{\partial p} : \dot{p} \mathbf{1} = 2\mu(\hat{\mathbf{n}} : \dot{\mathbf{e}} - \lambda) + E(\hat{\mathbf{n}} : \dot{\varepsilon}_V - \lambda) \quad (22)$$

Hence, substituting Equation 21 into Equation 20 one deduce

$$\lambda = \frac{\hat{\mathbf{n}} : (2\mu\dot{\mathbf{e}} + K\dot{\varepsilon}_V) - \sigma_0(1 + \tan\beta)}{\sigma_0(1 + \tan\beta) \left(1 + \frac{\hat{\mathbf{n}}}{\varepsilon^0} \right) + 2\mu + E} \quad (23)$$

Numerical solution

The first step in the numerical integration is to write the stress tensor in the predictor-corrector format,

$$\boldsymbol{\sigma}_{n+1} = \boldsymbol{\sigma}_{n+1}^{tr} - \mathcal{C}^e : \Delta \boldsymbol{\varepsilon}, \quad \boldsymbol{\sigma}_{n+1}^{tr} = \boldsymbol{\sigma}_{n+1} + \mathcal{C}^e : \Delta \boldsymbol{\varepsilon} \quad (24)$$

Using the backward implicit scheme for integrating the incremental plastic flow, one could discern:

$$\Delta \boldsymbol{\varepsilon}^p = \int_{t_n}^{t_{n+1}} \dot{\lambda} \hat{\mathbf{n}} dt \approx \Delta \lambda \hat{\mathbf{n}}_{n+1}$$

$$\hat{\mathbf{n}}_{n+1} = \frac{\sqrt{6}}{4} \frac{\mathbf{s}_{n+1}}{\|\mathbf{s}_{n+1}\|} + \frac{\tan\beta}{3} \mathbf{1}_{n+1}$$

$$\Delta \lambda = \frac{a - c_n}{\sigma_0(1 + \tan\beta) \left(1 + \frac{\hat{\mathbf{n}}_{n+1}}{\varepsilon^0}\right) + 2\mu + E} \quad (26)$$

Where $\Delta \lambda$ is the discrete plastic multiplier.

The cohesion is updated as

$$c_{n+1} = c_n + (1 + \tan\beta) \sigma_0 \left(1 + \frac{\varepsilon^p}{\varepsilon^0}\right) \quad (28)$$

For rate-independent plastic materials, the discrete consistency equation can be written as:

$$f_{n+1} = \sqrt{\frac{3}{2}} \|\mathbf{s}_{n+1}\| + p_{n+1} \tan\beta - c = 0 \quad (29)$$

We take the trace of both sides of the discrete constitutive equation

$$tr(\boldsymbol{\sigma}_{n+1}) = tr(\boldsymbol{\sigma}_{n+1}^{tr}) \Rightarrow p_{n+1} = p_{n+1}^{tr} \quad (30)$$

Where $p = tr \frac{\boldsymbol{\sigma}}{3}$ is the mean normal stress.

For isotropic linearly elastic material, the elastic constitutive equations are

$$\mathbf{s} = 2\mu \mathbf{e}, \quad p = K \varepsilon_V \quad (31)$$

Where K and μ are the elastic bulk and shear moduli, respectively.

Now, split the strain into two parts and consider each:

$$\mathbf{e} = \frac{\sqrt{6}}{4} \frac{\mathbf{s}_{n+1}}{\|\mathbf{s}_{n+1}\|}, \quad \varepsilon_V = \frac{\tan\beta}{3} \mathbf{1}_{n+1} \quad (32)$$

Therefore, the form of the deviatoric and mean stress is given by

$$\mathbf{s}_{n+1} = \mathbf{s}_{n+1}^{tr} - 2\mu \Delta \lambda \left(\frac{\sqrt{6}}{4} \frac{\mathbf{s}_{n+1}}{\|\mathbf{s}_{n+1}\|} \right), \quad p_{n+1} = p_{n+1}^{tr} - K \Delta \lambda \left(\frac{\tan\beta}{3} \mathbf{1}_{n+1} \right) \quad (33)$$

Therefore,

$$\hat{\mathbf{n}}_{n+1} = \hat{\mathbf{n}}^s_{n+1} + \hat{\mathbf{n}}^p_{n+1}$$

In which

$$\hat{\mathbf{n}}^s_{n+1} = \sqrt{\frac{3}{2}} \frac{\mathbf{s}_{n+1}^{tr}}{a}, \quad \hat{\mathbf{n}}^p_{n+1} = \frac{\tan\beta \mathbf{1}_{n+1}}{3a} \quad (35)$$

Step 1. Compute $\sigma_{n+1}^{tr} = \sigma_n + c^e : \Delta \boldsymbol{\varepsilon}$,

$$p_{n+1} = \frac{1}{3} \text{tr}(\sigma_{n+1}^{tr}), \quad \mathbf{s}_{n+1}^{tr} = \sigma_{n+1}^{tr} - p_{n+1} \mathbf{1}$$

Step 2. Check $a = \left\| \sqrt{\frac{3}{2}} \mathbf{s}_{n+1}^{tr} + \tan\beta p_{n+1} \mathbf{1} \right\| > c$?

No, set $\sigma_{n+1} = \sigma_{n+1}^{tr}$ and exit.

Step 3. Yes, set $\hat{\mathbf{n}}^s_{n+1} = \sqrt{\frac{3}{2}} \frac{\mathbf{s}_{n+1}^{tr}}{a}$, $\hat{\mathbf{n}}^p_{n+1} = \frac{\tan\beta \mathbf{1}_{n+1}}{3a}$, $\hat{\mathbf{n}}_{n+1} = \hat{\mathbf{n}}^p_{n+1} + \hat{\mathbf{n}}^s_{n+1}$

$$\Delta\lambda = \frac{a - c_n}{\sigma_0(1 + \tan\beta) \left(1 + \frac{\hat{\mathbf{n}}_{n+1}}{\varepsilon^0} \right) + 2\mu + E}$$

$$\sigma_{n+1} = \sigma_{n+1}^{tr} - 2\mu\Delta\lambda \hat{\mathbf{n}}_{n+1} - E\Delta\lambda \hat{\mathbf{n}}_{n+1}$$

$$c_{n+1} = c_n + (1 + \tan\beta)\sigma_0 \left(1 + \frac{\varepsilon^p}{\varepsilon^0} \right) \text{ and exit}$$

Box. 1 Radial return algorithm for stress update with Drucker-Prager criterion.

Problem Formulation

As mentioned in the preceding chapter the composite is now more applied in manufacturing and engineering design more than ever ([18], [19], [20], [21]). For what is more, the plastic deformation and its compact is of great importance in the study of composite [21]. Hence, an application of the Drucker-Prager criterion is carried out to study the plastic deformation's impact of the matrix in fiber reinforced composite.

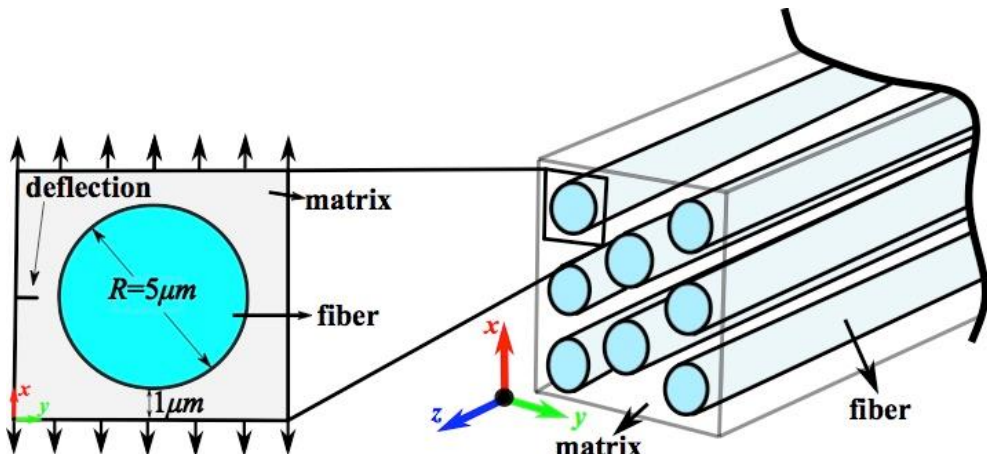


Fig. 1 Schematic illustration of the fiber reinforced composite, in which the zoomed view in the left is a “unit cell model” representative for the structure.

To study such effect, we carried out simulations applied with the Drucker-Prager criterion on the fiber-reinforced composite. The fiber-reinforced composite consists of fiber and matrix (usually consists of resin), which can be modelled as a unit cell model as shown in Figure 1. The study mainly focuses on the tensile plastic effect on the fiber-reinforced composite. For what is more, during the designing and manufacturing process, hardly prevented that deflection occurs on the composite, which usually exhibits as small fracture or cracks on the matrix as shown in Figure 1. Such effect is also taken into consideration in the modelling that compared and discussed in the following chapter. Simultaneously, the deflection is not propagated as the ongoing loading. Here, we only consider its impact on stress-strain distribution.

Material	Elastic Modulus	Poisson’s Ratio
Fiber	1GPa	0.3
Matrix	1MPa	0.3

Tab. 1 The elastic mechanical parameters for both the fiber and matrix.

The elastic mechanical parameters carried out for simulation is shown as in Table 1, in which the fiber is taken as a perfectly elastic material with high stiffness. The matrix is considered as a plastic material applied with the Drucker-Prager yield function, where the coefficients for the yield criterion is shown as in Table 2.

Yield Stress	Angle of Friction	Angle of Dilation	Flow Stress Ratio
100MPa	36	36	0.9

Tab. 2 Parameters for matrix applied for the Drucker-Prager criterion in the simulation.

Results and Discussion

Undergoing the 2-directional tensile loading, the stress σ_{22} distribution is shown as in Figure 2, in which the developing of stress distribution with loading time is presented from (a) to (f). From Figure 2 one could discern that the stress is highly concentrated in the central axis from the beginning phase. As the loading keeps, the stress is distributed evenly on both the matrix and fiber, comparatively. Howbeit the stress is highly concentrated on the 1-directional edge of the fiber and relatively low of the edge contacted matrix, which is not exhibited as the beginning stage. Also, the deformation changes from a smooth to an edged outline with the ongoing load.

The 2-directional strain distribution is also presented as in Figure 3. From the strain development, one could discern the strain concentrated on the shear surface along the fiber edge developing with time from (d) to (f).

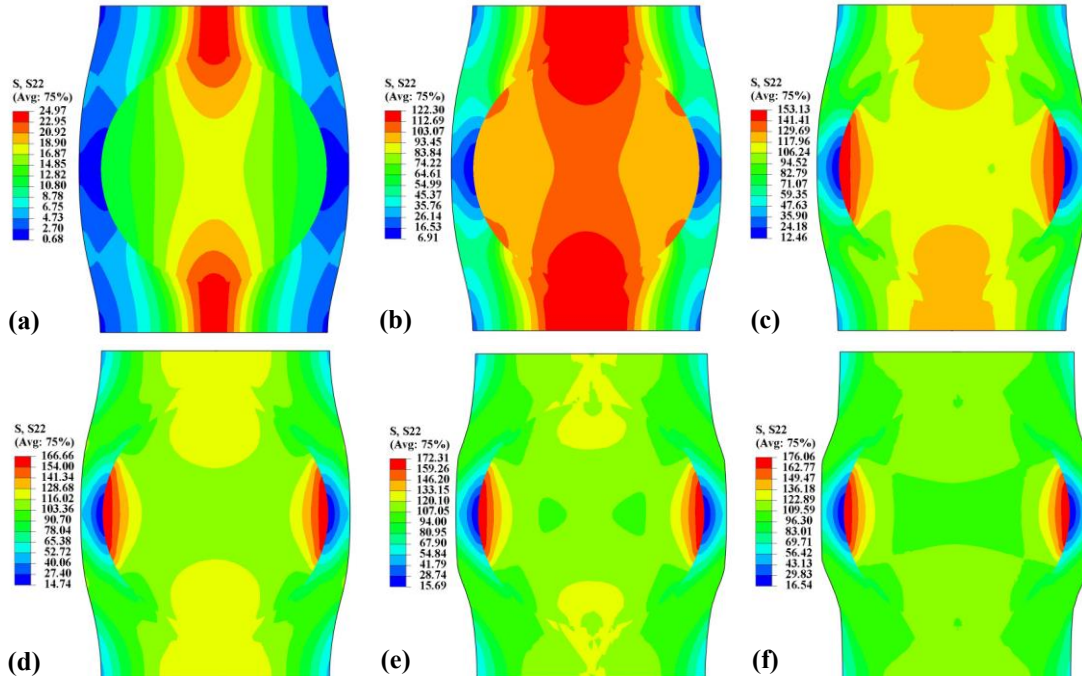


Fig. 2 The 2-directional stress distribution on the composite developing in time from (a) to (f).

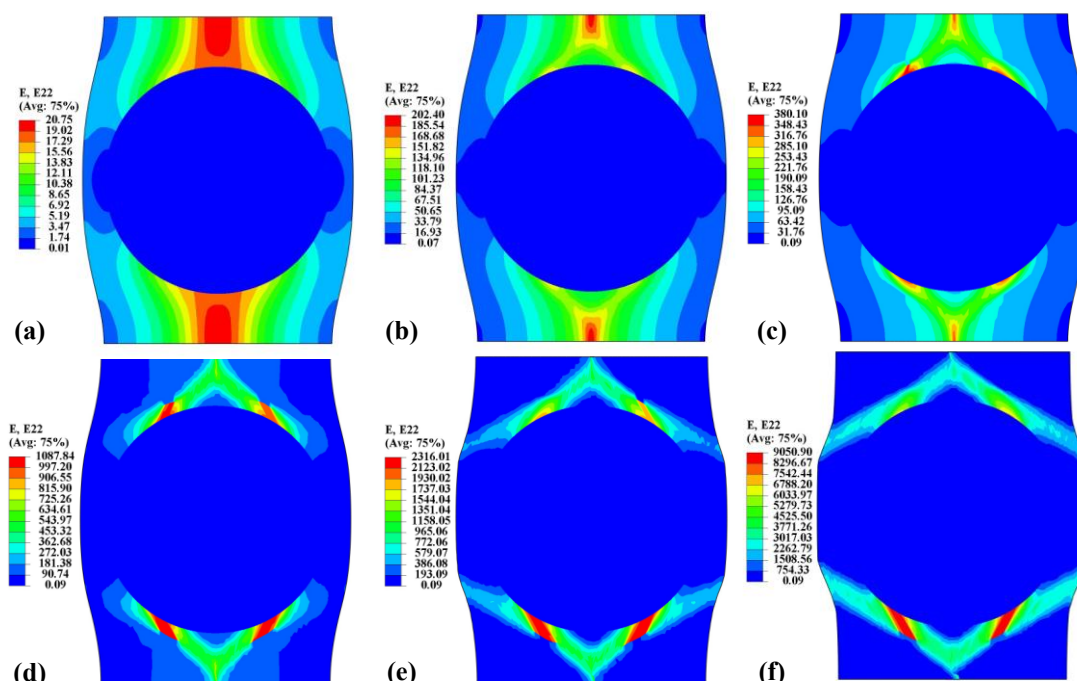


Fig. 3 The 2-directional strain distribution on the composites developing in time from (a) to (f).

Plus, at the beginning stage, the strain also exhibits similar distribution as the stress, where ε_{22} is highly concentrated along the central axis. With the ongoing load, the plastic strain concentrating tangential with the fiber circular edge as shown in Figure 3(f).

Here, as mentioned in the last chapter, we elicit a deflection on the matrix of composite to investigate its effect. The 2-directional stress distribution development is shown as in Figure 4 from (b) to (f), which exhibits similar trends as in Figure 2. The zoomed view of the deflection development is shown in Figure 4(a).

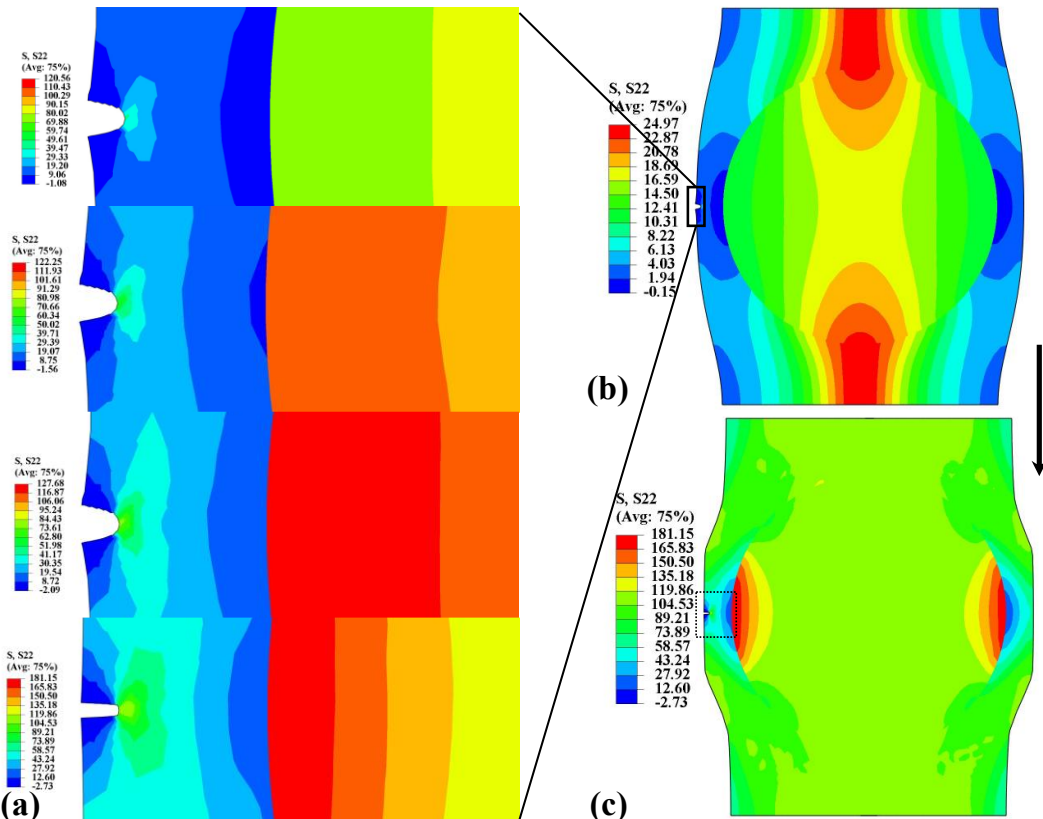


Fig. 4 The 2-directional stress distribution on the composites with deflection developing in time from (b) to (c), in which (a) shows a zoomed view for the propagation of the deflection.

From Figure 4(a), we can observe a local stress concentration at the end of the deflection. Such indicates that the high concentration of stress might elicit the local failure of the matrix. For what is more, the evident local stress increasement can be observed compare Figure 4(c) with Figure 2(f). Generally, the stress σ_{22} did not significantly changed compared with the no deflection model presented in Figure 2. Notwithstanding, the local deflection increases the local, and thence, the total 2-directional stress.

Also, the total strain ε_{22} distribution with the matrix deflection is presented as in Figure 5, developing from (a) to (c). From such distribution one can observe that the local matrix deflection only slightly change the local strain at the beginning stage, albeit basically makes no variance on the strain in the following stages.

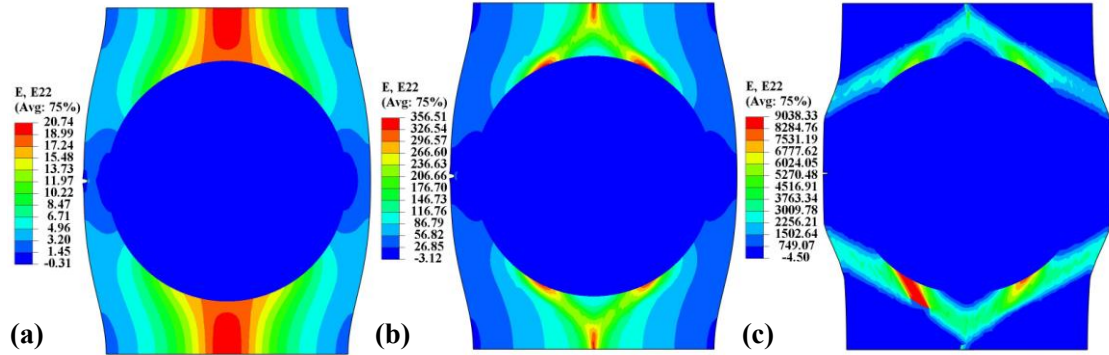


Fig. 5 The 2-directional strain distribution on the composites with deflection developing in time from (a) to (c).

The plastic strain distribution is shown in Figure 6 with the ongoing loading from (a) to (c), in which the deflection is taken into consideration.

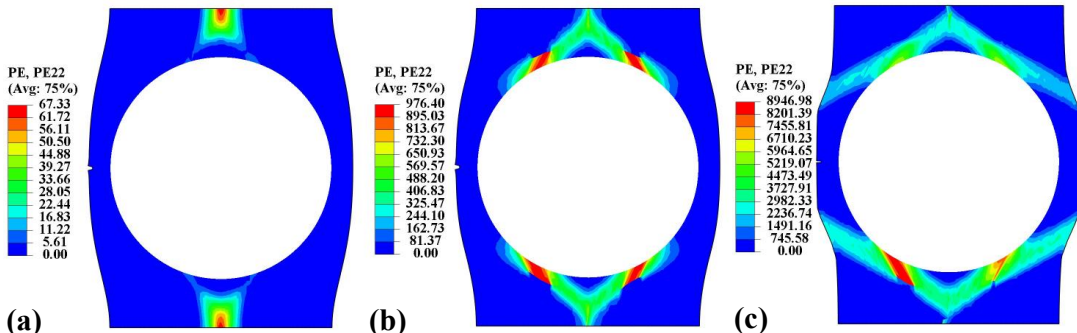


Fig. 6 The 2-directional plastic strain distribution on the composites with deflection developing in time from (a) to (c).

From Figure 6, one can discern that the matrix deflection makes no impact on the 2-directional plastic strain. Furthermore, the strain concentration along the central axis shown both in Figure 3(a) and Figure 5(a) is not plastic strain compared with Figure 6(a). the plastic strain grows from the loading edge to the tangential surface of fiber shown from Figure 6(a) to Figure 6(c).

Here, we also present a 2-directional stress-strain diagram of the matrix documenting the maximum value as shown in Figure 7.

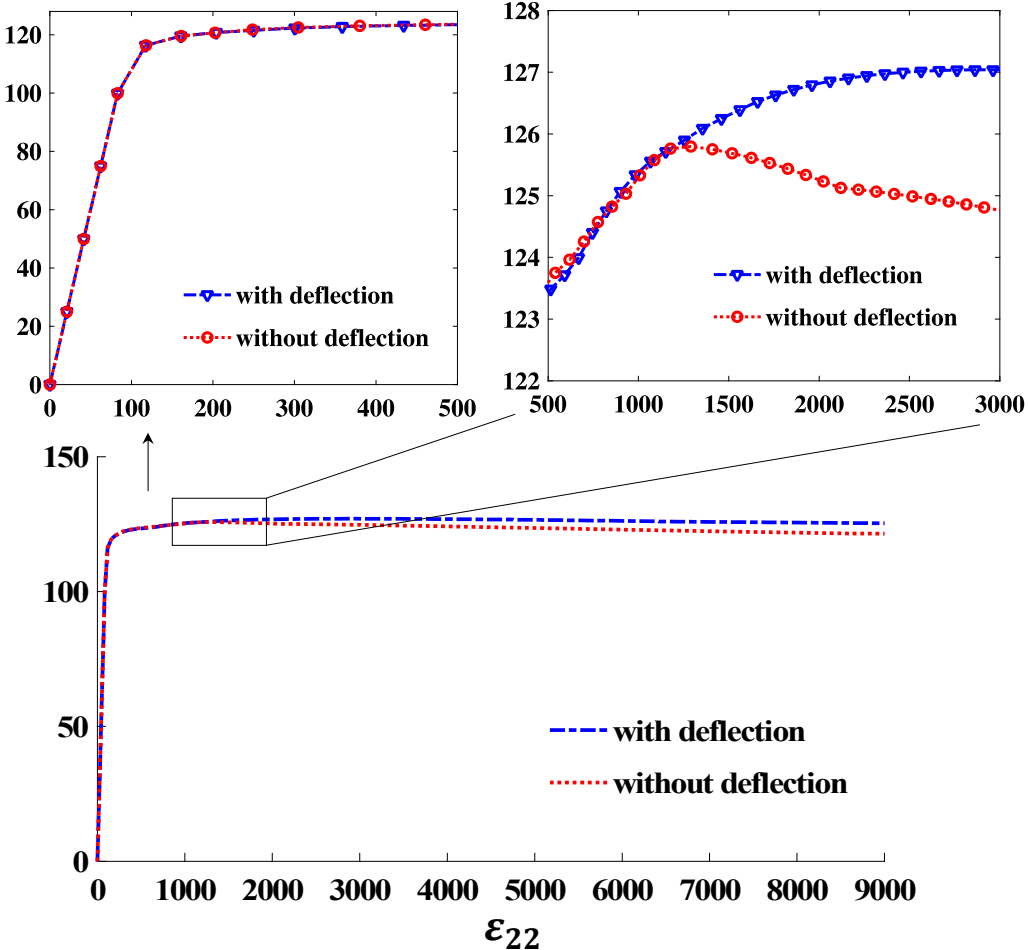


Fig. 7 The stress-strain curve of the composite with and without deflection, in which the unit is set to be [MPa].

From Figure 7, one can discern that the stress-strain curve coincides with each other at the beginning stage, including the elastic region and initial yielding state as shown in the left zoomed view. Notwithstanding, the yield region contends that the model with a matrix deflection exhibits higher values of stress as shown in the right zoomed view, which can be illustrated and explained by Figure 4. Also, such impact indicates a higher possibility of the local fracture as discussed in the preceding paragraphs. For what is more, the right zoomed view also indicates how the stress fluctuated as the initial stress variation stage.

For both the simulation illustrations and the diagrams indicate the variation effect of the matrix deflection will increase the 2-directional stress, especially the area surrounding the deflection. Also, the plastic strain growth distribution indicates a possible failure mechanism of the fiber-reinforced composite, to fracture along the fiber's shearing surface.

Conclusion

The rate-independent stress update algorithm with the Drucker-Prager criterion is reasoned both from an analytical solution (Equation 1-Equation 23) and a numerical solution (Equation 24-Equation 35) and illustrated as in Box 1. The fiber-reinforced composite is estimated as a unit cell model through decent simulations carried out with a tensile loading as illustrated in Figure 1. The unit cell is discussed in which a comparison of the addition of the deflection. The material coefficients carried out for simulation are given in Table 1 and Table 2.

The simulation results show that with the no deflection model, the stress is centrally concentrated along the middle axis at the beginning stage (Figure 2(a)), and growing more evenly distributed on the composite yet robustly concentrated on the 2-directional fiber edge (Figure 2(f)). A relatively low-stress value also occurs on the contact surface of the matrix (Figure 2(f)).

Also, the strain distribution shows that the strain displays similar trends with stress at the beginning stage, in which its value is highly concentrated along the central axis (Figure 3(a)), howbeit growing to highly concentrated along the shear surface of the fiber (Figure 3(f)).

When considering the existence of the local deflection on the matrix, the stress distribution generally follows the same as in without deflection (Figure 4(b), Figure 4(c)). Howbeit a local stress concentration occurs due to the deflection (Figure 4(a)). Specifically, the deflection elicits the stress concentration and the tail of the deflection. Also, the deflection model displays a similar strain distribution with the non-deflection model (Figure 3, Figure 5), only a small strain decrease at the deflection edge (Figure 5(a)). When discussing the plastic strain of the matrix, the deflection makes no difference in its distribution (Figure 6).

Of the stress-strain curve of the matrix (Figure 7), the deflection model displays higher stress value, which is explained and elucidated in the stress distribution (Figure 4). The curves coincide in the elastic region and the initial yielding stage (left zoomed view in Figure 7). Howbeit the stress fluctuates in a complex form at the beginning of yielding (right zoomed view in Figure 7).

References

- [1] Jacob Lubliner [1990]. PLASTICITY THEORY.
- [2] Alberto M Cuitiño. A material independent method for extending stress update algorithms to finite plasticity with multiplicative kinematics. *Engineering Computations*. December 1992
- [3] Ronaldo I. Borja. Plasticity, Modeling & Computation. DOI 10.1007/978-3-642-38547-6. 2013938490
- [4] J.C. Simo and T.J.R. Hughes. Computational Inelasticity. 1998, Volume 7. ISBN : 978-0-387-97520-7
- [5] D. Mohr. Integration Algorithms for Rate-independent Plasticity (1D). Lecture #4 – Fall 2015. ETH Zürich.
- [6] Dynamic Behavior of Materials and Structures. Computer Lab #5, Page 4: Stress update algorithm on von Mises plasticity.
- [7] H S Choi *et al* 2018 *J. Phys.: Conf. Ser.* **1063** 012011
- [8] M. Rezania, N. Sivasithamparam, M. M. Nezhad. On the stress update algorithm of an advanced critical state elasto-plastic model and the effect of yield function equation. *Finite Elements in Analysis and Design* 90 (2014) 74–83
- [9] B. An, H. D. Wagner. Role of microstructure on fracture of dentin. *Journal of the Mechanical Behavior of Biomedical Materials*. Vol 59 (2016): 527-537. ISSN 1751-6161.
- [10] An B. Constitutive modeling the plastic deformation of bone-like materials. *Int J of Solids Struct* 2016; Vol 92–93: 1-8
- [11] An B., Zhang D. Bioinspired toughening mechanism: lesson from dentin. *Bioinspir. Biomim.*, 10 (2015), Article 046010
- [12] B. An, D. Zhang. An analysis of crack growth in dentin at the microstructural scale. *Journal of the Mechanical Behavior of Biomedical Materials* 81 (2018) 149–160.
- [13] B. An, Y. Xu, D. Zhang. Crack initiation and propagation in composite microstructure of dentin. *International Journal of Solids and Structures* 110–111 (2017) 36–43
- [14] Xiong Zhang, Zhen Chen, Yan Liu. *The Material Point Method*, Academic Press, 2017, Pages 175-219, ISBN 9780124077164.

- [15] M. Čermák, S. Sysala, J. Valdmane (2018). Efficient and flexible MATLAB implementation of 2D and 3D elastoplastic problems. *Applied Mathematics and Computation.*
- [16] M. Čermák, S. Sysala, and J. Valdman. Matlab FEM package for elastoplasticity. 2018.
- [17] H. Teng. Effective elastic–plastic response of two-phase composite materials of aligned spheroids under uniaxial loading. *Mechanics of Materials* 117 (2018) 91–104.
- [18] A. Behnam, M. D. Denavit. Plastic stress distribution method for predicting interaction strength of steel-concrete composite cross sections. *Journal of Constructional Steel Research* 170 (2020) 106092.
- [19] M. Majewski, P. Holobut, M. Kursa, K. Kowalczyk-Gajewska. Packing and size effects in elastic-plastic particulate composites: Micromechanical modelling and numerical verification. *International Journal of Engineering Science* 151 (2020) 103271
- [20] C. He, J. Ge, B. Zhang, J. Gao, S. Zhong, W. K. Liu, D. Fang. A hierarchical multiscale model for the elastic-plastic damage behavior of 3D braided composites at high temperature. *Composites Science and Technology* 196 (2020) 108230
- [21] M. Zscheyge, R. Boehm, A. Hornig, J. Gerritzen, M. Gude. Rate dependent non-linear mechanical behaviour of continuous fibre-reinforced thermoplastic composites – experimental characterisation and viscoelastic-plastic damage modelling. *Materials & Design.*

SECTION III

Structural Designation of Composite Materials with Superior Mechanical Behaviors: Lesson from the Microstructure of Nacre and Enamel

Abstract

Biomaterials like nacre and tooth enamel display spectacular mechanical properties such as high stiffness, high strength, high toughness, and fracture durability. Such properties are exhibited by their natural developed structures, both employ common characteristics: consisting of hard mineral inclusions and soft protein matrix. Here, we build models, representative, for nacre, and enamel consisting of hard inclusions and soft matrix, respectively. We give the soft matrix a plastic property based on their natural mechanics. We thence calculate the 1 and 2-directional stiffness of the two structures and present their von Mises' stress, directional stress, and directional strain distribution, respectively. For what is more, we estimate the fracture resistance of the two structures based on the assumption that the failure occurs on the soft matrix in which the shear stress reaches a critical value. We hence deduce that the nacre displays better 1-directional stiffness and enamel displays better 2-directional stiffness. The shear stress-displacement diagrams in each direction are also presented indicating the nacre is more likely to fail in 1-direction and enamel is more likely in 2-direction. Based on the results we present an optimized model taking the characters from both the nacre and enamel. Results show that the optimized model exhibits higher stiffness in both the two directions and evidently better crack resistance in 2-direction.

Keywords: stiffness; fracture; biomaterials; biomechanics; bioinspired structure

Introduction

There are many species in nature. These creatures have evolved to obtain materials with superior mechanical properties with regard to their natural environment, which are called biomaterials. Biomaterials is among the key issue in structural design due to its spectacular performance. Human dentin is one of them. Dentin displays high crack resistance and hardening yielding behavior ([1], [3], [4]). Also, cortical bone displays similar crack resistance property ([2], [6], [7], [8]). The constitutive models for dentin and cortical bone are similar to many aspects, with hardening plastic property that exhibits superior fracture resistance ([1], [6]). Also, biomaterials composites all display similar hierarchical structure, which could be depicted by “architected”, in which hard inclusions bonded with soft matrix ([5], [7]). Mirkhalafa, *et al* [5] employ the CAD approach to estimate the hierarchical structure of enamel and nacre, which is the key essence studied in this paper.

As mentioned, the microstructure of nacre displays high durability, stiffness, and crack resistance, which could be illustrated as the “Brick-and-Mortar” structure. Such a structure is well studied by scholars. An experimental approach employing the three-point bending method tests the BM structure’s fracture resistance and present the crack propagation law illustrated by testing [9]. Experimental approaches illustrated the fracture mechanism of nacre and properties is explained by mesoscopic models [10]. For what is more, the tensile stiffness and strength, and fracture resistance are studied and tested by carrying out experiment directly studying the nacre’s mechanical properties [11]. A numerical approach to study its bending properties by studying the layer numbers effect on the nacre’s total bending load fracture resistance presents a complex relationship between the layer numbers and its mechanical properties [12]. Plus, spatial orientation and arrangement of such a structure are studied by the experimental approach [13].

Enamel is the hardest and most highly mineralized tissue of mammalian teeth, which displays high fracture resistance and complex hierarchical architecture structure [14]. Furthermore, the enamel section displays different architecture in certain areas, and the crack propagated along with the protein within rods [15]. Such a character is estimated and studied through an experimental approach revealing how the decussation structure resists crack growth with regards to directions and regions ([15], [16]). Not only humans, mammals such as wild wolf’s teeth also exhibit high toughness and durability with a hierarchical structure, consisting of hard rods and soft protein matrix [17]. The microscopic structure of the mentioned “rod” is hence estimated

through decent experiments and inspire a new structural design [18], whose thought trace is similarly employed in this paper.

Method

Problem Formulation

As mentioned in the preceding chapter, for both the nacre and the enamel's microstructure displays high stiffness and durability, which is highly focused in this paper. Their structural arrangement is the key issue studied. Hence, the modeling part is significantly important to ensure the main character is described properly with consideration of a universal application for the whole structure.

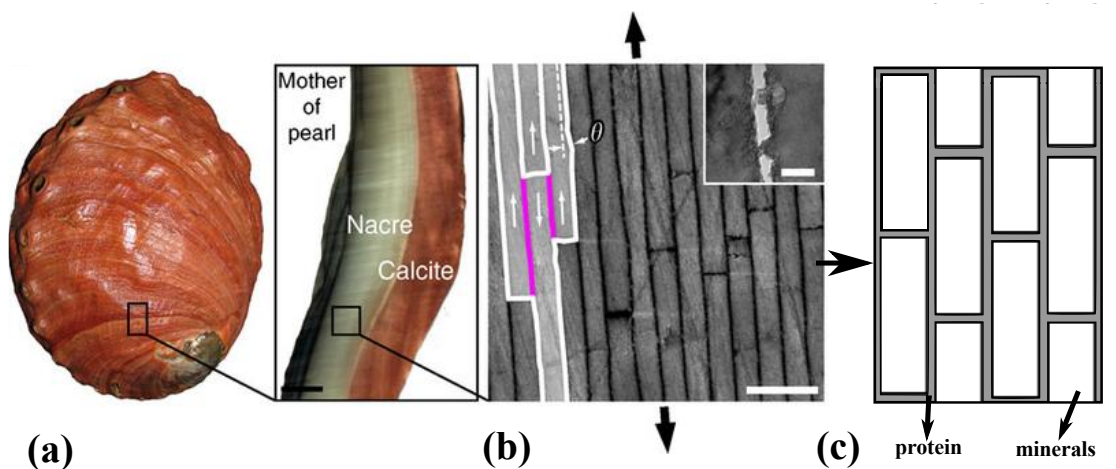


Fig. 1 The structural illustration of nacre. (a) photo of the nacre. (b) SEM photo of the nacre's microscopic structure. (c) schematic illustration of the nacre microscopic structure's modelling.

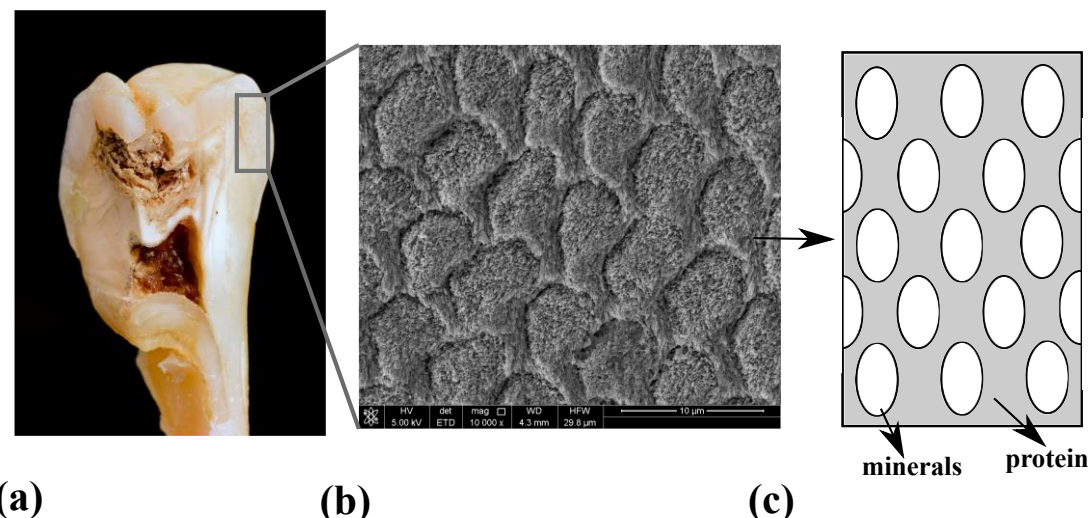


Fig. 2 The structural illustration of tooth enamel. (a) photo of the human tooth. (b) SEM photo of the enamel's microscopic structure. (c) schematic illustration of the enamel microscopic structure's modelling.

Initially, the modelling for the nacre structural design is shown in Figure 1(c), which is also described by the “Brick-and-Mortar” structure. With consideration of the chemical components, the hard inclusion usually consists of minerals, and the soft matrix consists of organic protein.

The modelling for the nacre structural design is shown as in Figure 2(c), in which the oval part is the enamel rod consisting of minerals surrounded by soft protein.

From both the scanning electron microscope (SEM) picture taken at a microscopic level of nacre and enamel shown in Figure 1(b) and Figure 2(b), we build the given model trying to illustrate the basic characters of the structure with a wide representation for the whole material. For what is more, the mechanical parameters for these materials are shown as in Table 1, in which the soft protein matrix employs a plastic property, as illustrated by An. *et al* ([1], [2], [3], [4]) and Ghazlana. *et al* [12]. We employ a perfect plastic model for the soft matrix. Admittedly, hard mineral inclusion displays plastic properties too [1], yet based on the previous analyzation of biomaterials’ fracture, crack does not usually propagate on hard minerals and mostly the minerals have not reached the yield stress when the composite fails ([5], [9], [12], [15], [16], [18]), hence the plastic property of hard inclusion is not considered in the study.

Material	Elastic Modulus	Poisson’s Ratio	Yield Stress
Mineral	20.7GPa	0.3	
Protein	1MPa	0.3	9MPa

Tab. 1 Mechanical parameters of the mineral and protein carried out for simulation.

Stiffness Calculation

To estimate the stiffness on each direction of the presented biomaterials, the elastic moduli for enamel and nacre are to be calculated with the set parameters. To delineate such, the mean strain is calculated taking the form

$$\begin{cases} \bar{\varepsilon}_x = \frac{u_x}{a} \\ \bar{\varepsilon}_y = \frac{u_y}{b} \end{cases} \quad (1)$$

In which u_x and u_y are displacements in 1 and 2 directions, respectively; a and b are length and width of the presented models, respectively.

The mean stress takes the form:

$$\begin{cases} \bar{\sigma}_x = \sum_{y=0}^b \frac{R_x(a, y)}{b} \\ \bar{\sigma}_y = \sum_{x=0}^a \frac{R_y(x, b)}{a} \end{cases} \quad (2)$$

In which R_x and R_y are reactional forces in 1 and 2 directions, respectively.

The 1 and 2-directional elastic moduli of the composite can thence be calculated through Equation 1 and 2:

$$\begin{cases} E_x = \frac{\bar{\sigma}_x}{\bar{\varepsilon}_x} \\ E_y = \frac{\bar{\sigma}_y}{\bar{\varepsilon}_y} \end{cases} \quad (3)$$

Fracture Estimation

As mentioned and presented through both numerical and experimental methods, the fracture and failure of the bioinspired structural materials occurs at the soft protein matrix and propagated along with such material in the whole structure ([5], [9], [12], [15], [16], [18]). For what is more, such local failure usually exhibits plastic properties that might resist the crack growth ([1], [2], [3], [4], [12]). Hence, here, we adopted two basic hypotheses for the composites' failure in simulation: 1). The failure occurs on matrix when shear stress reaches a specific critical value. 2). The matrix displays plastic properties in the fracture process. Usually, the displacement loaded can be directly measured. Therefore, we present the relation between the matrix shear stress with the composites' loading displacement to estimate and study the fracture properties.

Results and Discussion

Stiffness Calculation

Based on the model, the mechanical distribution can hence be calculated for the structures as given. The von Mises stress, 1-directional stress and 1-directional strain distribution of the enamel undergoing 1-directional loading are shown as in Figure 3.

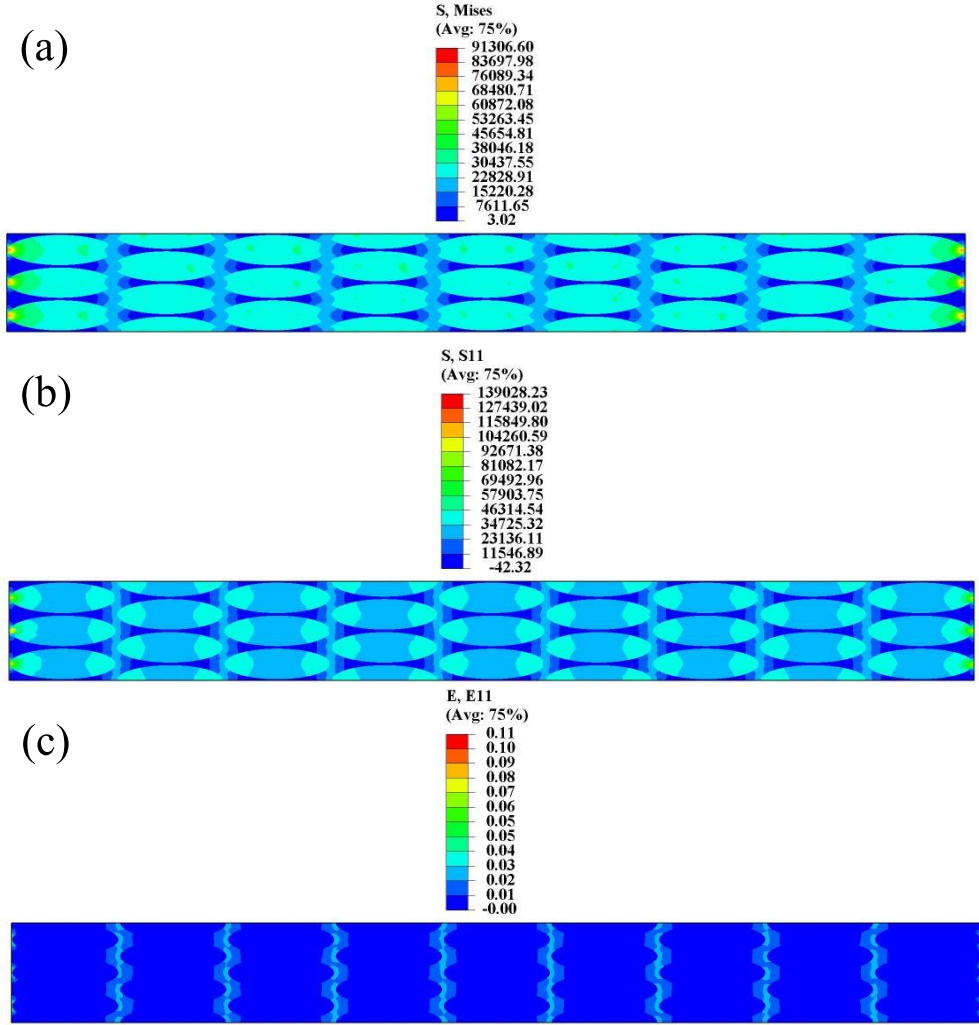


Fig. 3 The enamel's 1-directional mechanical distribution carried out for uniaxial tensile loading. (a) von Mises stress distribution. (b) 1-directional stress distribution. (c) 1-directional strain distribution.

From Figure 3(a) and Figure 3(b) one can discern the hard inclusion takes higher stress value due to its high stiffness, especially, the 1-directional stress is unevenly distributed on the hard inclusions as shown in Figure 3(b). As shown in Figure 3(c) one deduces that the contact surface undergoes higher strain values, which might also indicate local failure or deformation.

Similarly, the von Mises stress, 1-directional stress, and 1-directional strain distribution of the enamel undergoing 2-directional loading are shown as in Figure 4.

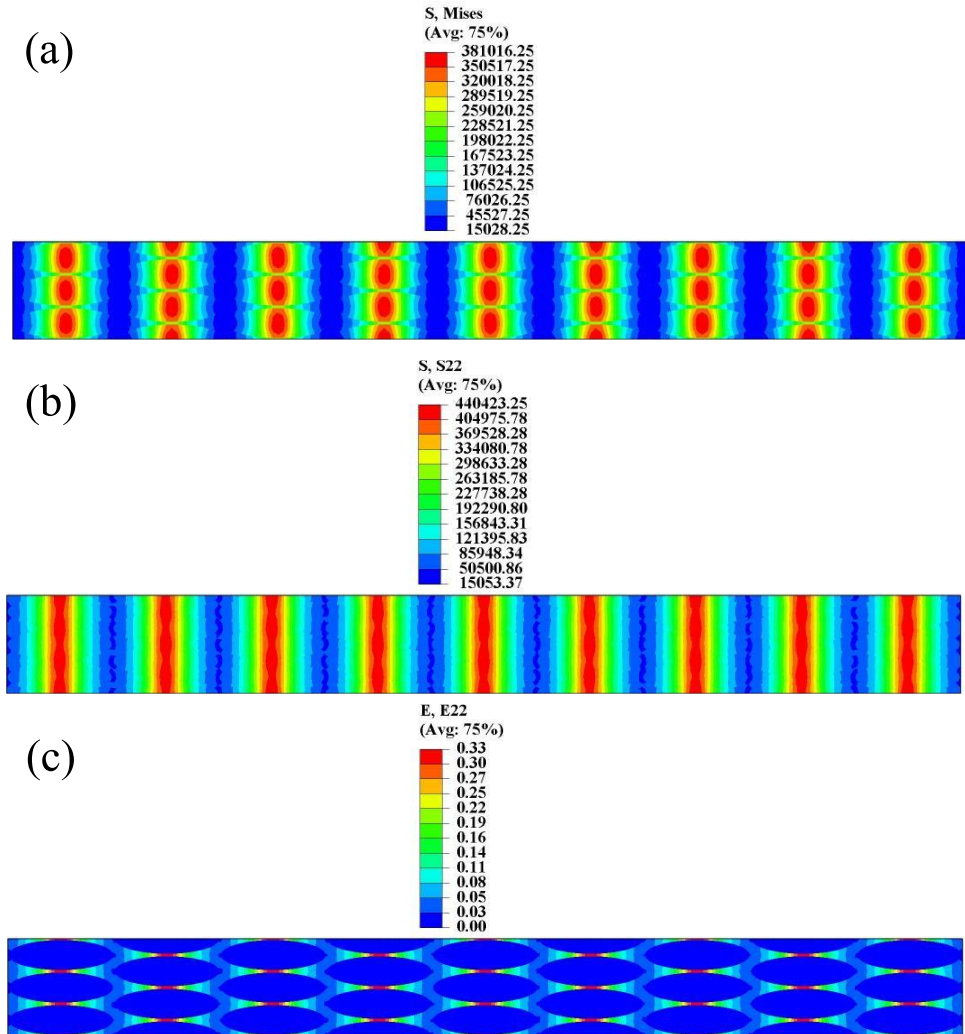


Fig. 4 The enamel's 2-directional mechanical distribution carried out for uniaxial tensile loading. (a) von Mises stress distribution. (b) 2-directional stress distribution. (c) 1-directional strain distribution.

Comparing Figure 4(a) with Figure 4(b) one could discern that the 1-directional stress also makes a robust effect on the Mises stress distribution due to the variance occurs on the rods' contact edge. From Figure 4(c) one could observe strain concentration on inclusion-matrix contact edge.

For the nacre structure, the von Mises stress, 1-directional stress and 1-directional strain distribution undergoing 1-directional loading are shown as in Figure 5.

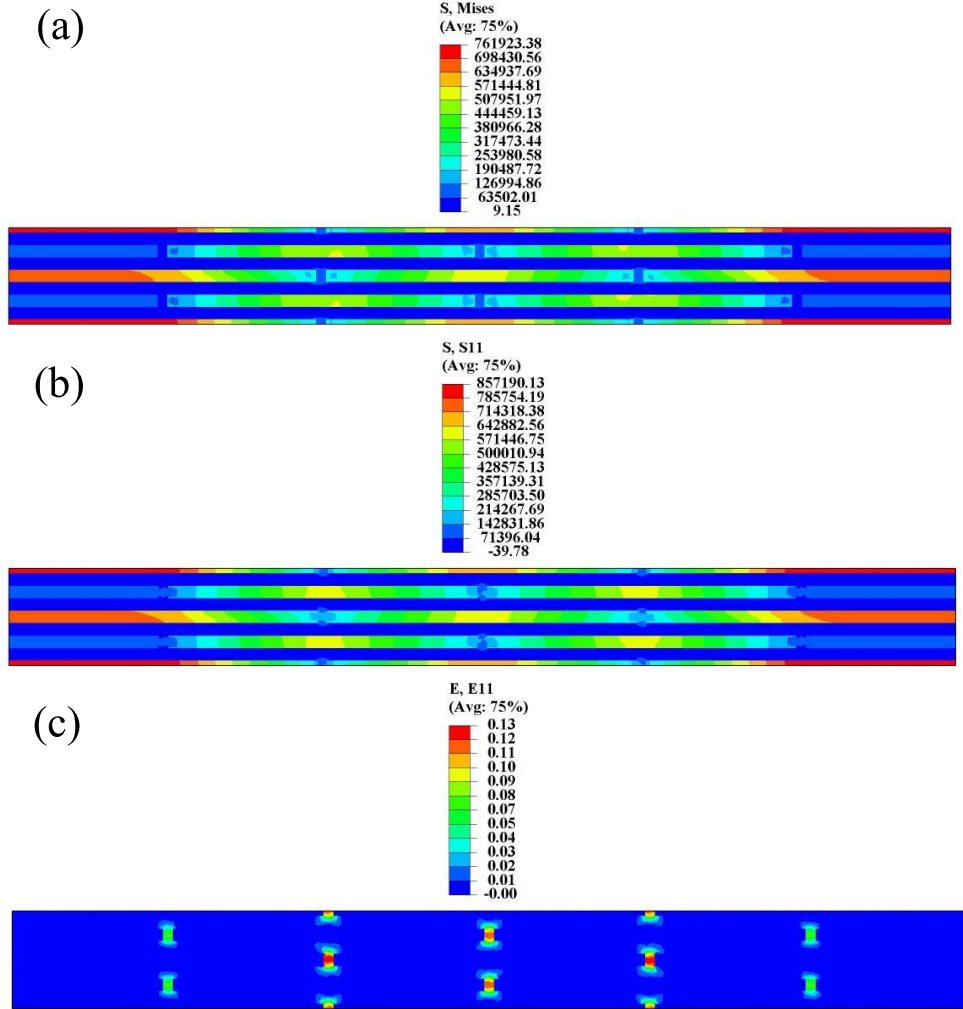


Fig. 5 The nacre's 1-directional mechanical distribution carried out for uniaxial tensile loading. (a) von Mises stress distribution. (b) 1-directional stress distribution. (c) 1-directional strain distribution.

From Figure 5 one could observe that the nacre's 2-directional stress makes little influence on the whole structure's stress distribution comparing Figure 5(a) and Figure 5(b). A strain concentration occurs at the soft matrix between contacts of nacre inclusion as shown in Figure 5(c). Such a concentration indicates a possible dislocation between inclusion layers.

The von Mises stress, 2-directional stress and 2-directional strain distribution of the nacre structure undergoing 2-directional loading are shown as in Figure 6.

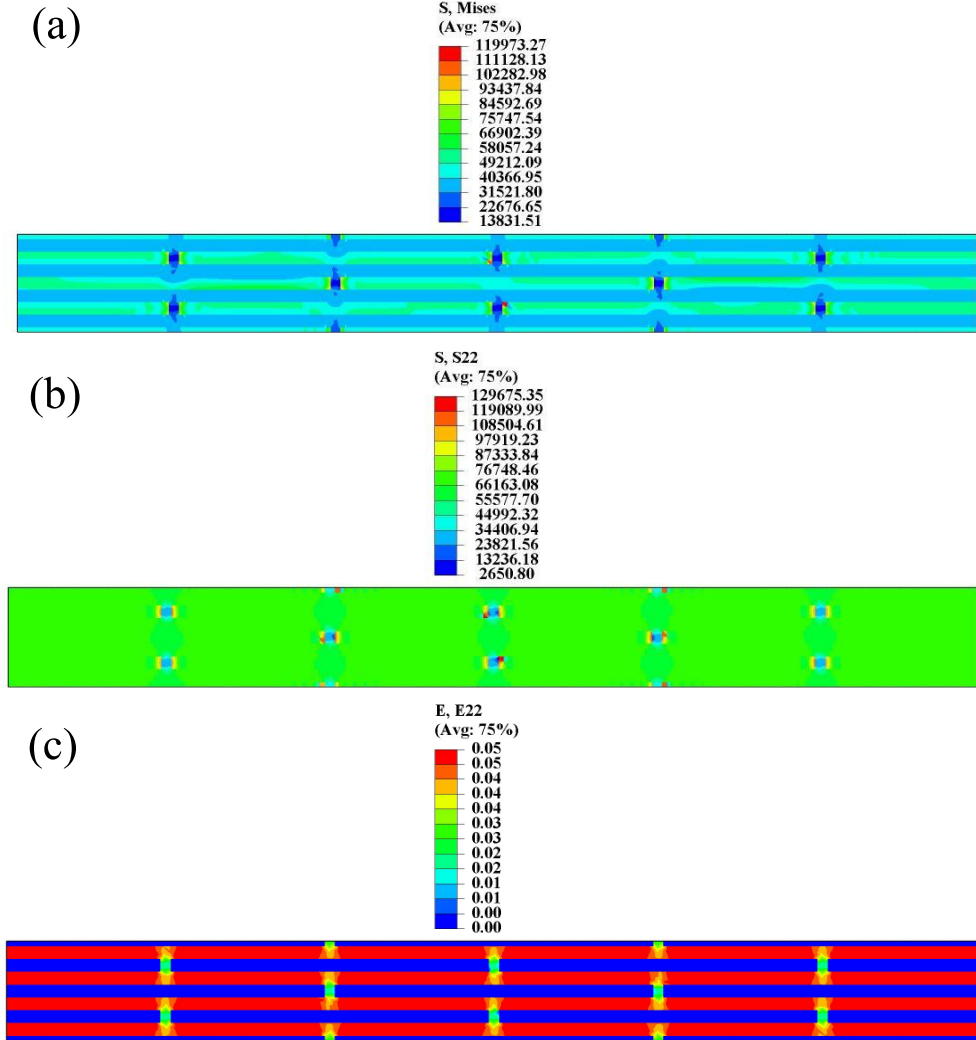


Fig. 6 The nacre's 2-directional mechanical distribution carried out for uniaxial tensile loading. (a) von Mises stress distribution. (b) 2-directional stress distribution. (c) 2-directional strain distribution.

Comparing Figure 6(a) with Figure 6(b) one observe that the nacre's 2-directional stress does not play the key role in the total stress distribution. Figure 6(c) shows that strain concentrates on hard inclusions undergoes 2-directional loading.

As illustrated in Figure 2-Figure 6, one could deduce a basic stiffness for each direction of each composite materials based on the stress-strain distribution. Applied with Equation 1-Equation 3 one could calculate the stiffness of each material as given in Figure 7.

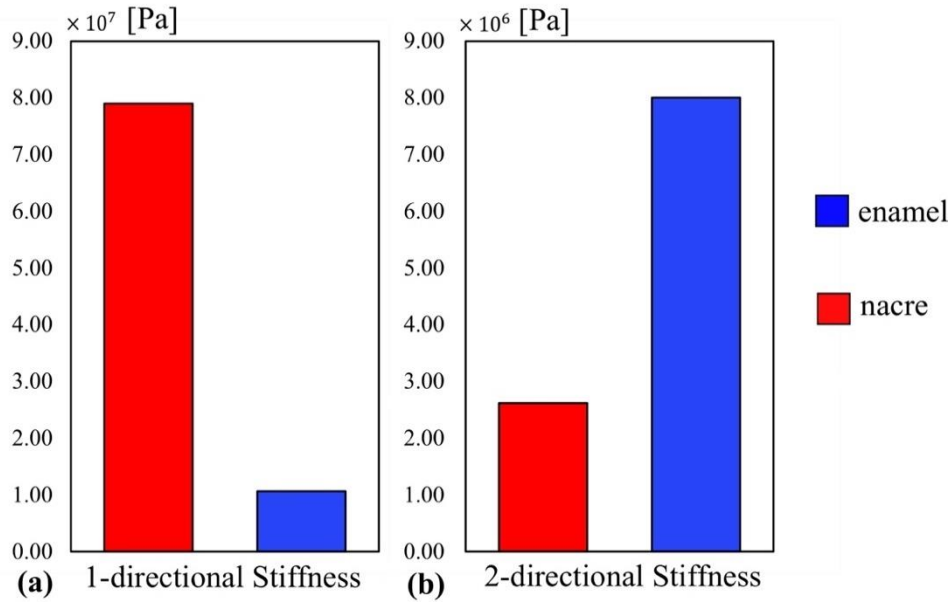


Fig. 7 The nacre and enamel structured composites' 1 and 2-directional stiffness.

As shown in Figure 7 the nacre's 1-directional stiffness is much higher than what is for enamel, yet the enamel's 2-directional stiffness is much higher than enamel. Firstly, the longitudinal lengthy hard inclusion in nacre could provide support for its longitudinal stiffness. Yet, for the higher value of the 2-directional stiffness of enamel, the circular shape and the evenly distributed contact area of the hard inclusion and the cross arranged rods could be a possible explanation.

Hence, we can adopt a basic thought trace that if a structural design contains characteristics of enamel and nacre in both the two directions might exhibit higher stiffness in both the two directions.

Fracture Estimation

As illustrated in the last chapter, the matrix (protein) fails when shear stress reaches a critical value. Thence, the shear stress distribution of enamel protein is given as shown in Figure 8(a) and the 1-directional displacement distribution when a 1-direction loading is applied is shown in Figure 8(b).

From Figure 8(a) one observes that there is a high concentration of shear stress occurs along with the 1-directional enamel rod's contact, which might indicate a possible protein fracture mechanism. For what is more, the high concentration of stress value is parallel with the 1-direction, implying an indicator of the mechanism to prevent the fracture take place along the axis perpendicular to the loading direction.

Figure 9 presents the shear stress distribution of enamel protein and the 2-directional displacement distribution when a 2-direction loading is applied.

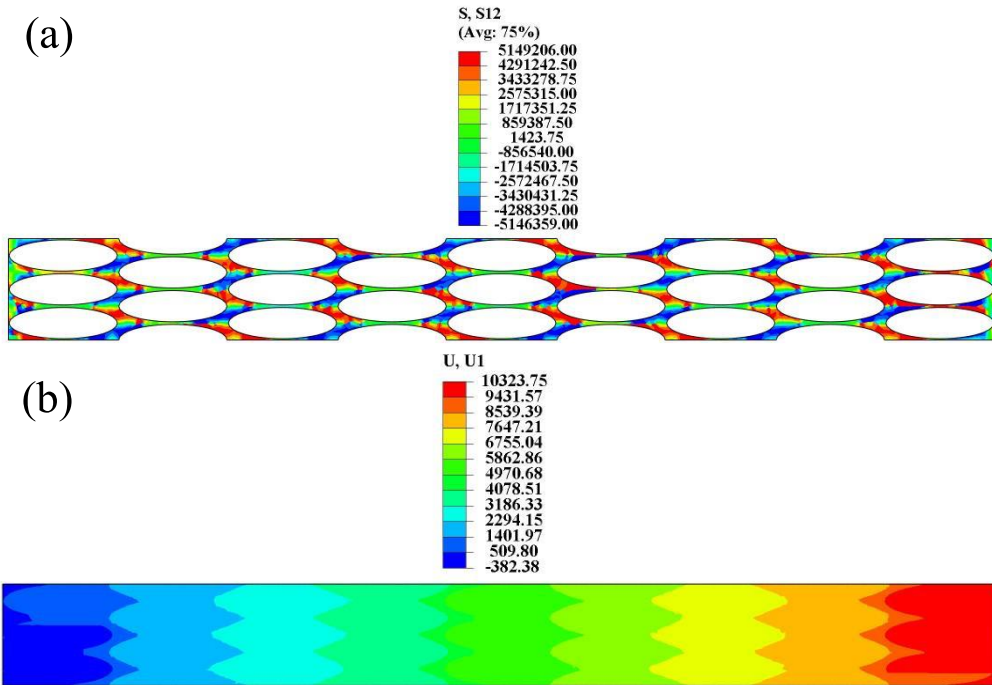


Fig. 8 The enamel's 1-directional mechanical distribution carried out for uniaxial tensile loading. (a) shear stress distribution. (b) 1-directional displacement distribution.

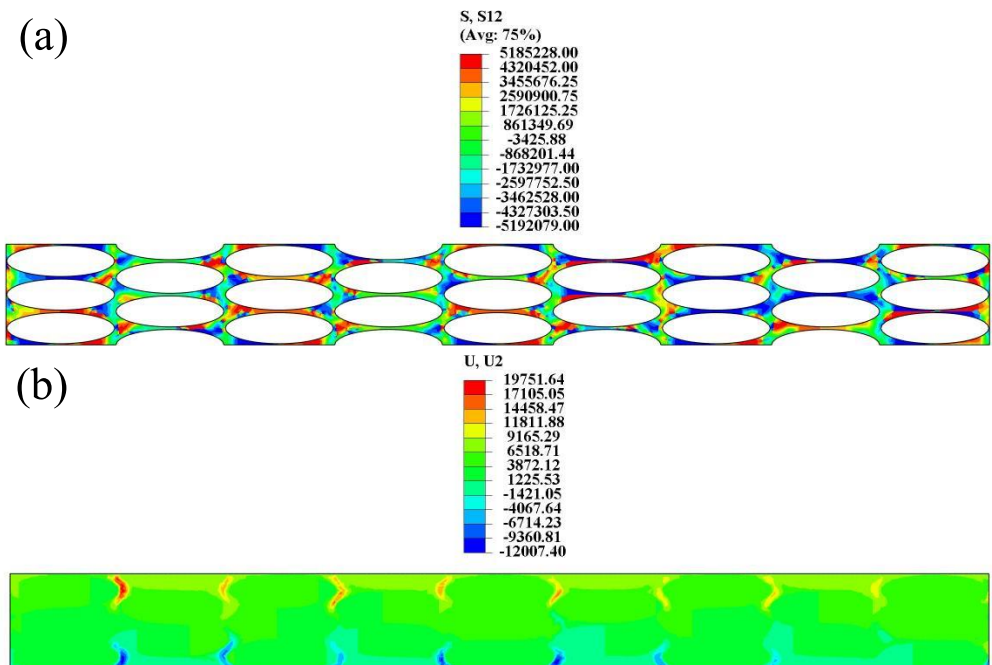


Fig. 9 The enamel's 2-directional mechanical distribution carried out for uniaxial tensile loading. (a) shear stress distribution. (b) 2-directional displacement distribution.

From what is shown in Figure 9(a), a strain concentration occurs on the enamel rods' 2-directional contact edge. Howbeit, similar strain distribution pattern as discussed in Figure 8(a) that shear stress concentration does not occur along edges perpendicular to the loading edge indicates a mechanism that can effectively resist fracture and crack propagation. From Figure 9(b) as the loading displacement gives there are deformation occurs along the inclusion's 1-directional edges. Such phenomena contend a possible local malposition occurs that might lead to sliding of the enamel rod and its surrounding organic protein.

Figure 10 presents the shear stress distribution of nacre protein and the 1-directional displacement distribution when a 1-direction loading is applied. Figure 11 presents the shear stress distribution of nacre protein and the 2-directional displacement distribution when a 2-direction loading is applied.

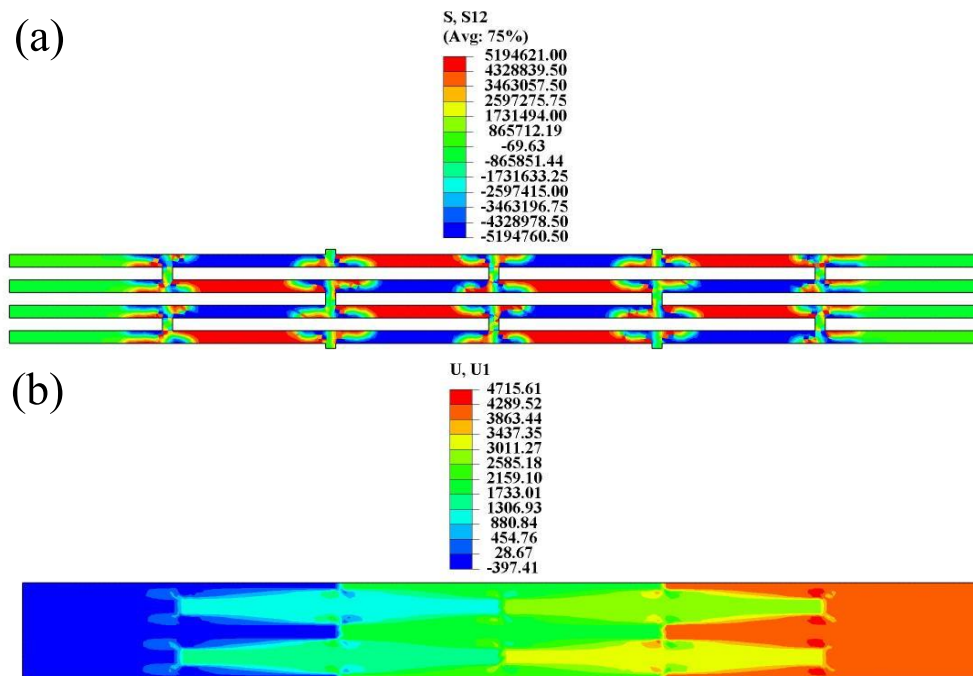


Fig. 10 The nacre's 1-directional mechanical distribution carried out for uniaxial tensile loading. (a) shear stress distribution. (b) 1-directional displacement distribution.

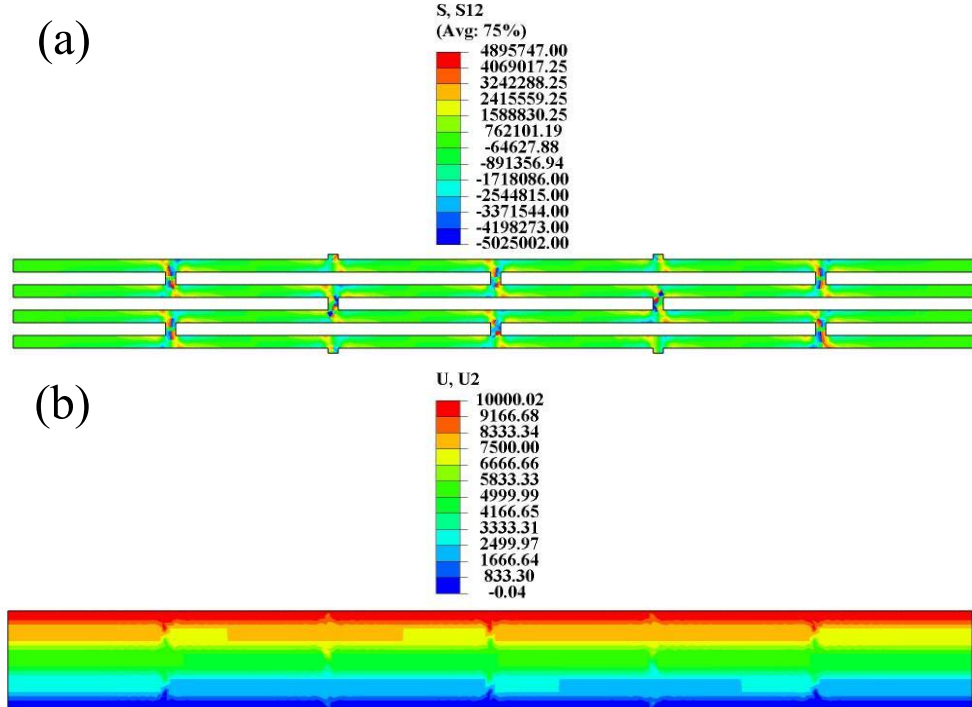


Fig. 11 The nacre's 2-directional mechanical distribution carried out for uniaxial tensile loading. (a) shear stress distribution. (b) 2-directional displacement distribution.

Similarly, as it is presented in Figure 10, one observes that a shear stress concentration occurs along the matrix longitudinal axis, but no concentration along the axis perpendicular to the loading direction, also indicating a fracture prevention mechanism. But the nacre's 2-directional loading shows a shear stress concentration perpendicular with the loading direction, contending a higher possibility for local failure. But the bonding hard inclusions could provide a robust cohesion to increase the local strength.

As it is mentioned in the preceding chapter, we adopt a perfectly plastic model for the matrix as investigating its possibility of local failure. Due to the displacement that can be directly measured by modern equipment, we present shear stress-displacement curves as guidelines for judgment of the local failure.

Here, Figure 12 presents the shear stress-displacement of the 1-directional loading of enamel and nacre, respectively.

From Figure 12 one discerns that the nacre matrix experience higher shear stress value with the ongoing displacements, which indicate that under 1-directional loading, the nacre structure is more likely to experience the local fracture. Hence, from the

fracture resistance perspective, the enamel structure is preferred under 1-directional loading.

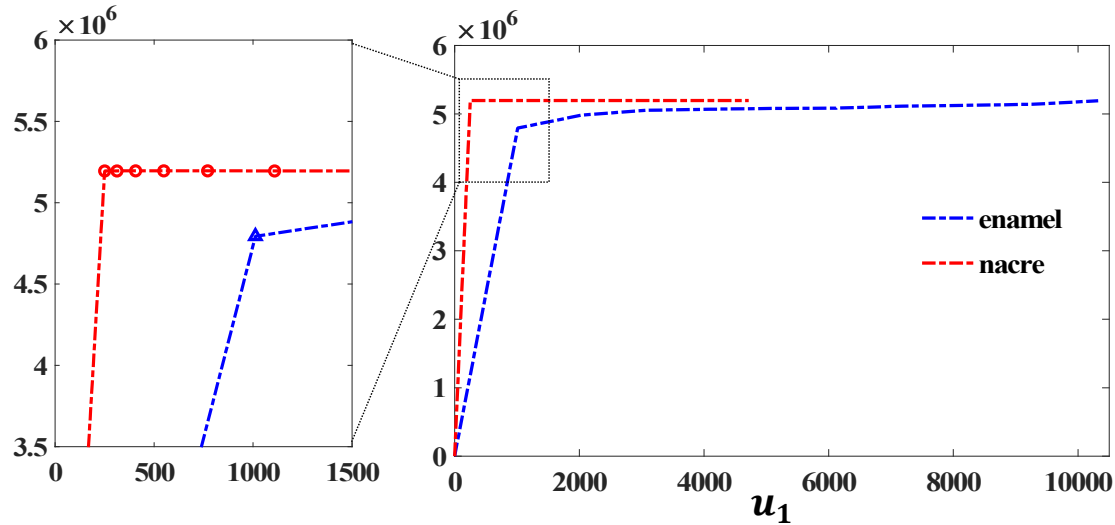


Fig. 12 The nacre and enamel structured composites' 1-directional shear stress-displacement diagram.

Also, Figure 13 presents the shear stress-displacement of the 2-directional loading of enamel and nacre, respectively.

Following a similar thought trace, as presented in Figure 13 a higher stress value occurs on enamel under 2-directional loading, indicating a higher possibility for local fracture on enamel under such loads. Thenceforth, a nacre structure is preferred preventing local failure.

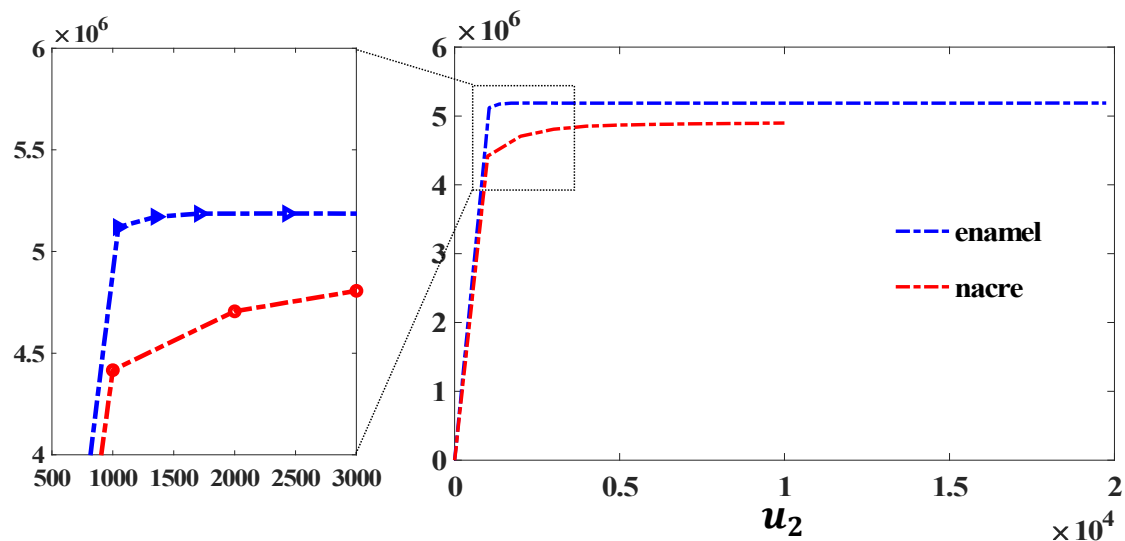


Fig. 13 The nacre and enamel structured composites' 2-directional shear stress-displacement diagram.

Optimization

Based on the previous discussions, we can adopt a basic guideline for designing a new structure exhibits high stiffness in both 1 and 2-directions, and high fracture resistance (low shear stress values on soft matrix) in both 1 and 2-directions: adopting the advantages of the structural displacement of both nacre and enamel in each direction. Hence, a new structural designation is presented as shown in Figure 14. The modelling of the structure carried out for simulations is shown in Figure 15.

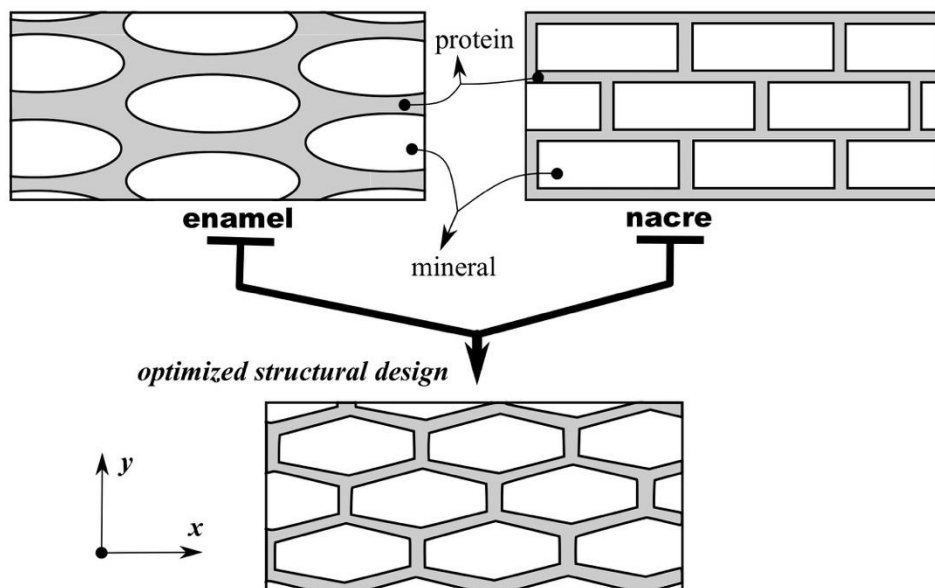


Fig. 14 Optimization process of the structural design based on the enamel and nacre microstructure.

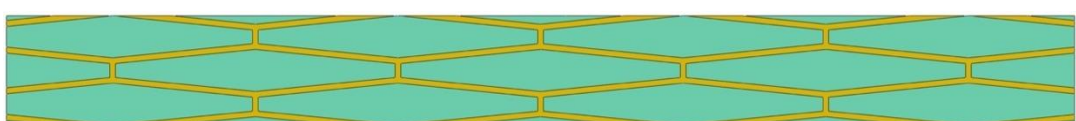


Fig. 15 Modelling of the optimized structure.

As the modeling presented, a verification for such an optimized structure's mechanical properties needed to be tested with simulations. We adopt the same thought trace as presented in the preceding part to calculate the 1 and 2-directional elastic moduli and its matrix shear stress-displacement curve with comparison to the nacre and enamel model, respectively.

The von Mises stress, 1-directional stress, and 1-directional strain distribution of the optimized structure undergoing 1-directional loading are shown as in Figure 16.

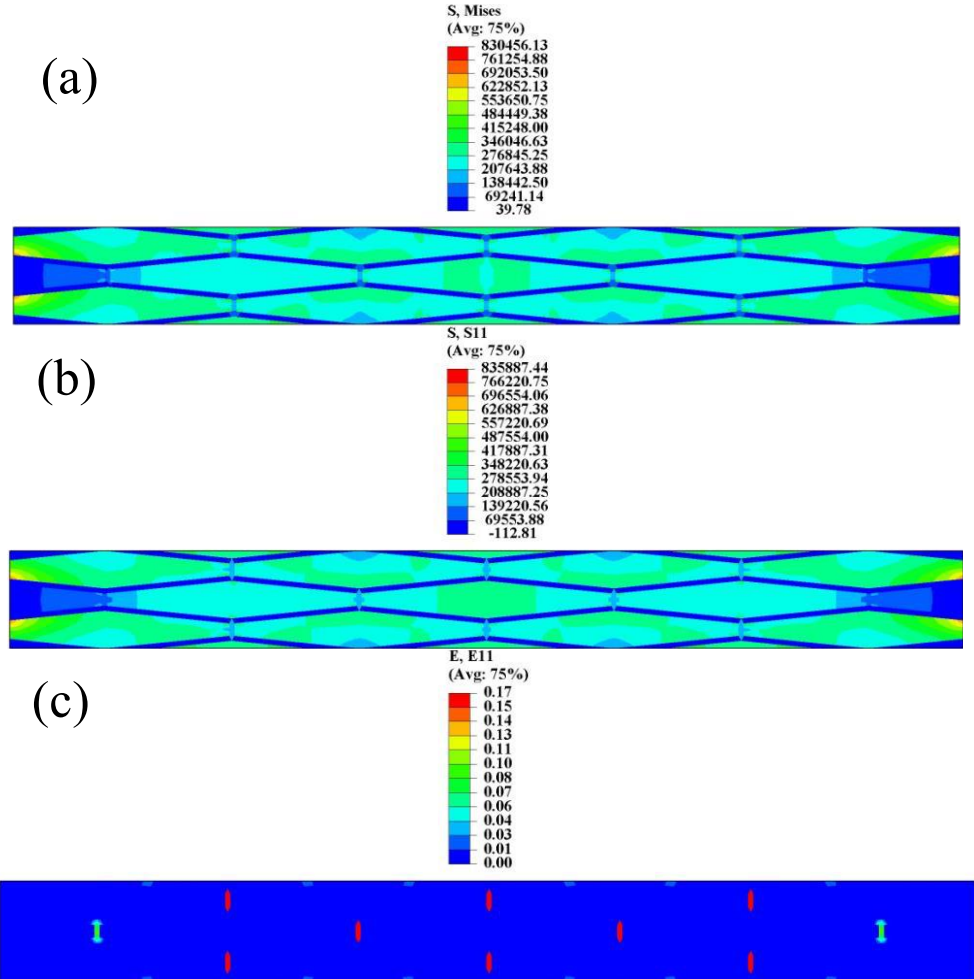


Fig. 16 The optimized structure's 1-directional mechanical distribution carried out for uniaxial tensile loading. (a) shear stress distribution. (b) 1-directional displacement distribution.

As presented in Figure 16, the 1-directional stress is the dominating stress as comparing Figure 16(a) with Figure 16(b). Generally, the 2-directional stress makes little effect on the total stress distribution. Furthermore, a local 1-directional strain concentration occurs while loading, howbeit the extended outline of the inclusions' shape could prevent longitudinal failure,

The von Mises stress, 2-directional stress, and 2-directional strain distribution of the optimized structure undergoing 2-directional tensile loading are shown as in Figure 17.

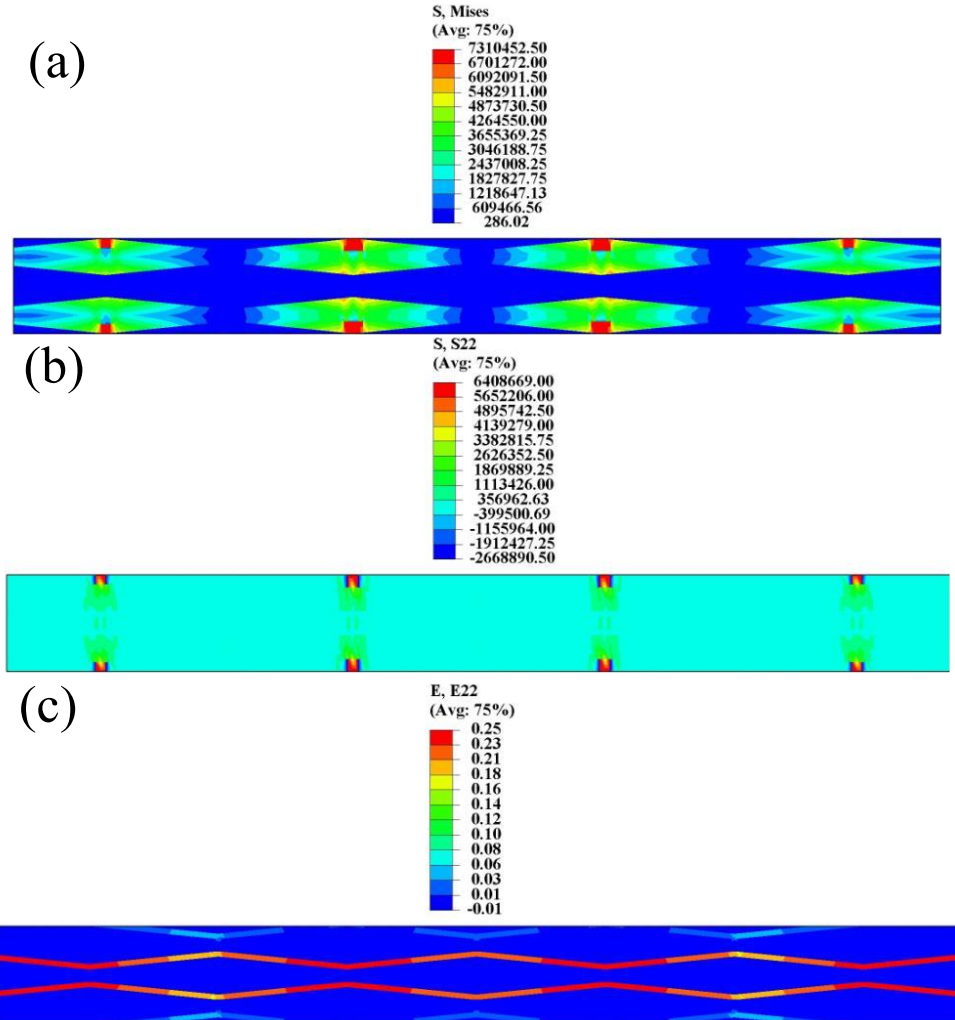


Fig. 17 The optimized structure's 2-directional mechanical distribution carried out for uniaxial tensile loading. (a) shear stress distribution. (b) 1-directional displacement distribution.

Similarly, one observes the 2-directional stress is not the main stress dominating the stress distribution of the whole structure comparing Figure 17(a) with Figure 17(b). Moreover, strain concentration along 1-directional edges occurs, indicating a possible form of the materials' failure.

Following previous steps, we calculate the elastic moduli for the optimized model in 1 and 2-directions and compare such results with the stiffness of the nacre and enamel model. The results are shown in Table 2 and as illustrated in Figure 18.

Structure	enamel	nacre	optimized structure
1-directional Stiffness	10611974.6923077	79478880.8205128	85044895.0769231 [Pa]
2-directional Stiffness	7946666.13612566	2603749.64921466	9657233.08900524

Tab. 2 The 1 and 2-directional stiffness calculation results of enamel, nacre, optimized structure, respectively.

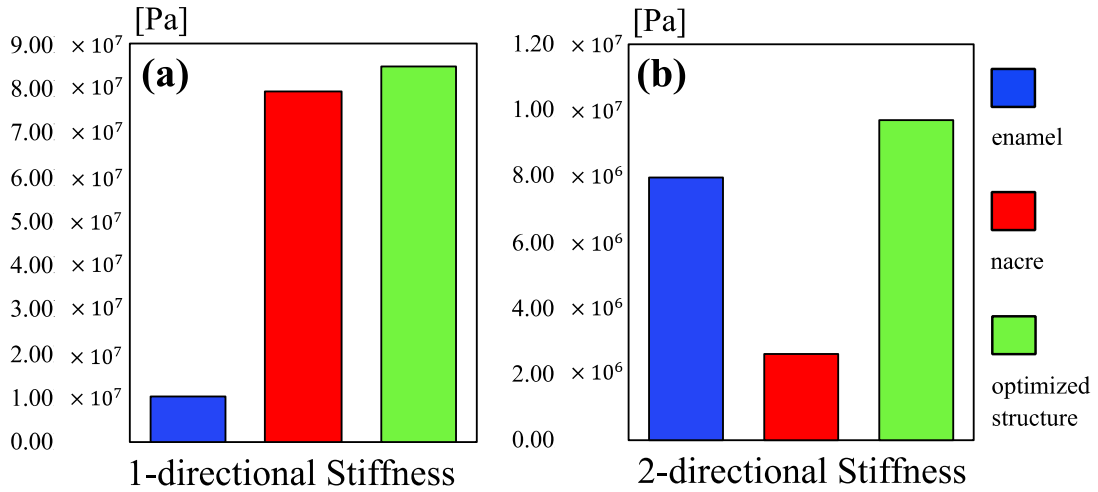


Fig. 18 The comparison of the structure's stiffness. (a) the 1-directional stiffness of nacre, enamel, and optimized model, respectively. (b) the 2-directional stiffness of nacre, enamel, and optimized model, respectively.

From the calculation results, one discerns that the optimized model robustly increases the stiffness in both 1 and 2-directions, respectively. Such increases, as mentioned, could be explained by the adoption of the characteristics of both nacre and enamel in both directions.

Subsequently, the possibility of local failure is hence be estimated by analyzing the shear stress distribution. As discussed previously, a perfectly plastic material model is adopted for the description of the soft matrix in the optimized model.

Figure 19 presents the shear stress distribution of the optimized model's matrix and the 1-directional displacement distribution when a 1-direction loading is applied. Figure 20 presents the shear stress distribution of optimized model's matrix and the 2-directional displacement distribution when a 2-direction loading is applied.

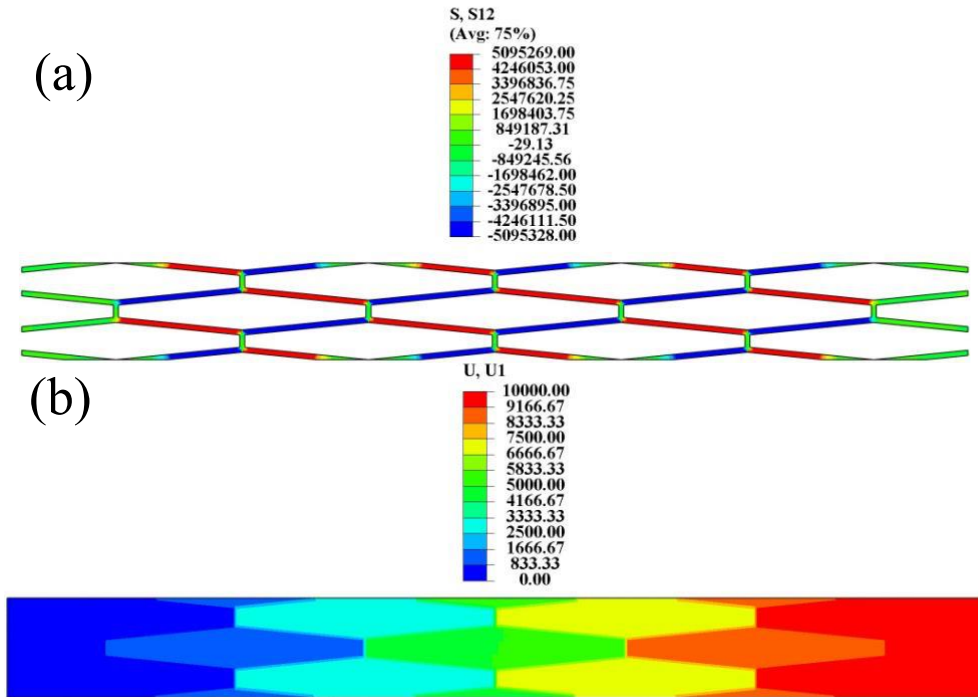


Fig. 19 The optimized structure's 1-directional mechanical distribution carried out for uniaxial tensile loading. (a) shear stress distribution. (b) 1-directional displacement distribution.

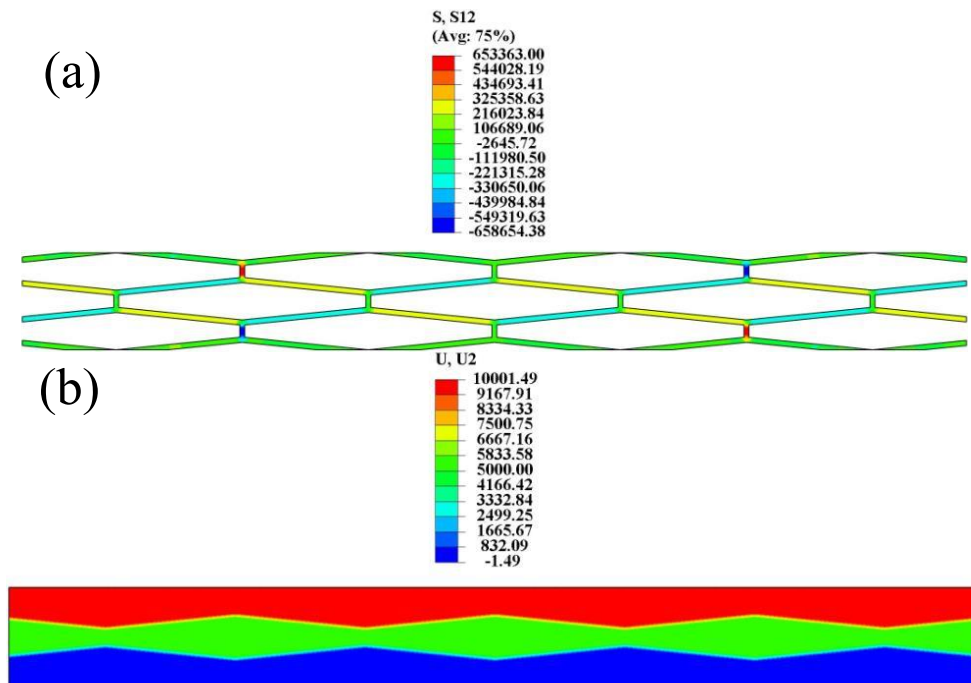


Fig. 20 The optimized structure's 2-directional mechanical distribution carried out for uniaxial tensile loading. (a) shear stress distribution. (b) 2-directional displacement distribution.

For both Figure 19(a) and Figure 20(a) indicate a high shear stress concentration along the loading direction. Such high shear stress concentration might indicate the

fracture pattern of the optimized model. Also, from what is shown in Figure 20(b), with Figure 17(c) indicating a deformation pattern in 2-directional loading.

Based on the calculation results, a shear stress-displacement curve is given in each direction as shown in Figure 21.

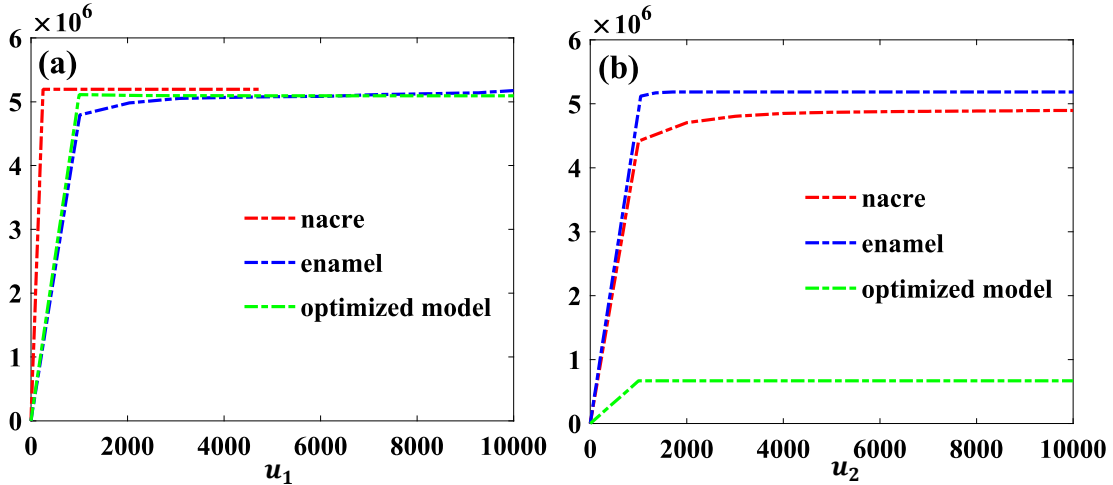


Fig. 21 The shear stress-displacement relationship. (a) the 1-directional curve of nacre, enamel, and optimized model, respectively. (b) the 2-directional curve of nacre, enamel, and optimized model, respectively.

Based on Figure 21(a), one can observe that the optimized model's shear stress is generally the same value as the enamel structure. Notwithstanding, the shear stress is greatly reduced pertaining to displacement under 2-directional loading for the optimized model comparing with nacre and enamel as shown in Figure 21(b). Such results indicate that the structural design is generally successful with regard to preventing the local failure, especially in the 2-directional as the shear stress value is greatly reduced from Figure 21(b). even the shear stress value is not greatly reduced, a generally similar value with the enamel also validates the design.

Conclusion

Biomaterials such as nacre and enamel display superior mechanical properties including high stiffness, high toughness, and fracture resistance. Such properties are employed through a specific hierarchical architecture composite, usually including a hard inclusion and soft matrix. Nacre and enamel both display such structure (Figure 1, Figure 2). To study such structures, we carry out simulations employ a perfect plasticity model for the soft matrix (Table 1), usually consist of protein. In the study, we

test the 1 and 2-directional elastic moduli for nacre and enamel, respectively (Equation 1-Equation 3). We also estimate the composites' fracture resistance through analyzing the soft matrix's shear stress, in which we employ a criterion that the material fails when the matrix shear stress reaches a critical value.

For the calculation of the elastic moduli of the two materials, a directional tensile loading is carried out and the Mises stress, directional stress, and strain are illustrated for enamel (Figure 3, Figure 4) and nacre (Figure 5, Figure 6). The calculation results show that the nacre structure exhibits higher stiffness in 1-direction and enamel exhibits higher stiffness in 2-direction (Figure 7). Also, based on the given criterion, under the tensile loading in the two directions, the shear stress of the soft matrix and the displacements of the whole composite's material is presented for enamel (Figure 8, Figure 9) and nacre (Figure 10, Figure 11). Based on such results, the shear stress-displacement curve of the two composites in 1-direction (Figure 12) and 2-direction (Figure 13) is given respectively. Such results show that local fracture is more likely to occur on nacre in 1-direction and on enamel in 2-direction.

The obtained results indicate that both the enamel and nacre both displays some superior properties in specified conditions, compared with the other. Thenceforth, a basic thought trace is established: we need to employ both the characteristics of the two composites in the two directions to create an optimized structure that displays superior mechanical behavior. Hence, an optimized model is presented (Figure 14) and modeled (Figure 15).

To investigate and verify the mechanical properties, we also carry out tensile loading in the two directions and present the Mises stresses, 1 and 2-directional stresses, 1 and 2-directional stresses for the optimized model (Figure 16, Figure 17). Calculation results contend the optimized structure displays higher stiffness in both the directions than enamel and nacre (Table 2, Figure 18), which validate the design of the structure. For what is more, to test its fracture resistance, we also calculate the optimized structure's soft matrix 1 and 2-directional shear stress and displacement distribution (Figure 19, Figure 20). Similarly, a shear stress-displacement diagram is given indicating that the optimized structure displays the same level of fracture resistance as enamel in the 1-direction (Figure 21(a)). Notwithstanding, such a structure greatly reduces the shear stress value in 2-direction, indicating less chance to fail to occur on the composites. The optimized design could provide decent insights and guidelines for future manufacturing and composites' structural design.

References

- [1] B. An. Constitutive modeling the plastic deformation of bone-like materials. *International Journal of Solids and Structures* 92–93 (2016) 1–8
- [2] B. An, Y. Liu, D. Arola, D. Zhang. Fracture toughening mechanism of cortical bone: an experimental and numerical approach. *J. Mech. Behav. Biomed. Mater.*, 4 (2011), pp. 983-992
- [3] An B., Zhang D. Bioinspired toughening mechanism: lesson from dentin. *Bioinspir. Biomim.*, 10 (2015), Article 046010
- [4] B. An, H. D. Wagner. Role of microstructure on fracture of dentin. *Journal of the Mechanical Behavior of Biomedical Materials*. Vol 59 (2016): 527-537. ISSN 1751-6161.
- [5] M. Mirkhalafa, A. Sunesarab, B. Ashrafib, F. Barthelata. Toughness by segmentation: Fabrication, testing and micromechanics of architected ceramic panels for impact applications. *International Journal of Solids and Structures* 158 (2019) 52–65
- [6] Godaa M. Assidib S. Belouettarb J.F. Ganghoffera. A micropolar anisotropic constitutive model of cancellous bone from discrete homogenization. *J. Mech. Behav. Biomed. Mater.*, 2012; Vol 16: 87-108
- [7] Zhang Z., Zhang Y., Gao H. On optimal hierarchy of load-bearing biological materials. *Proc. R. Soc. B*, 278 (2011), pp. 519-525
- [8] Su Y, Wang L, Wu X, Yi C, Yang M, Yan D, Cheng K, Cheng X. The spatial differences in bone mineral density and hip structure between low-energy femoral neck and trochanteric fractures in elderly Chinese using quantitative computed tomography. *Bone*, Vol 12
- [9] B. Wang, X. Hub, P. Lua. Modelling and testing of large-scale masonry elements under three- T point bending – Tough and strong nacre-like structure enlarged by a factor of 20,000. *Engineering Fracture Mechanics* 229 (2020) 106961
- [10] Horacio, Decanini & Juster, Allison & Latourte, Félix & Loh, Owen & Grégoire, David & Zavattieri, Pablo. (2011). Tablet-level origin of toughening in abalone shells and translation to synthetic composite materials. *Nature communications*. 2. 173. 10.1038/n
- [11] F Barthelat. Nacre from mollusk shells: a model for high-performance structural materials. *Bioinsp. Biomim.* 5 (2010) 035001 (8pp)

- [12] A. Ghazlana, T. Ngoa, T. Lea, T. Nguyena, A. Remennikov. Blast performance of a biomimetic panel based on the structure of nacre – A numerical study. *Composite Structures* 234 (2020) 111691.
- [13] A. Shi, Y. Li, W. Liu, J. Xu, D. Yan, J. Lei, Z. Li. Highly thermally conductive and mechanically robust composite of linear ultrahigh molecular weight polyethylene and boron nitride via constructing nacre-like structure. *Composites Science and Technology*
- [14] D. Bajaj, D. Arola. Role of prism decussation on fatigue crack growth and fracture of human enamel. *Acta Biomaterialia* 5 (2009) 3045–3056.
- [15] M. Yahyazadehfar, D. Bajaj, D. Arola. Hidden contributions of the enamel rods on the fracture resistance of human teeth. *Acta Biomaterialia* 9 (2013) 4806–4814
- [16] M. Yahyazadehfar, D. Arola. The role of organic proteins on the crack growth resistance of human enamel. *Acta Biomaterialia* 19 (2015) 33–45.
- [17] N. Zhang, X. Wang, W. Xiang, Y. Zhong, F. Yana, B. Jiang. Hierarchy structure and fracture mechanisms of the wild wolf tusk's enamel. *Materials Science & Engineering C* 106 (2020) 110277.
- [18] J. Koldehoff, M. V. Swain, G. A. Schneider. The geometrical structure of interfaces in dental enamel: A FIB-STEM investigation. *Acta Biomaterialia* 104 (2020) 17–27.

SECTION IV

An investigation of the elastoplastic nature of ITD on the toughness of the dentin microstructure

Abstract

Dentin is an essential part in human tooth that displays superior mechanical behaviors such as high stiffness and toughness relative to its lightweight, which could be attributed to its microscopic structure. Here, we adopt elastic and perfectly plastic model for ITD, and ductile damage evolution model for material failure. We calculate the stiffness of the dentin through consider it as composite materials. The tensile loading simulation indicate that dentin structure with plastic ITD will generate strain concentration along the four corners on ITD bonging PTD. The plasticity will reduce the forces acting on the structure. There are crack occurs on PTD initiated along the DT edge to the axis perpendicular to the loading direction, which corresponds to the stress concentration as on the unit cell model. There are wavy cracks on the ITD nearing the bonding interface between ITD and PTD. Most generated cracks evolved from the DT edge propagating on PTD till further on ITD. The ITD plasticity makes the stress-strain more evenly distributed on the structure in crack propagation. The quantitative results indicate the ITD plasticity can reduce the stress on PTD as to resist crack growth but make little effect on the stress of ITD as the growing strain. The ITD plasticity makes little variation on the shear stress distribution on the bonding interface, indicating such nature does not contribute to the debonding effect as a major role.

Keywords: biomechanics; biomaterials; composite materials; dentin; microstructure

Introduction

Biomaterials display superior mechanical behaviors adjusting to its loading conditions with millions of years of evolution. Tooth, as one of the most common characters seen from most creatures, exhibits high fracture resistance, containing enamel and dentin [1]. The enamel and dentin exhibit extremely different structures containing different chemicals adjusting to their different functions. The dentin evolving to convey nutrition as to supply the enamel and the whole tooth structure [2]. Also, it will absorb energy from enamel from chewing as the cracks propagating in enamels. The dentin microstructures consist of void rounded by hard materials embedded in soft materials [2]. Most biomaterials display plasticity as to resist failure. The biomaterials can be depicted by multiple models including the Drucker-Prager yield function ([3], [4], [13], [14], [15], [16], [17]). The fracture and crack growth can also be depicted by many models ([5], [6], [7]). In fine, many developed mechanical models can be adopted for delineating the biomaterials behavior.

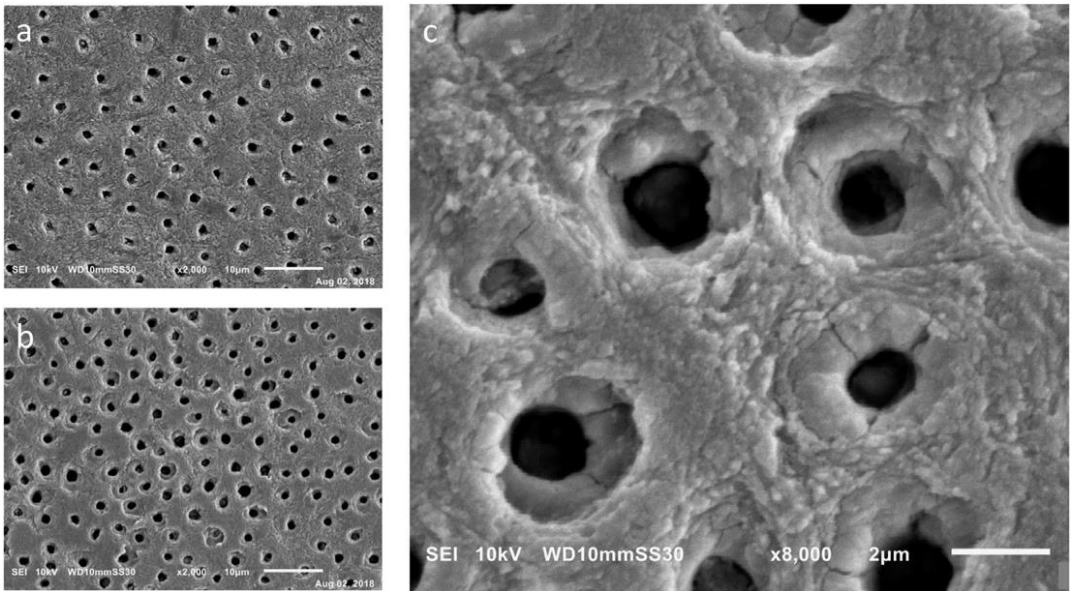


Fig. 1 SEM photos of the dentin microstructure, taken by A. Nazari *et al.*

Specifically, dentin structure mechanical behavior is well studied through experimental approaches ([9], [10]). The measured Young's Modulus, Yield stress, etc. from published resources is adopted in our study. The zoomed view of SEM photos shows good details of the dentin microstructure ([11], [12]). From the SEM photos as given in Fig. 1, we observe basic characteristics of the dentin microstructure: consisting of small voids surrounded by larger circular edges, further embed in matrix materials. The fracture behavior is comprehensively studied by An with the adoption of the Drucker-Prager criterion ([13], [15], [16], [17]). Notably, two types of fracture: cracks

occur on PTD initiated on the DT edge, which is also detected through SEM photos ([11], [12]); and the cracks propagated along with the ITD and PTD bonding interface caused by the elastic moduli mismatch [13]; are specifically detected through the work by An through numerical approaches.

As studied, the dentin and other biomaterials can be seen as composites consisting of materials with different properties. With the previous introductions, the plasticity of the dentin can be elicited as to study the fracture behavior. The elastoplastic behavior of composite indicates their mechanical behaviors ([18], [19], [20]). In our approaches, we follow the basic modeling strategy as previous studies conducted by An ([13], [15], [16], [17]). The main focuses are on the investigation of the ITD elastoplastic nature as its functions in affecting the composite's stiffness and toughness. To simplify, we adopt perfectly plasticity for ITD and ductile damage model for evolution. The approaches may not perfectly satisfy the experimental results, howbeit still offer decent insights for investigations of the ITD plasticity on dentin microstructure.

Method

2.1 Stiffness and strength

2.1.1 Elastic ITD

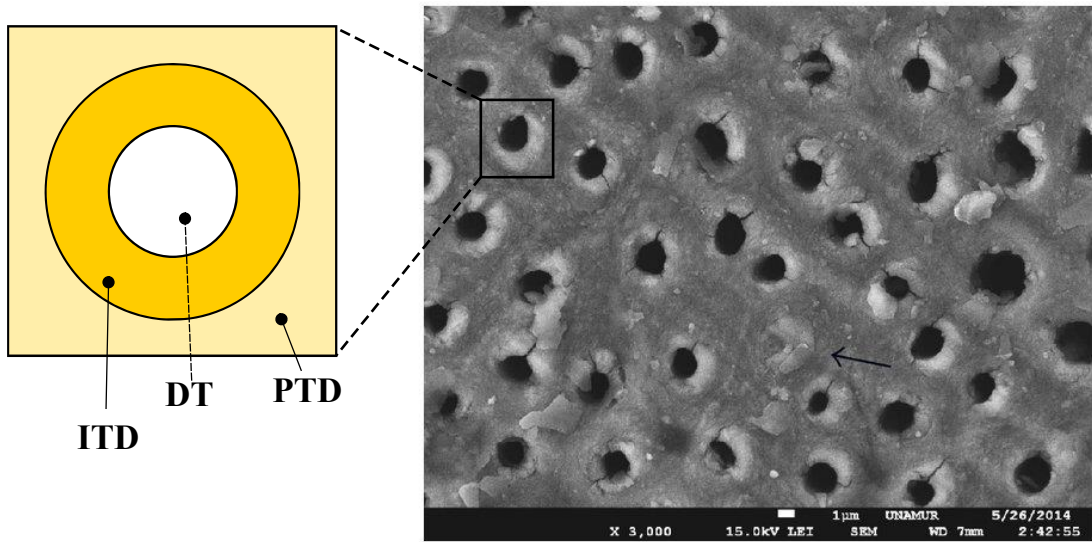


Fig. 2 Schematic view for the basic modelling strategy of the dentin unit cell, nominating each part as shown. The SEM photo is taken by A. Namour *et al.*

As discussed in §1, preceding studies show that the dentin structure involves a special hierarchical structure include a void nominated as Dentin Tubule (DT) surrounded by a round of hard materials called Inter-Tubular Dentin (ITD), and embedded in soft materials called Peri-Tubular Dentin (PTD). The microscopic scale dentin is generally consisting of thousands of such similar structures, which we considered as a “unit cell” for the structure. To investigate the mechanics of the dentin, we model such a unit cell as shown in Fig. 2 for simulations and calculations.

Initially, the dentin microstructure can be seen as composite materials with bonded materials of different modulus. To calculate the stiffness of such a composite structure, we carry out loadings on the unit cell structure as shown in Fig. 3. Note that the boundary conditions can be written as:

$$\begin{cases} y = 0: u_2 = 0 \\ x = \pm m: u_1 = 0 \\ y = n: u_2 = +1 \end{cases} \quad (1)$$

With the boundary conditions, we load the unit cell with a 2-directional unit displacement. With the loading, we can calculate the mean stress and mean strain in the 2-direction as:

$$\bar{\varepsilon}_y = \frac{u_y}{m} \quad (2)$$

$$\bar{\sigma}_y = \sum_{x=0}^a \frac{R_y(x, n)}{m} \quad (3)$$

Henceforth, the elastic modulus of the composite materials as:

$$E_y = \frac{\bar{\sigma}_y}{\bar{\varepsilon}_y} \quad (4)$$

As introduced in §0, we know that the ITP and PTD have different Young's modulus, indicate different stiffness. Here, we present parameters for the dentin's ITP and PTD as shown in Tab. 1 and Tab. 2 based on previous studies ([14], [15]). Note that the modulus value is chosen within an experimental data range and the yield stress is neglected in 2.1.1 as considering an elastic ITD.

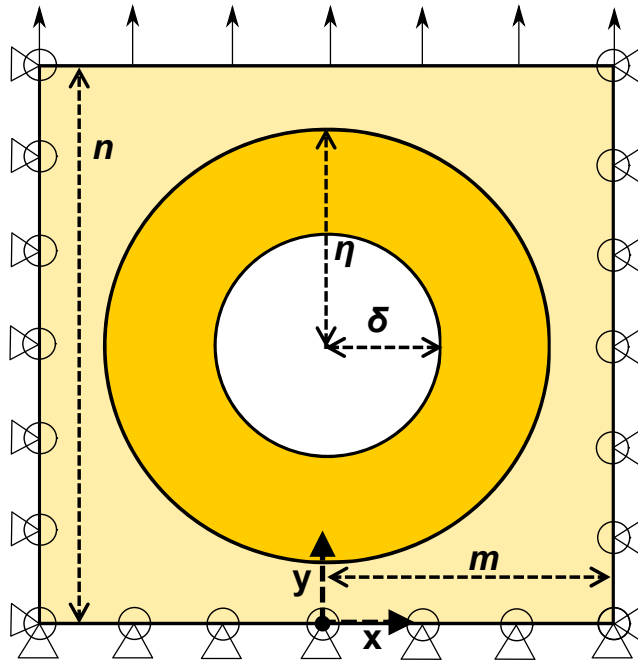


Fig. 3 Schematic illustration of the unit cell undergoing mechanical loadings for calculation of the composite's Young's modulus. Note that the geometric parameters: $\delta = 2$, $\eta = 4$, $m = 5$, $n = 2m$, in μm . Note that x axis is also recognized “1-direction”, y axis is also recognized “2-direction”.

Youngs modulus	Poisson's ratio
200GPa	0.3

Tab. 1 The mechanical parameter for PTD.

As given in Tab. 1, the PTD is considered as a pure elastic material.

Youngs modulus	Poisson's ratio	Yield stress
20GPa	0.3	70MPa

Tab. 2 The mechanical parameter for ITD, where the yield stress denote the plastic attribute of ITD, which is considered separately.

2.1.2 Plastic ITD

From §0 we know that the plastic nature of the dentin ITD is adopted or ignored with regards to the specific topics studied by previous scholars. In this part, to delineate such an effect on the composite's stiffness, we adopt the plastic nature of the ITD compared to 2.1.1. Note that a perfectly plastic model is adopted to simplify the estimation and neglect the complex hardening or softening effect.

Here, for the strain of the plastic model can be depicted as:

$$\boldsymbol{\varepsilon} = \boldsymbol{\varepsilon}^e + \boldsymbol{\varepsilon}^p \quad (5)$$

Therefore, the stress can be written as

$$\boldsymbol{\sigma} = \mathbf{C} : (\boldsymbol{\varepsilon} - \boldsymbol{\varepsilon}^p) \quad (6)$$

As mentioned, a perfect plasticity model is adopted. When the stress is within the yield strength, such condition is represented as the plastic strain does not change:

$$d\boldsymbol{\varepsilon}^p = 0 \quad (7)$$

When the stress reaches the yield strength in tension, in uniaxial problem, the plastic strain can only increase and the 2-directional stress equals the yield:

$$d\boldsymbol{\varepsilon}^p > 0, \quad \frac{\sigma_{22}}{\sigma_Y} = 1 \quad (8)$$

Where σ_Y denotes the yield stress, and σ_{22} is the 2-directional stress.

We adopt such a model just to study how the plasticity might influence the dentin's stiffness in this section. Here, we apply the yield stress as given in Tab. 2 for the ITD and carrying out simulations for the same model as shown in Fig. 3. To specify, the PTD is considered as a purely elastic material due to its higher stiffness, the yield stress effect is not required in the study of composite's stiffness. Note that both the simulations in 2.1 are carried out in Abaqus/CAE 2017. For the meshing, we adopt the Plane strain assumption, with mesh-type CPE4.

2.2 Toughness and fracture

2.2.1 Elastic ITD

Numerous studies ([2], [13], [15], [16], [17]) indicate that dentin structure displays high fracture resistance and such specific mechanical property is widely studied both experimentally and numerically. Here, a simplified failure model for crack propagation is adopted as an energy-based, linear softening, hybrid mode damage evolution model, where the criterion for damage initiation is when the maximum principal stress reaches a specific value.

For the damage evolution, we adopt a ductile damage model, in which the equivalent plastic strain is a function of strain rate and stress triaxiality:

$$\dot{\epsilon}_D^p = \dot{\epsilon}_D^{pl}(\eta, \dot{\epsilon}^p) \quad (9)$$

Where the stress triaxiality is a division of hydrostatic stress to von Mises stress:

$$\eta = \frac{J_1}{\sigma_v} \quad (10)$$

And the damage evolves when:

$$w_D = \frac{d\dot{\epsilon}^p}{\dot{\epsilon}_D^{pl}(\eta, \dot{\epsilon}^p)} = 1 \quad (11)$$

In which w_D is an increment variable increasing with plastic strain:

$$\Delta w_D = \frac{\Delta \dot{\epsilon}^p}{\dot{\epsilon}_D^{pl}(\eta, \dot{\epsilon}^p)} \geq 0 \quad (12)$$

For the damage initiation model, the maximum principal stresses for PTD and ITD are shown in Tab. 3 and Tab. 4, respectively.

Youngs modulus	Poisson's ratio	Maximum principal stress
200GPa	0.3	86MPa

Tab. 3 The parameters of PTD for fracture simulation.

Youngs modulus	Poisson's ratio	Maximum principal stress
20GPa	0.3	10MPa

Tab. 4 The parameters of ITD for fracture simulation.

For our model, the equation for the energy of crack propagation:

$$KE = \int_{a_0}^a (G - R) da \quad (13)$$

In which G is the energy dissipative rate, R is the fracture energy denoted as $R = G_{ic}$. In our model, we adopt that $G_{1c} = G_{2c} = G_{3c}$ as given in Tab. 5 and Tab. 6.

The crack propagation rate is given as:

$$\dot{a} = \sqrt{\frac{2\pi}{\alpha}} \cdot \sqrt{\frac{E}{\rho}} \cdot \left(1 - \frac{a_0}{a}\right) \quad (14)$$

As mentioned, in our model, we adopt a linear damage model, hence we have $\alpha = 1$ as shown in Tab. 5 and Tab. 6.

Normal mode	Shear mode		
Fracture energy	Fracture energy (1-direction)	Fracture energy (2-direction)	Power
43000	43000	43000	1(Linear)

Tab. 5 The parameters of PTD for fracture simulation.

Normal mode	Shear mode		
Fracture energy	Fracture energy (1-direction)	Fracture energy (2-direction)	Power
5000	5000	5000	1(Linear)

Tab. 6 The parameters of ITD for fracture simulation.

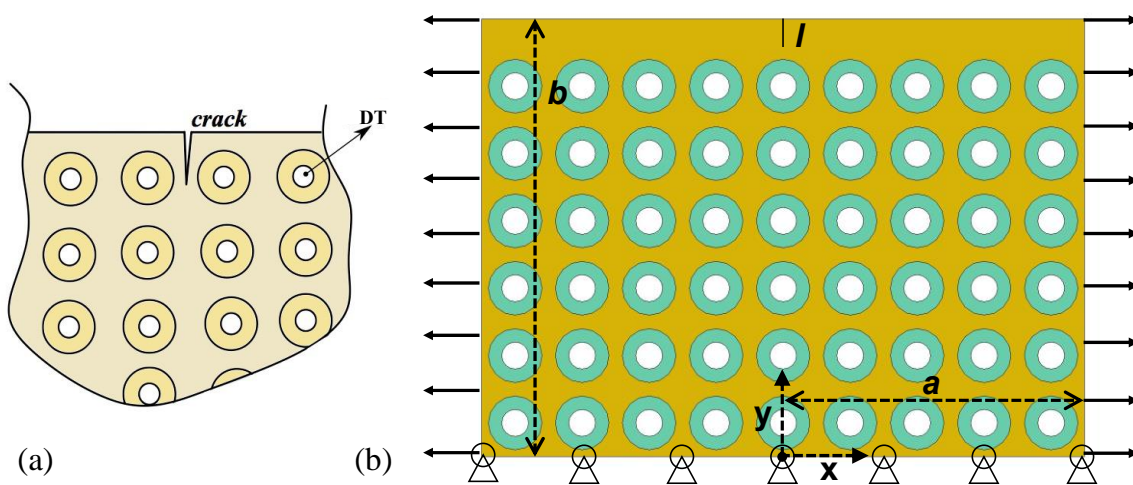


Fig. 4 Schematic view of the mechanical model carried out for fracture simulation.

(a) Schematic for the crack initiation on dentin. (b) Mechanical model for the fracture simulation, in which the 1-directional loading is $u_{-1} = -1$, $u_{+1} = 1$.

Note that the initial crack length $l = 5$, in μm . Note that x axis is also recognized “1-direction”, y axis is also recognized “2-direction”.

For 2.2.1, we adopt the same strategy as in 2.1.1, that the plastic nature of ITD is neglected. Hence, a fracture occurs on ITD and is considered as elastic failure. The mechanical model carried out for fracture of the dentin microstructure is shown in Fig. 4. Note that the model consists of 54 “unit cells” as shown in Fig. 3.

The boundary conditions for our mechanical model can be mathematically written as:

$$\begin{cases} y = 0: u_2 = 0 \\ x = \pm a: u_1 = \pm 1 \\ y = b: F_s = 0 \end{cases} \quad (15)$$

In which F_s denotes the surface force acting on the edge.

2.2.2 Plastic ITD

In this part, we adopt similar strategies as given in 2.1.1 to 2.1.2. We neglect the ITD’s plastic nature in 2.2.1. Here, we set the ITD as perfectly plastic material as given in Tab. 2. With the set plastic ITD and elastic PTD, we carry out the same simulation with the same mechanical loadings as given in Fig. 4 and Eq. 15, with the same initial crack, with length $l = 5$.

Note that both the simulations in 2.2 are carried out in Abaqus/CAE 2017. For the meshing, we adopt the Plane strain assumption, with mesh-type CPE4.

Results and discussion

3.1 Stiffness and strength

3.1.1 Elastic ITD

With the mechanical loadings as given in Fig. 3 and Eq. 1, we obtain results as shown below. From Fig. 5 and Fig. 6 we got the strain and stress distribution on the dentin unit cell from the first and last step as given from (a) to (b).

From the strain distribution as given in Fig. 5 one can observe that applied with an elastic ITD, the 2-directional strain is concentrated along the central axis in 2-direction, while displays a generally low value along the on the ITD. Albeit the strain is concentrated along the 1-direction's edge on the PTD along with the DT.

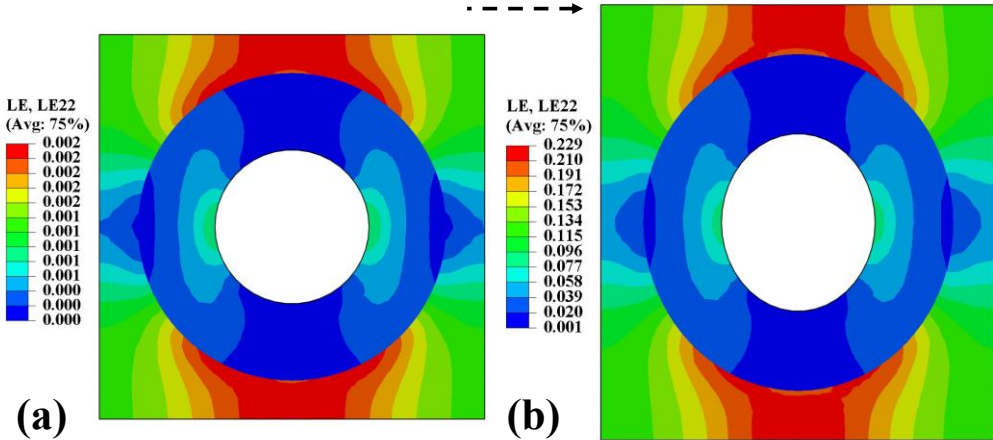


Fig. 5 The 2-directional strain distribution of the unit cell under uniaxial loading, with elastic ITD. (a) First step. (b) Last step.

From the 2-directional stress distribution as given in Fig. 6, one discerns that the stress is concentrated along the 1-direction along the DT edge on PTD. Such a phenomenon indicates higher possibilities for the fracture to occur on PTD along the axis perpendicular to loading directions under tensile loadings. The 1-directional stress value on ITD is low compared with the total stress distribution. We also find that the 2-directional stress is more evenly distributed with the loadings from (a) to (b).

The elastic ITD exhibits similar stress-strain distribution from the beginning to the end of the loading as shown from (a) to (b) in Fig. 5 and Fig. 6.

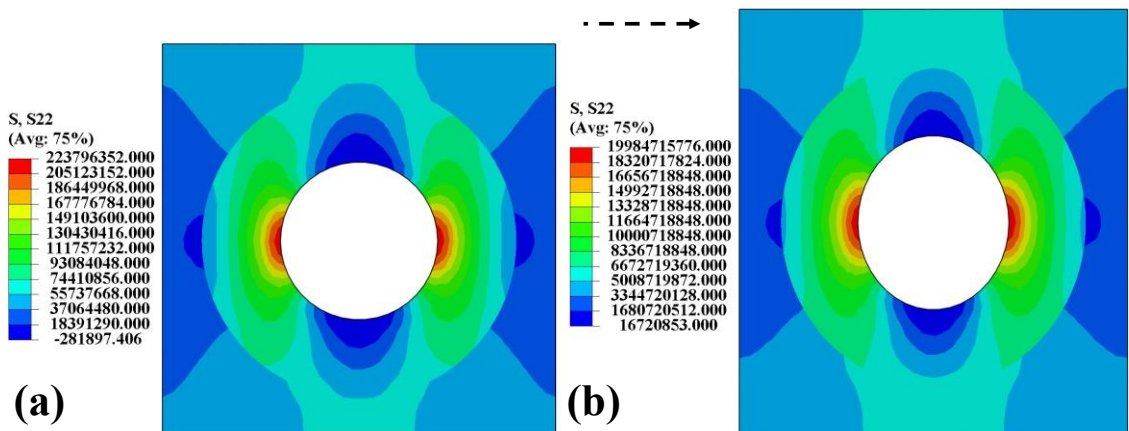


Fig. 6 The 2-directional stress distribution of the unit cell under uniaxial loading, with elastic ITD. (a) First step. (b) Last step.

3.1.2 Plastic ITD

Here, as given from Eq. 5 to Eq. 8 and in Tab. 2, we adopt a perfectly plasticity model for ITD for the same uniaxial loading to check how plasticity influences the 2-directional stress-strain distribution as compared with Fig. 5 and Fig. 6. As shown in Fig. 7, we discern that the 2-directional strain has the same distribution in the first step with the elastic ITD as compared with Fig. 5(a). However, as the loading keeps, the plastic ITD displays a totally different strain distribution, shown in Fig. 5(b). We observe that the strain is robustly concentrated along the PTD edge on the four corners. Also, the total strain value is increased with the plastic effect. For what is more, the total strain is distributed concentrating on the four edges tangent to the PTD circular edge. Such a phenomenon indicates a protection mechanism for the ITD to constrain the failure.

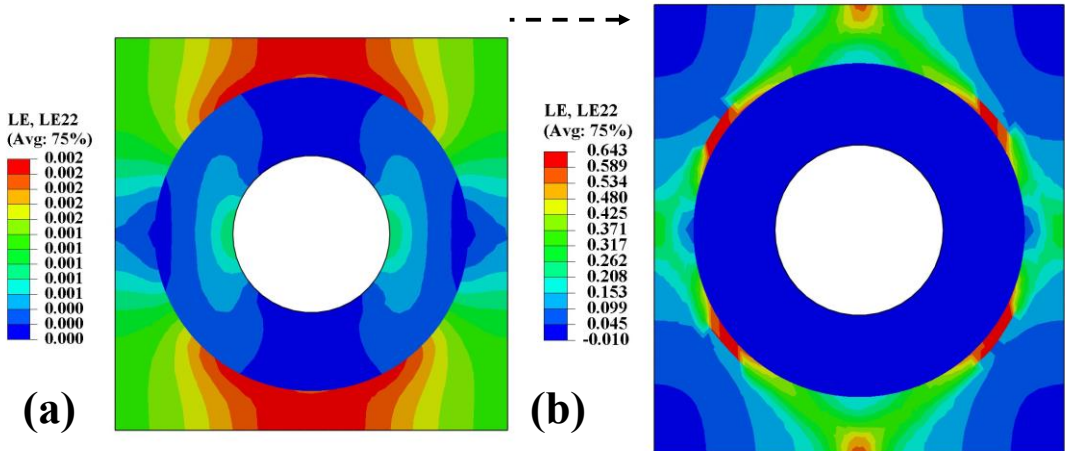


Fig. 7 The 2-directional strain distribution of the unit cell under uniaxial loading, with perfectly plastic ITD. (a) First step. (b) Last step.

As mentioned, comparing Fig. 7(b) with Fig. 5(b) one discern extremely different strain distributions. To delineate such, we calculate the plastic strain of the unit cell as shown in Fig. 8 From Fig. 8(b) and Fig. 7(b) we deduce that plastic strain plays a major role in the total 2-directional strain based on the fact that the two figures exhibit similar patterns. Moreover, from Fig. 8 we observe that the plastic strain initiated along the lines that tangent to the PTD circular edge and evolving from closer to the 2-direction's concentration to a more evenly distributed pattern. Such plastic strain could help explain how the plastic nature could help restrain the fracture.

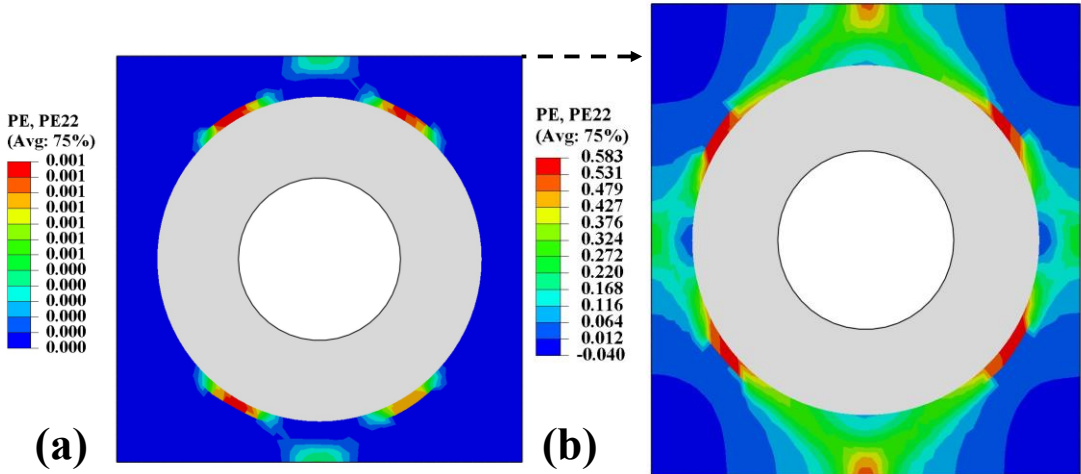


Fig. 8 The 2-directional plastic strain distribution of the unit cell under uniaxial loading, with perfectly plastic ITD. (a) First step. (b) Last step.

Similarly, we also present how the 2-directional stress evolves on the unit cell with a plastic ITD. As comparing Fig. 9(a) with Fig. 6(a) we also discern the same stress distribution at the beginning stage. However, as given in Fig. 9(b) and Fig. 6(b), we observe that the total 2-directional stress value is greatly reduced due to the plastic nature of ITD. The stress is also more evenly distributed among the unit cell. Notably, the 2-directional stress is also highly concentrated along the 1-direction on the PTD, but such stress value is highly reduced compared with Fig. 6(b). Though the PTD material properties remain the same, the ITD properties' change contends an alleviation of the stress concentration on the PTD.

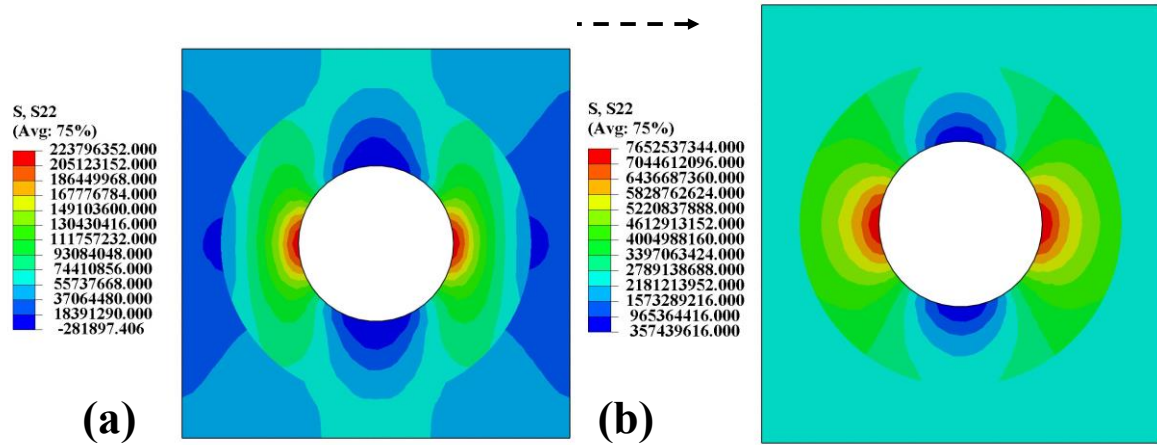


Fig. 9 The 2-directional stress distribution of the unit cell under uniaxial loading, with perfectly plastic ITD. (a) First step. (b) Last step.

Based on Eq. 2 to Eq. 4 we obtain results from Fig. 10, indicating how stiffness evolve with the loading.

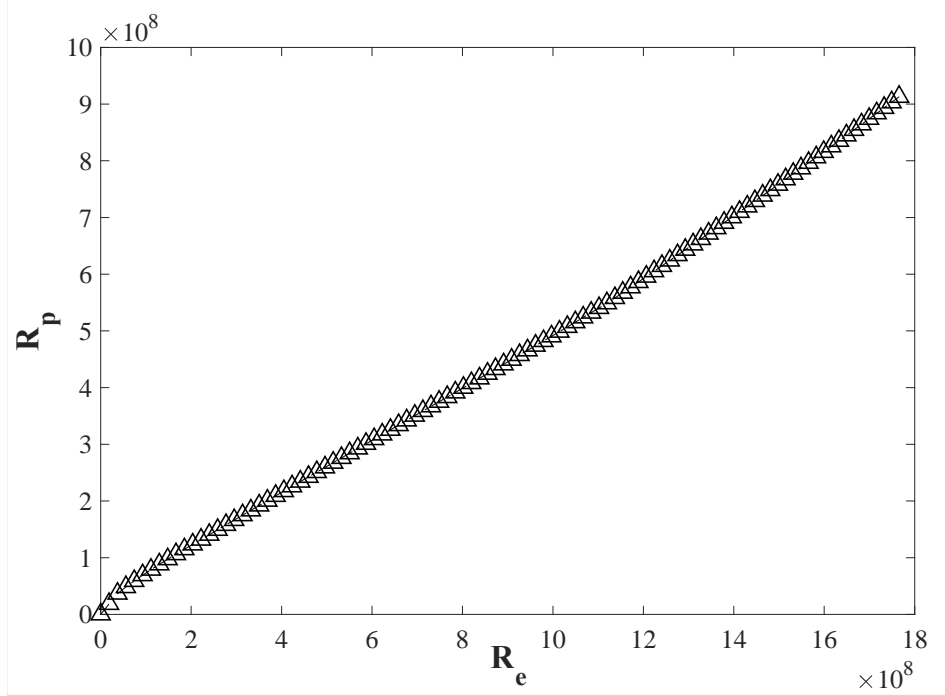


Fig. 10 The relationship between the reaction force with the model of elastic ITD and perfectly plastic ITD, in which R_e represents reaction force for elastic ITD and R_p represents reaction force for plastic ITD. Note that the unit is 10^{12} N.

From Fig. 10, the slope $\frac{dR_p}{dR_e}$ initially grows and the steepness decreases in the when R_e reaches the value around 3, the slope started to decrease, indicating the ITD's plastic nature started to make effect on the loading. When R_e reaches the value around 12, it started to increase again yet the value is still below 1 indicate that $R_p < R_e$, we can explain such a phenomenon as the ITD's plastic effect does not exhibit as evident as the beginning stage yet still make an effect on the composite's total stiffness.

3.2 Toughness and fracture

3.2.1 Elastic ITD

Based on the damage evolution model (Tab. 3 – Tab. 6) and mechanical loadings (Fig. 4), we obtain results as given indicating how fracture initiate and develops on the dentin structure as shown below. Fig. 11 – Fig. 13 shows the fracture evolution of the 1-directional stress distribution on the dentin structure.

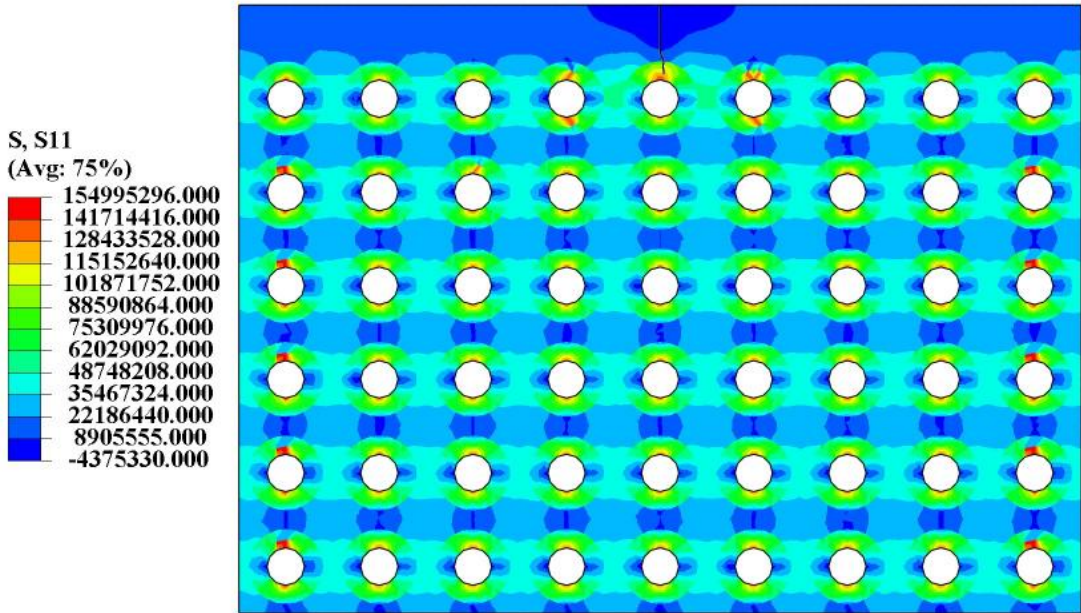


Fig. 11 The 1-directional stress distribution of preliminary stage of the crack propagation on dentin structure, with elastic ITD.

Fig. 11 shows that the 1-directional stress generally has the same distribution around the DT referring to such distribution on unit cell (Fig. 6). Notwithstanding, there is some detectable stress concentration on the PTD along the 2-direction near the initial crack. Such a phenomenon could be explained by the initial crack propagation effect, in which the crack surrounding area absorbs more energy from fracture.

From Fig. 12 one observes how cracks initiated on the dentin microstructure. From the zoomed view on the right top part, we detect the DT bonding the initial crack has a stress concentration on the PTD in the lower part. Also, from the neighboring DT one observes cracks propagated along the axis perpendicular to the loading directions, which have been discussed in 3.1. Such a similar pattern is also detected on the other zoomed views in Fig. 12 which is studied by other scholars ([2], [12], [13]). For what is more, the 1-directional stress value is lower on PTD under same direction's loading, observed from the two down zoomed views. Such distribution is also explained in 3.1 as tensile loading on the unit cell. Aside from the perpendicular directional cracks, there are cracks on ITD close to the PTD with a wavy shape in the right-top and down zoomed views. Such cracks could indicate a debonding between the ITD and PTD, but not the exactly debonding effect explained as elastic modulus mismatch ([15], [16]), could be attributed to the mechanical model.

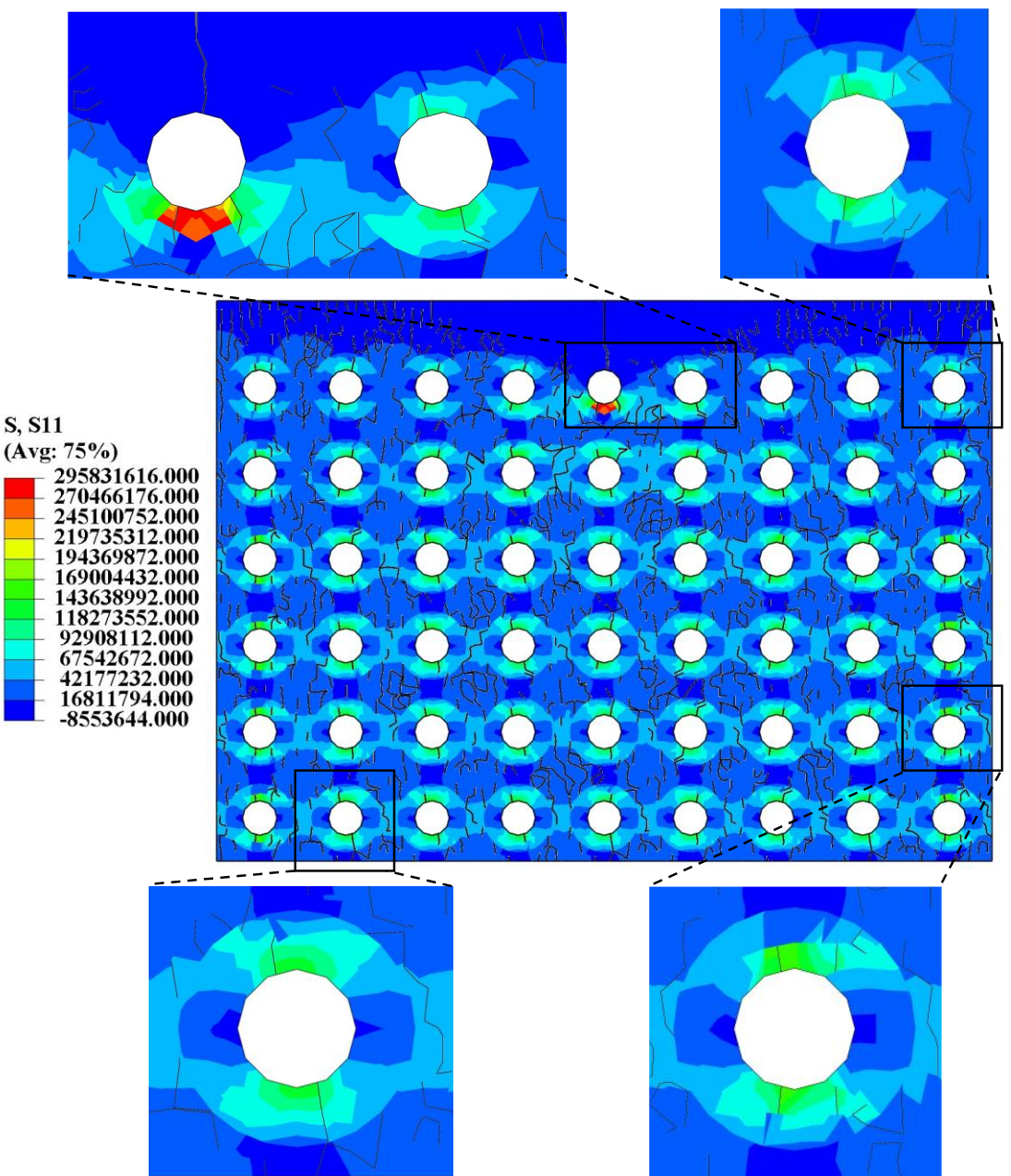


Fig. 12 The 1-directional stress distribution, when the fracture initiate on dentin, in which the zoomed view shows the how cracks evolved around the DT, with elastic ITD.

In Fig. 13, the crack is fully propagated on the dentin, in which we observe more evenly distributed 1-directional stress and mildly higher stress value on the PTD along the 2-direction. Also, some cracks perpendicular to the loading directions on the PTD propagated on the ITD and connected with the mentioned wavy cracks that may be related to the debonding. Such indicates how cracks on ITD is propagated from cracks originated from DT on the PTD. Notably, the DT neighboring the initial crack generates more crack in the lower part compared with the step of fracture initiation.

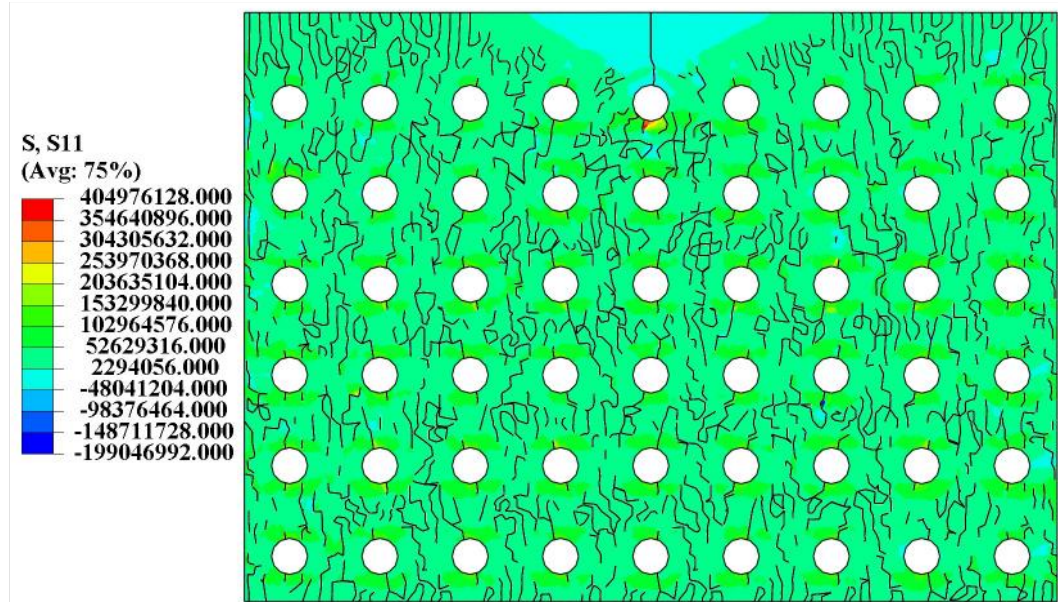


Fig. 13 The 1-directional stress distribution of the final stage of the fracture on dentin's microstructure, with elastic ITD.

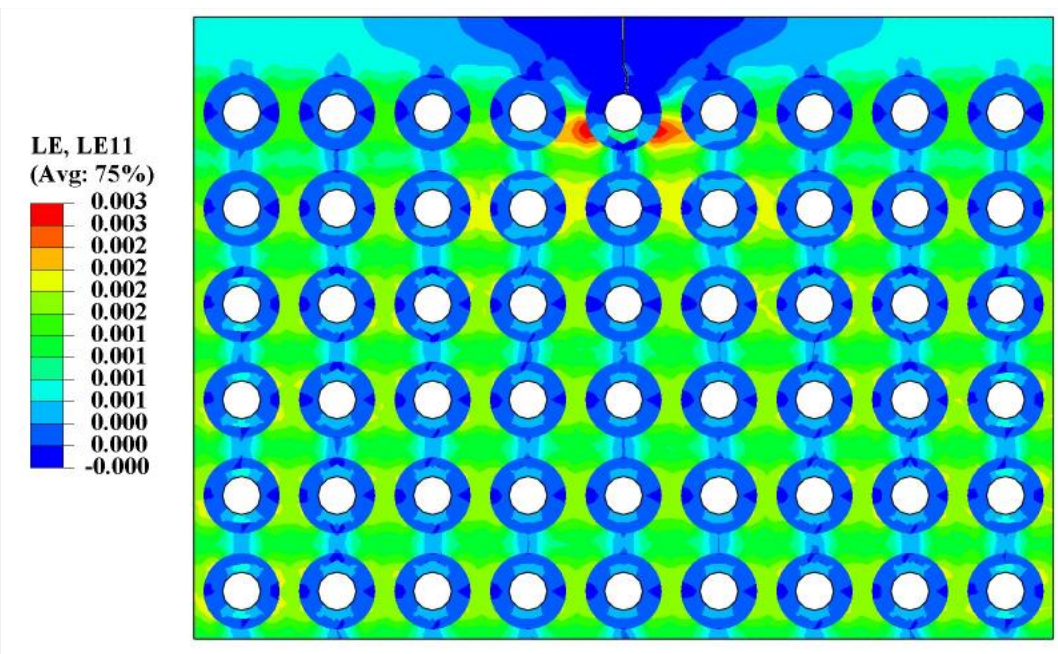


Fig. 14 The 1-directional strain distribution of preliminary stage of the crack propagation on dentin structure, with elastic ITD.

In Fig. 14, we observe a larger value of 1-directional strain on the ITD comparing with PTD due to the smaller elastic modulus. There are also strain concentrations along with the DT neighboring the initial crack. Notably, a severe 1-directional strain concentration on the ITD bonding the DT neighboring the initial crack can be detected. Also, we observe a larger strain value in 2-direction on PTD surrounding the DT. Correspondingly, a smaller strain value in 2-direction on ITD. In detail, there are 1-directional strain concentration occurs around the DT neighboring the initial crack

for a value of about 0.002. Such patterns are also discerned in the lower part occurs on ITD bonding the PTD, such strain indicates the possibility of the debonding.

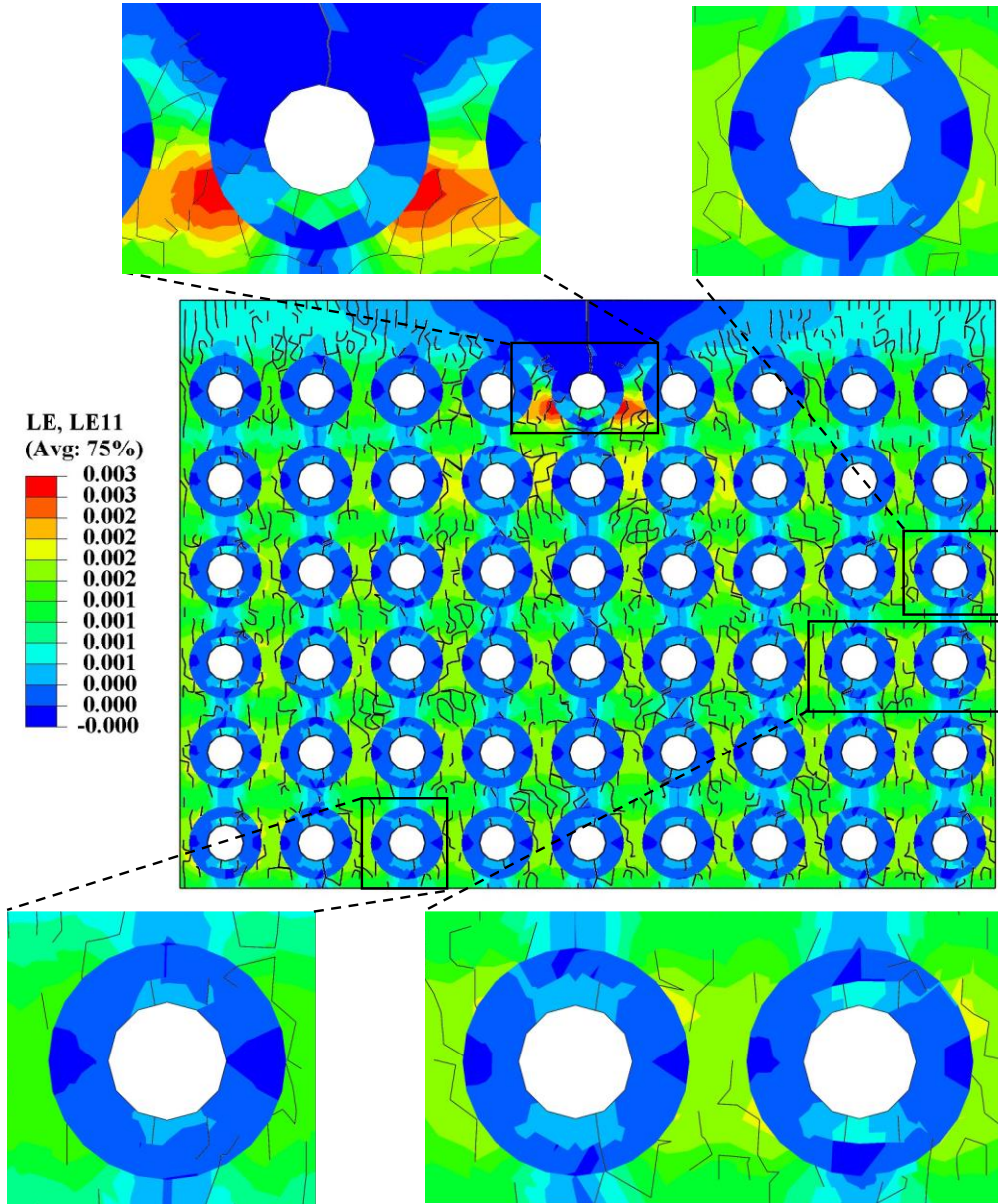


Fig. 15 The 1-directional strain distribution, when the fracture initiate on dentin, in which the zoomed view shows the how crack evolved around the DT, with elastic ITD.

From the 1-directional strain distribution as the same step as in Fig. 12 shown in Fig. 15, we observe evident strain concentration on the ITD bonding the DT neighboring the initial crack. Such a phenomenon, corresponding to Fig. 12, as the stress concentration occurs on the PTD of the same DT, could reflect the stiffness difference of ITD and PTD. Notably, we observe cracks parallel to loading direction as shown in the right-top and right-down zoomed views. The cracks can be attributed to the inner

friction of the PTD under 1-directional loading. As shown in the left-top zoomed view, there is a “V-shaped” crack occurs on the PTD neighboring the initial crack, the “V-shape” could be explained as the synergy of the PTD inner friction and the propagation and the fracture energy dissipation of the initial crack.

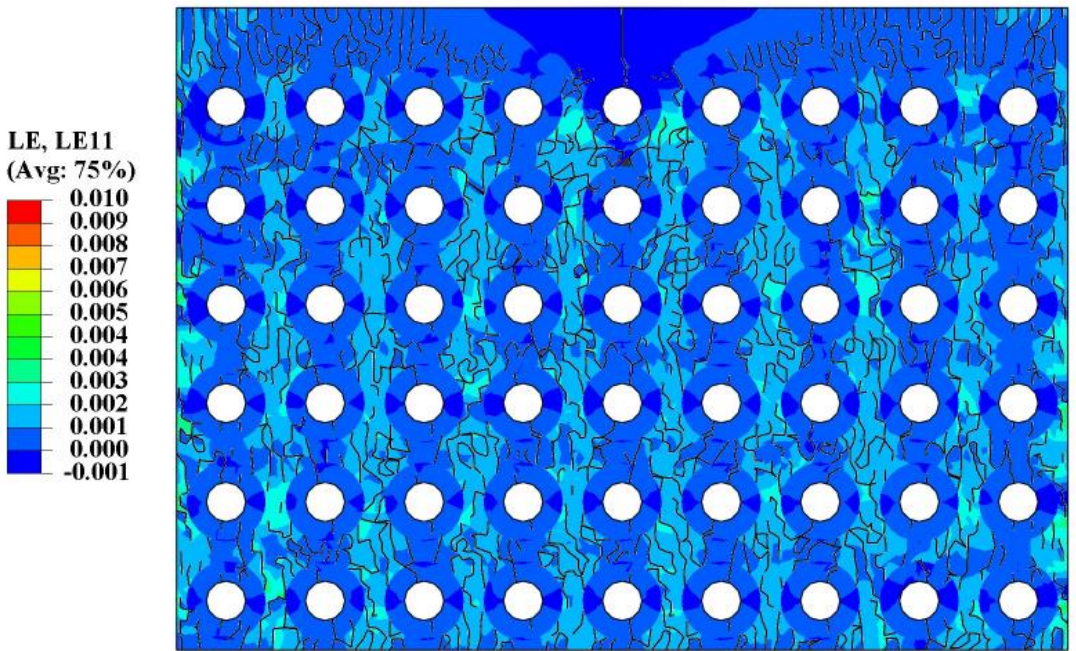


Fig. 16 The 1-directional strain distribution of the final stage of the fracture on dentin’s microstructure, with elastic ITD.

In the last step of the crack propagation as shown in Fig. 16, the 1-directional strain is more evenly distributed on the ITD with a higher value on the 2-direction. Such specific high value on the 2-direction could be attributed to the special shape of PTD and the elastic modulus difference: under 1-directional tensile loading, with a circular shape when the surrounding soft matrix is under tension the PTD perpendicular axis (2-direction) is under compression, hence dissipate energy in the 2-direction to its surrounding soft matrix, ITD. Hence the ITD is compressed within the two PTDs, indicating 2-directional strain value concentration.

3.2.2 Plastic ITD

With the adoption of the perfectly plastic model of ITD, we generate different results with the beyond. Detecting these differences might unveil the mechanism of the ITD plastic nature.

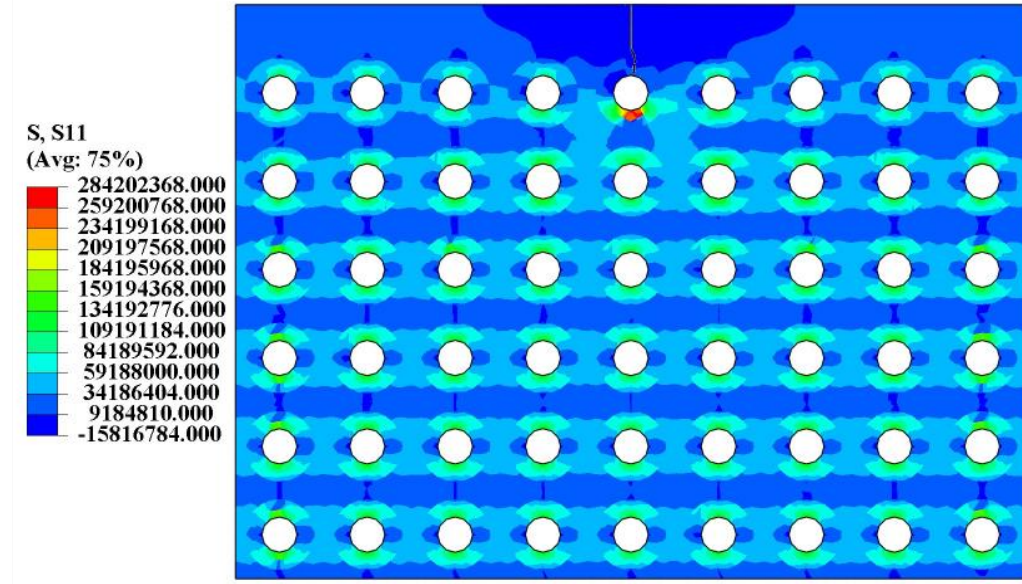


Fig. 17 The 1-directional stress distribution of preliminary stage of the crack propagation on dentin structure, with a perfectly plastic ITD, in first step.

In the preliminary stage, the stress distribution generally has no difference due to the plastic has not made much effect from Fig. 17. From Fig. 18 and Fig. 13 we detect similar crack propagation patterns, but fewer cracks in Fig. 18. Also, the structure displays a less 1-directional stress value shown in Fig. 18 with the plastic ITD. Such a phenomenon indicating the plasticity reduces the stress, and resist the crack growth comparing the 1-directional stress distribution.

Notably, a stress distribution difference occurs along the propagating of the initial crack comparing Fig. 18 with Fig. 13. The 1-directional stress distributed along the initial crack as a triangle area in Fig. 13, howbeit a stress decrease along the initial crack as given in Fig. 18. Such distributions also indicate how the plastic ITD could reduce the stress and resist the crack growth.

From Fig. 19 and Fig. 14 we observe conspicuous differences as the strain is comparably more concentrated along the 1-direction with the adoption of the plasticity. But the maximum strain value is lower for plastic ITD with 0.002 comparing with 0.003. Albeit the concentrated strain value along 1-direction is bigger than dentin with elastic ITD. The concentration in 1-direction at the beginning stage could be attributed to plasticity responding to tensile loading to resist fracture.

At the stage of the fracture initiation, a totally different 1-directional strain distribution displayed as given from Fig. 15 and Fig. 20. The elastic ITD model displays a higher maximum strain value. The general strain value variance between the ITD and

PTD is similar for the two models. Howbeit the plastic ITD model displays higher 1-directional strain value.

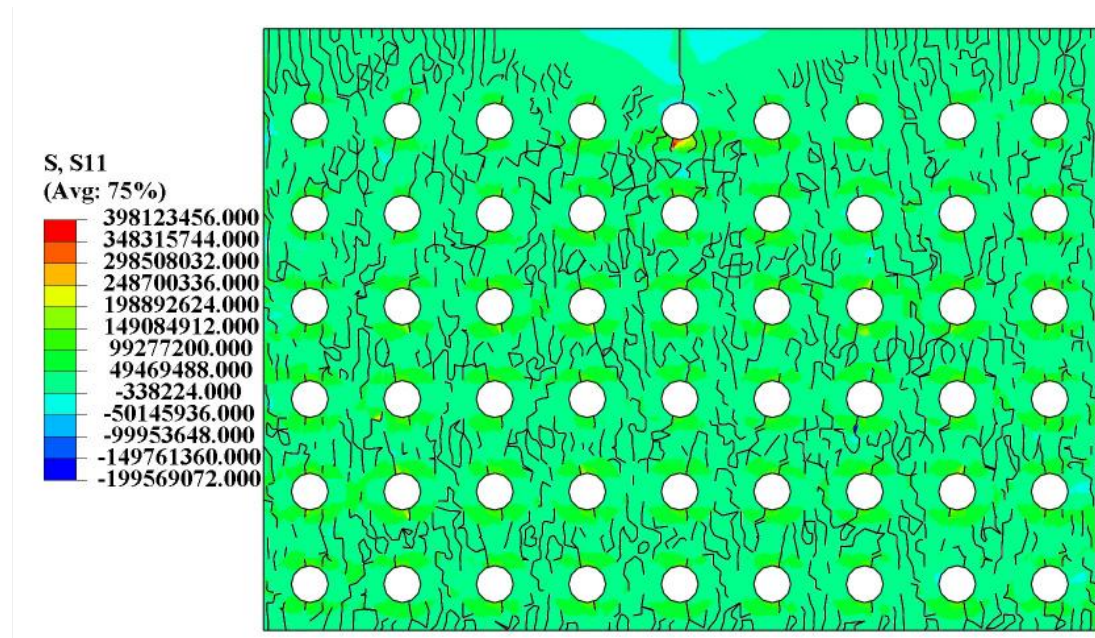


Fig. 18 The 1-directional stress distribution of the final stage of the fracture on dentin's microstructure, with a perfectly plastic ITD.

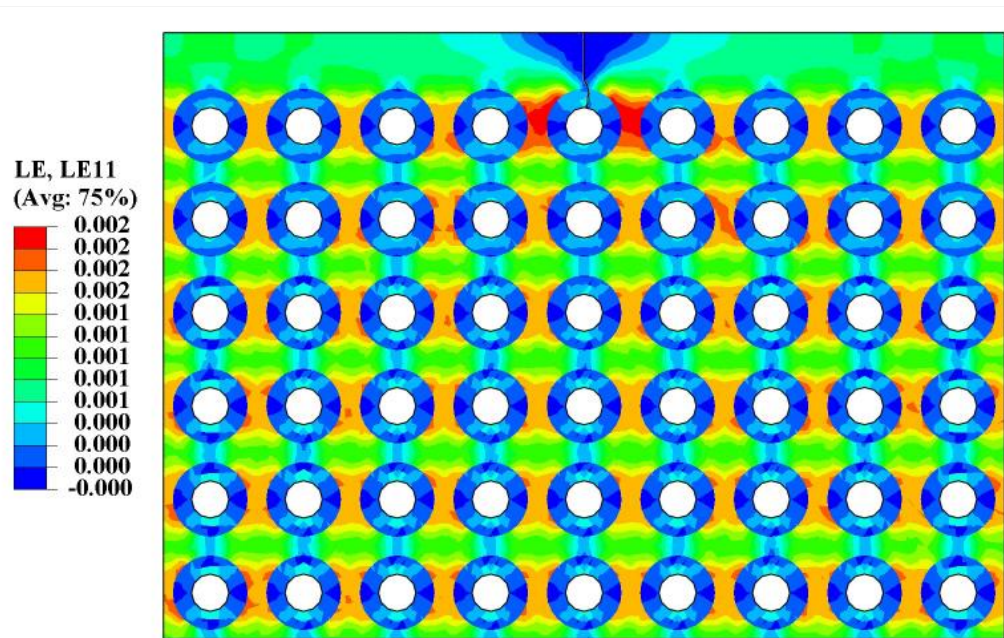


Fig. 19 The 1-directional strain distribution of preliminary stage of the crack propagation on dentin structure, with a perfectly plastic ITD.

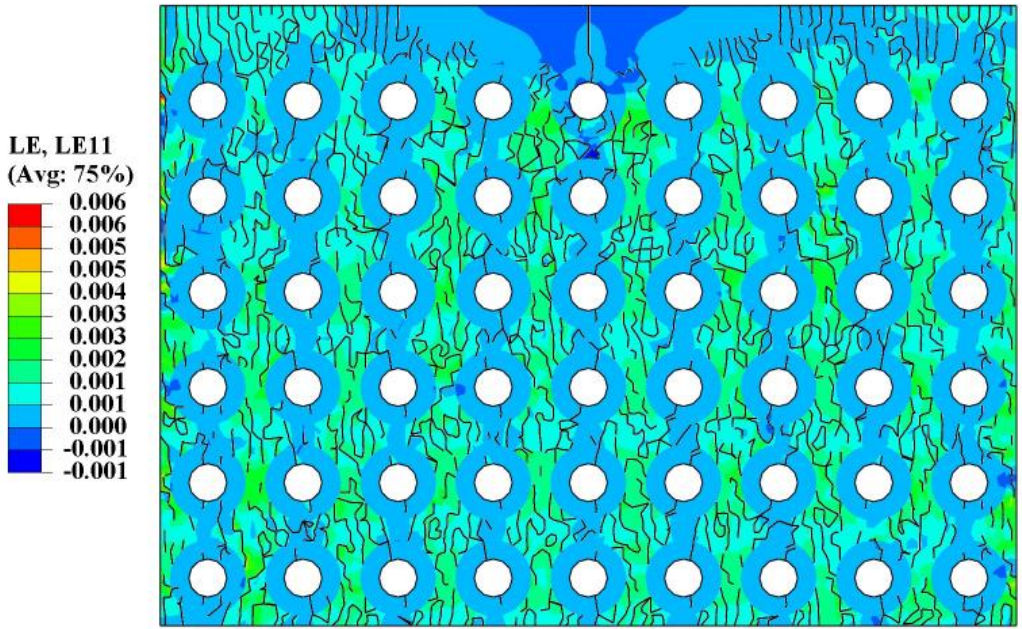


Fig. 20 The 1-directional strain distribution of the final stage of the fracture on dentin's microstructure, with a perfectly plastic ITD.

To specify the effect of the plastic nature from the ITD, we know present 1-directional plastic strain evolving from Fig. 21 to Fig. 22. The plastic strain does not exhibit a notable effect at the crack initiation stage in Fig. 21, with only small plastic strain, occurs on the ITD cracks bonding the PTD.

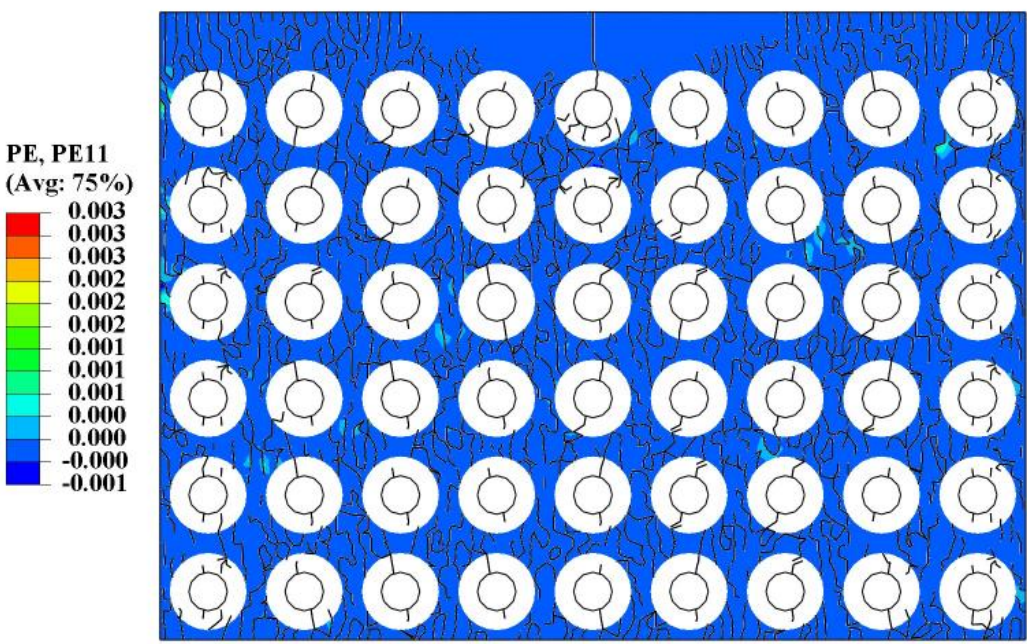


Fig. 21 The 1-directional plastic strain distribution, when the fracture initiate on dentin, with a perfectly plastic ITD.

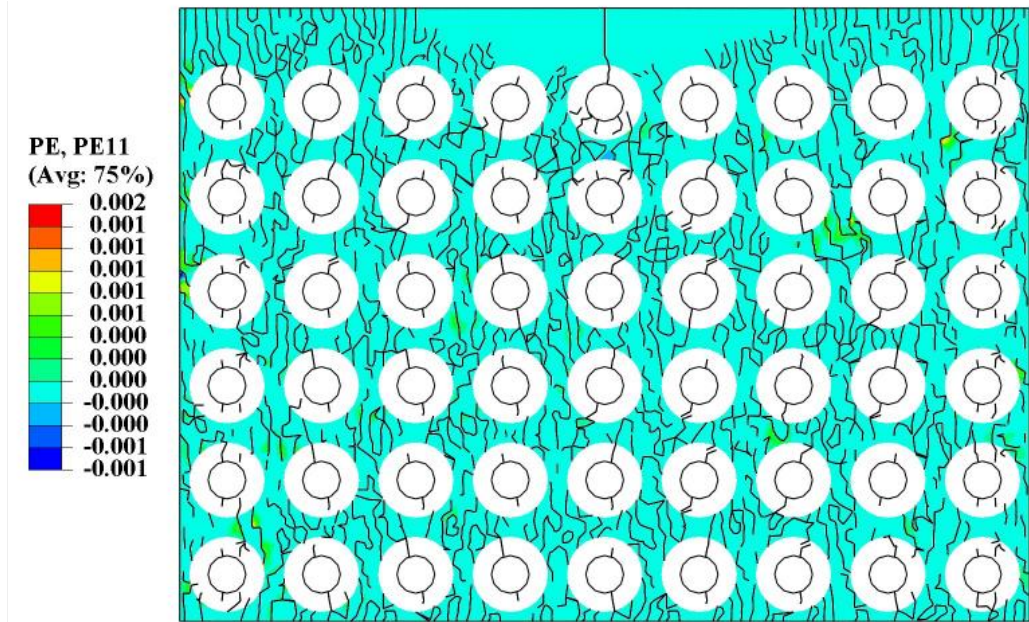


Fig. 22 The 1-directional plastic strain distribution of the final stage of the fracture on dentin's microstructure, with a perfectly plastic ITD.

As for the final stage of the crack propagation, the 1-directional plastic strain still does not display the conspicuous impact of the ITD. Yet the strains occur in several areas within the cracks for the value of approximately 0.001. As comparing and discussed previously, such plastic concentrate to resist crack and fracture. With specifically show the 1-directional plastic strain distribution, one deduces the plastic strain does not make much variance on the total strain value, however, the plastic nature helps reduces stress increases and concentration, henceforth, releases fracture energy to resist crack growth.

To quantitatively show how plasticity alters the stress-strain distribution, here, we present 1-directional stress-strain diagrams for both the PTD and ITD considering elastic and plastic ITDs as given from Fig. 23 to Fig. 24. During the fracture process, for the elastic PTD, with an elastic ITD, the PTD displays higher 1-directional values shown in Fig. 23, indicating the plastic ITD could reduce the 1-directional stress on the bonding PTD. Such results indicate the plastic nature of ITD can release stress and reduces chances for fracture on the PTD. In the zoomed view shown in Fig. 23, the 1-directional stress initially growing with the same trends growing with the slopes with an approximately higher stress value, then exhibits a higher slope with a higher stress.

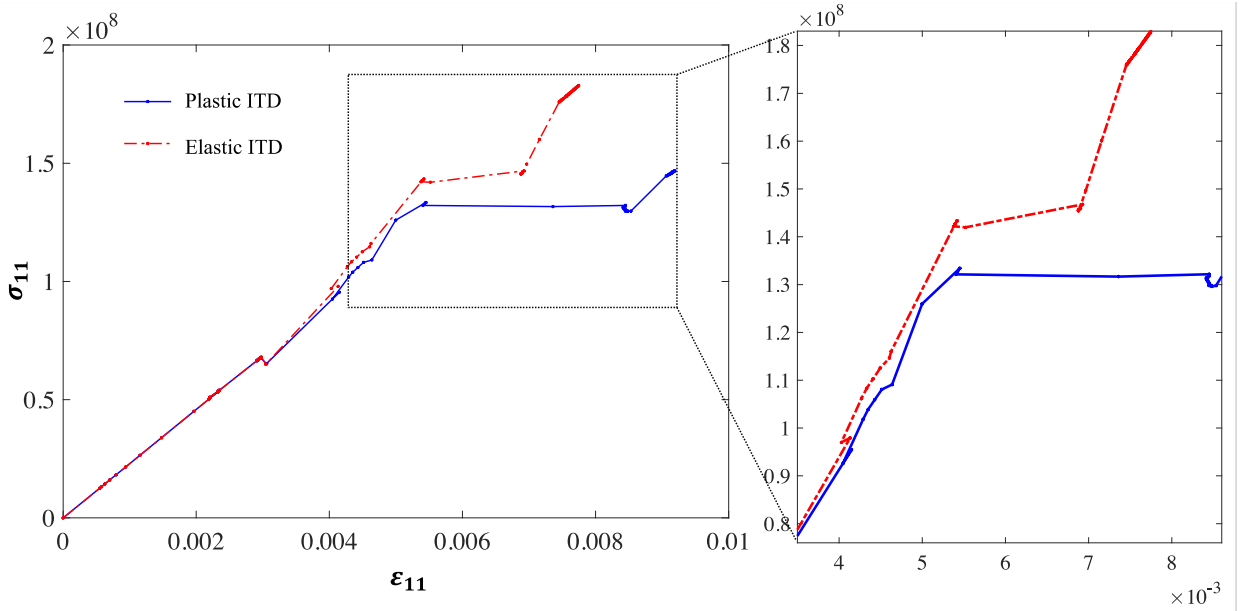


Fig. 23 The 1-direction stress-strain relationship of the PTD with the crack propagation, comparing elastic and perfectly plastic ITD, respectively.

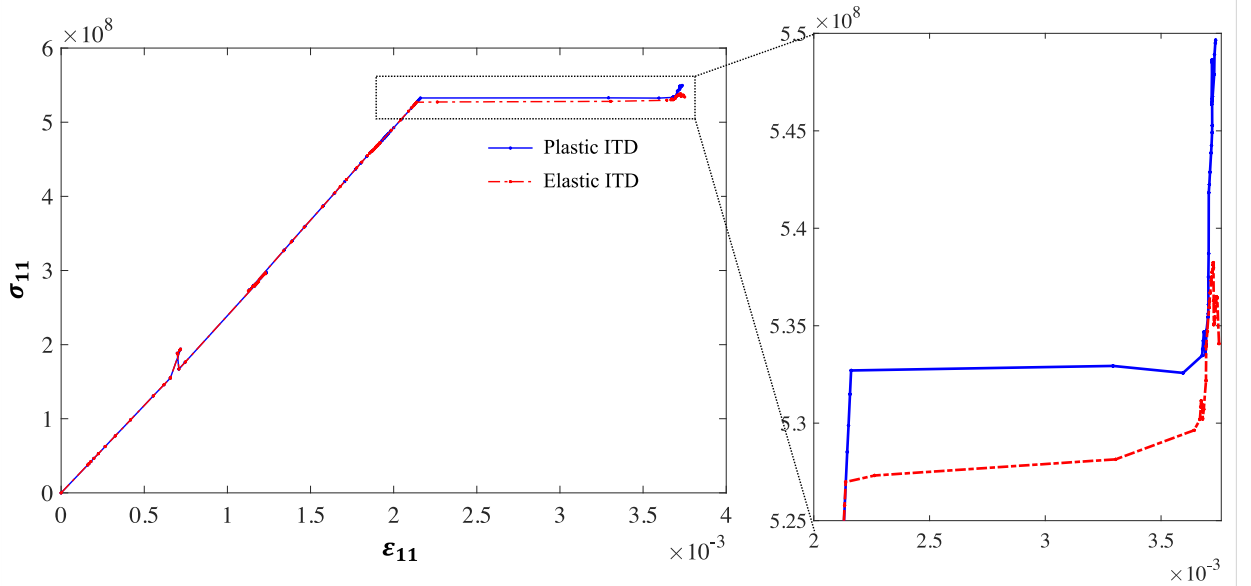


Fig. 24 The 1-direction stress-strain relationship of the ITD with the crack propagation, comparing elastic and perfectly plastic ITD, respectively.

Here in Fig. 24, the plastic nature does not variate the 1-directional stress as shown clear for PTD in Fig. 23. Only little variance can be detected after the initiation of the fracture as small 1-directional stress difference shown in the zoomed view in Fig. 24.

Comparing Fig. 23 and Fig. 24 we deduce that the plasticity of ITD will robustly affect the 1-directional stress distribution of its bonding PTDs, howbeit will not alter such distribution for ITD. Hence, we can reason out the protection mechanism of the

ITD plasticity: to reduce the tensile stress on the PTD to avoid PTD crack as mentioned in the preceding chapter, thence the crack is less likely to propagate along the PTD to ITD to cause further fracture and failure.

As mentioned in the §0, the debonding of the ITD and PTD is caused by the elastic modulus mismatch of the two materials, which occurs along the bonding interface. In our approaches, no clear debonding phenomena observed howbeit similar fracture observed as in the zoomed view in Fig. 12 and Fig. 15. Hence, the debonding can be investigated based on our model through studying the shear stresses on the bonding interface between the ITD and PTD.

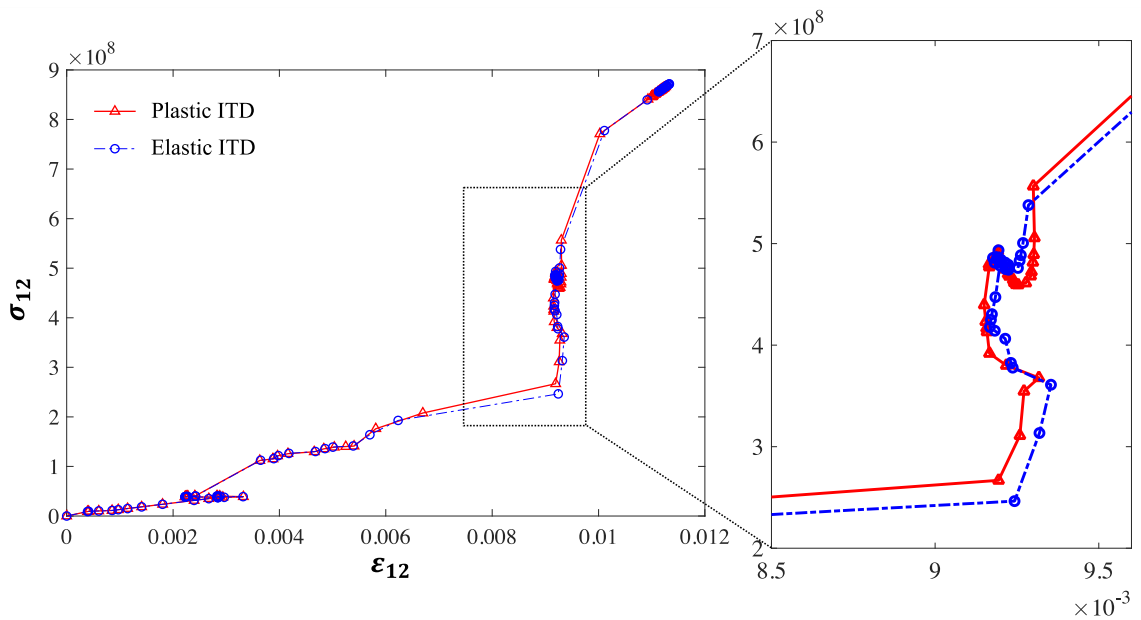


Fig. 25 The shearing stress-strain relationship of the bonding interface with the crack propagation, comparing elastic and perfectly plastic ITD, respectively.

Here, in Fig. 25, the shear stress-strain on the ITD and PTD bonding interface is given. From the distribution of the diagram, there is no clear variance with the effect of the ITD plasticity. With the scrutiny of the two curves, the zoomed view displays small variance with the two stresses, in which the plastic ITD bonding shearing stress was initially larger but later smaller than the elastic ITD's, and later on bigger than the elastic ITD. The competing stresses as shown on the bonding interface within the plastic and elastic ITD clue in that plasticity does not alter shearing between boundaries or frictional failure for our model. Also, the competing stresses indicate how elastic and plastic ITD show different bonding friction behavior at different phase with a generally similar trend.

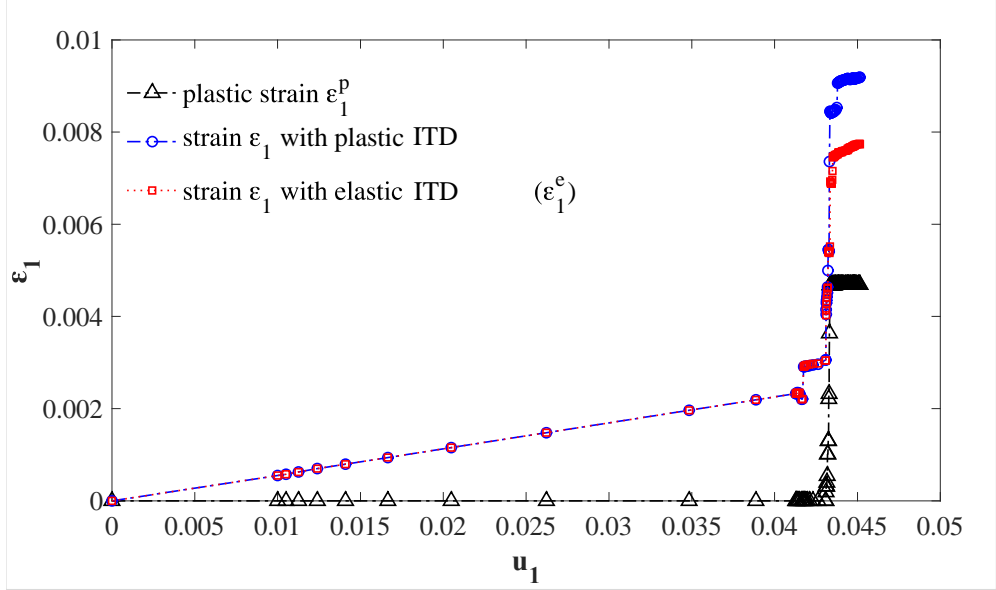


Fig. 26 The 1-directional strain evolution with the growing 1-directional displacements, in which the plastic strain, total strain of the elastic and perfectly elastic ITD is presented respectively.

As shown in Fig. 14 to Fig. 16 and Fig. 19 to Fig. 22, aside from previous discussions, Fig. 26 quantitatively presents how plasticity affects the 1-directional strain distribution in the fracture process. The curves comparing structure with the 1-directional strain of the plastic ITD, elastic ITD, and the plastic strain presents how strain evolves in the fracture process. Both the 1-direction strain for elastic and plastic ITD experience a ladder-shaped increase as the 1-directional displacement in the value of about 0.042. Subsequently, the plastic strain makes an effect at the displacement value of about 0.043. The ladder-shaped strain increase indicates the fracture occurs on dentin. With the effect of the ITD plastic strain, the dentin structure experience overall higher strain value as to resist crack. Observing the details, there is a smaller ladder-shaped increase for the dentin strain with plastic ITD. Such ladder-shaped increasing of the strain could also attribute to the protection mechanism of the plasticity as to resist crack growth.

Conclusion

Investigating the stiffness and toughness of the dentin structure, we first model the geometry based on the dentin microstructure from SEM photos (Fig. 1, Fig. 2). The study of the composite's elastic modulus based on Eq. 2 to Eq. 4 with the boundary conditions of tensile loading with fixed displacement in 1-direction as shown in Fig. 3 and depicted in Eq. 1. Considering the elasticity and plasticity (Eq. 5 to Eq. 7) of ITD respectively regarding parameters of Tab. 2. The fracture of the structure is

based on adopted ductile damage evolution model with failure criterion of maximum principal stress (Eq. 9 to Eq. 14) with specific parameters (Tab. 3 to Tab. 6) and boundary conditions of fixed on the down edge under tensile loading with an initial crack (Fig. 4 and Eq. 15).

We obtain results of the dentin composite's elastic modulus 1765574656 Pa. The 2-directional stress distribution shows there are stress concentrations along the axis perpendicular to the loading directions on PTD (Fig. 6). The 2-directional strain also exhibits similar behavior (Fig. 5). With ITD plasticity, the 2-directional strain is more heavily concentrated on the four corners bonding the PTD on ITD (Fig. 7). Such phenomenon is delineated through observing the 2-directional plastic strain distribution, showing the plastic strain initiated on the four corners nearing the central axis, from which we could deduce the strain concentrations on corners are ITD plastic effect (Fig. 8). The 2-directional stresses exhibit lower values with more an evenly distributed pattern (Fig. 9). The 2-directional reaction forces visualize how ITD plasticity influences the overall stiffness through forces reduction (Fig. 10).

For the fracture growth evolution, we observe two types of cracks: crack growing along the axis perpendicular to the loading direction on PTD and wavy cracks surrounding the PTD on ITD as in the zoomed views (Fig. 12 and Fig. 15). We also detected V-shaped cracks (Fig. 15) that can be attributed to the synergy of the PTD inner friction and crack propagation along the axis perpendicular to the loading direction. With the plasticity of ITD, the structure exhibits lower 1-directional stress values (Fig. 13 and Fig. 18) yet small variance for the 1-directional strain (Fig. 16 and Fig. 20). To investigate the plasticity specifically, the 1-directional plastic strain shows little concentration on ITD with a value of approximately 0.001 (Fig. 21 to Fig. 22). Such a result indicates the plastic strain does not variate strain value evidently, while reduces the stress value to resist crack growth (Fig. 18 and Fig. 13).

Based on the 1-directional stress-strain distribution for both the ITD and the PTD, The ITD plasticity reducing the PTD with elastic ITD for 2-directional stress evidently in Fig. 23. Howbeit the ITD plasticity slightly increases the ITD 2-directional stress value (Fig. 24 and Fig. 25). Such results unveiled the protection mechanism of ITD plasticity: to slightly increase the ITD stress to absorb the fracture energy dissipated from the PTD as the PTD stress is reduced. There is no shearing stress value variance on the bonding interface, indicating plasticity does not contribute to such fracture phenomenon (Fig. 25). The strain distributions indicate plasticity occurs after the initiation of fracture to resist further failure (Fig. 26).

Acknowledgement

The author would like to thank B. An for the valuable discussion.

References

- [1] D. Arola, S. Gao, H. Zhang, R. Masri. The Tooth: Its Structure and Properties. *Dental Clinics of North America*. Volume 61, Issue 4, October 2017, Pages 651-668.
- [2] Marshall GW Jr. Dentin: microstructure and characterization. *Quintessence Int.* 1993; 24(9):606-617.
- [3] Jacob Lubliner [1990]. PLASTICITY THEORY.
- [4] Z. Suo. Perfect Plasticity. *Plasticity*. imechanica.org.
- [5] Jinyuan Zhai. MODELING DUCTILE DAMAGE OF METALLIC MATERIALS. PhD Dissertation. University of Akron. August, 2016.
- [6] J. Ruzicka, M. Spaniel, A. Prantl, J. Dzugan, J. Kuzelka, M. Moravec. Identification of Ductile Damage Parameters in the Abaqus. March 2013.
- [7] D. Arola, J. A. Rouland, D. Zhang. Fatigue and fracture of bovine dentin. *Experimental Mechanics* volume 42, pages380–388(2002)
- [8] J. Ivanci, M. Naranjo, S. Correa, A. Ossa, F.R. Tay, D.H. Pashley, D. Arola. Differences in the microstructure and fatigue properties of dentine between residents of North and South America. *archives of oral biology* 59 (2014) 1001–1012
- [9] Zhang, Y., Du, W., Zhou, X. et al. Review of research on the mechanical properties of the human tooth. *Int J Oral Sci* 6, 61–69 (2014).
- [10] M. Toparli, N.S. Koksal, Hardness and yield strength of dentin from simulated nano-indentation tests, *Computer Methods and Programs in Biomedicine*, Volume 77, Issue 3, 2005, Pages 253-257, ISSN 0169-2607
- [11] Amaury Namour et al. Treatment of Dentinal Hypersensitivity by means of Nd:YAP Laser: A Preliminary In Vitro Study. *The Scientific World Journal*. Volume 2014, Article ID 323604, 7 pages

- [12] A. Nazari, D. Bajaj, D. Zhang, E. Romberg, D. Arola. Aging and the reduction in fracture toughness of human dentin. *JOURNAL OF THE MECHANICAL BEHAVIOR OF BIOMEDICAL MATERIALS* 2 (2009) 550–559.
- [13] B. An, H. D. Wagner. Role of microstructure on fracture of dentin. *Journal of the Mechanical Behavior of Biomedical Materials*. Vol 59 (2016): 527-537. ISSN 1751-6161.
- [14] An B. Constitutive modeling the plastic deformation of bone-like materials. *Int J of Solids Struct* 2016; Vol 92–93: 1-8
- [15] An B., Zhang D. Bioinspired toughening mechanism: lesson from dentin. *Bioinspir. Biomim.*, 10 (2015), Article 046010
- [16] B. An, D. Zhang. An analysis of crack growth in dentin at the microstructural scale. *Journal of the Mechanical Behavior of Biomedical Materials* 81 (2018) 149–160.
- [17] B. An, Y. Xu, D. Zhang. Crack initiation and propagation in composite micro-structure of dentin. *International Journal of Solids and Structures* 110–111 (2017) 36–43
- [18] H. Teng. Effective elastic–plastic response of two-phase composite materials of aligned spheroids under uniaxial loading. *Mechanics of Materials* 117 (2018) 91–104.
- [19] M. Majewski, P. Holobut, M. Kursa, K. Kowalczyk-Gajewska. Packing and size effects in elastic-plastic particulate composites: Micromechanical modelling and numerical verification. *International Journal of Engineering Science* 151 (2020) 103271
- [20] C. He, J. Ge, B. Zhang, J. Gao, S. Zhong, W. K. Liu, D. Fang. A hierarchical multiscale model for the elastic-plastic damage behavior of 3D braided composites at high temperature. *Composites Science and Technology* 196 (2020) 108230

SECTION V

Investigation of the mechanics of the airfoil: application of machine learning in the noise prediction of NACA 0012

Abstract

NACA 0012 is a typical airfoil widely applied for studies of fluid mechanics. The fluid stream on airfoil creates noise. The mechanism of airfoil noise is complicated. The concentration of the study is to investigate the noise of NACA 0012 based on the experimental database. The NACA airfoil is introduced in which related parameters and designation are shown as figures. The mechanism of airfoil encounters a free stream flow is given and introduced. Plus, based on simulation and obtained data, the mechanical distribution of the airfoil is presented in both the form of diagrams and simulation results. The attributes of the applied database are presented, where the data attributes are represented as figures. The mathematical basis of the decision tree and a linear regression model is demonstrated through equations. Hence, the calculation results of the decision tree and linear regression model is presented as the form of figures and formulas. Here, I applied a set of data trained for the model to verify the validity of both the decision tree and regression model. Simultaneously, a set of tested data is used in both the models to get the predicted noise of airfoil NACA 0012.

Keywords: computational fluid dynamics; machine learning; finite element method; airfoils; NACA0012

Introduction

The application and study of airfoil started in the 20th century, in which the NACA airfoil, a collection and parameters' algorithm of airfoil created by NASA, is widely applied and studied by scholars. Computational fluid dynamics is also widely used in the study of airfoils, especially in determining the mechanical distribution and analytical refinement of airfoil design [2]. The dynamic motion and vortex distribution are also taken into consideration [3]. Similar works were then, coupled with wind tunnel test to investigate the wing-body effect [4]. The numerical study also investigates its ground effect focusing on the wing vortex [5]. The wing's noise effect and pollutant emission's effect is then be reviewed and discussed [6]. Most importantly, the morphology and its mechanical effect of NACA 0012 airfoil are discussed, which elucidate the important mechanism of airfoil's geometrical parameters on mechanics [7]. The material designation, which includes material and structural arrangement, contributes largely to the reduction of noise [8], which are discussed in this article. The computational mechanical coefficients (Lift, Drag, Moment) is calculated by investigating various parameters in the CFD process [9]. Taken the 3D wing as a whole, the algorithm for computational simulation methods is discussed and applied to different wing shape [10]. For what is more, certain optimization based on mechanical coefficients calculation is presented [11]. The complex essence of airfoil design is elucidated in detail considering fluid mechanics [12]. The detailed investigation of the CFD application on NACA 0012 is proposed in a methodology to harvest the benefits of camber morphing airfoils for small unmanned aerial vehicle (SUAV) applications [13]. The fluid fields and mechanical coefficients are studied by inspecting the angle of attack ([14], [15]). The vibration and noise are generally mostly caused by the vortex. Airframe noise of engine vortex is studied by carrying out extensively noise control tests, which presents a few design concepts on the landing gear, high-lift devices, and whole aircraft are provided for advanced aircraft low-noise design [16]. Such vortex is also studied with regards to Reynold's number [17].

Taken consideration of the airfoil's noise, complex characters synergized the production of fluid noise, which is still in studying by scholars. Albeit the exact equation depicting the cause of noise does not exist, a significant amount of methods can be applied for noise prediction, including model describing the running of the engine [18]. Therefore, noise reduction potentials are thence be demonstrated through numerical method [19]. Experimental methods for noise detection is also presented with re-

sults of different noise reduction approaches [20]. Specific wing design could also reduce noise [21]. In fine, noise is very complicated and yet has no exact methods for the study.

Notwithstanding, machine learning is born to solve complicated, knotty problems. Based on the database applied from experiments of airfoil NACA 0012 containing noise and related attributes' data [1], Brooks *et al.* [22] presents predictions of the airfoil noise based on previous data and methodologies. Then, a neural network study for noise prediction is presented ([23], [24]).

Method

NACA 0012

The NACA airfoils are airfoil shapes for aircraft wings developed by the National Advisory Committee for Aeronautics (NACA). The parameters in the numerical code can be entered into equations to precisely generate the cross-section of the airfoil and calculate its properties. [25]

The schematic view of airfoil NACA 0012 is shown as in Figure 1, in which the geometrical parameters is obtained from *Airfoil-Tools* [26].

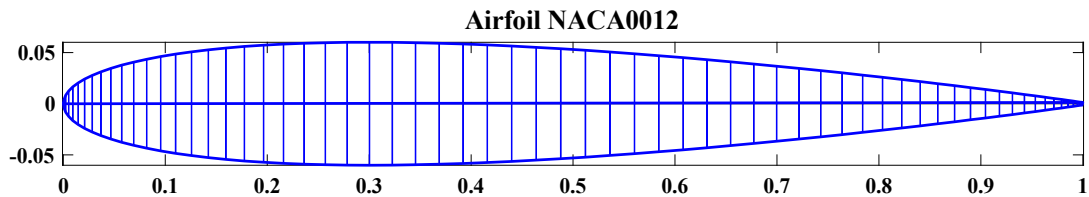
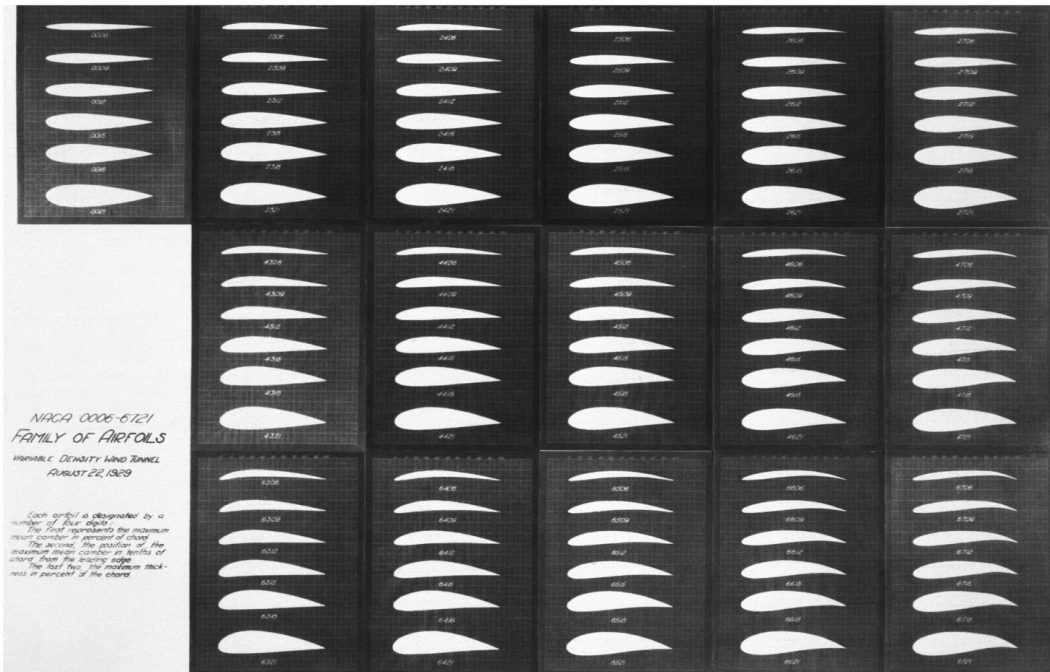


Fig. 1 Schematic illustration of airfoil [NACA0012] morphology.

When encountered with free stream flow, the airfoil will experience lift and drag force, which magnitude is determined by velocity (v), angle of attack (α), etc. as shown in Figure 3. Such mechanical distribution will hence be analyzed through simulation and decent diagrams.

Plus, on account of the air friction, boundary layer detachment, vibration, etc. the airfoil will generate noise of different magnitudes. The mechanisms of such noise are complex. Thus, with the application of machine learning, we can discern certain mechanisms under the noise generation based on the airfoil experimental database.



NASA L-05344

Langley Research Center
Hampton, Virginia 23681-0001

Fig. 2 The collection of NACA airfoil [25].

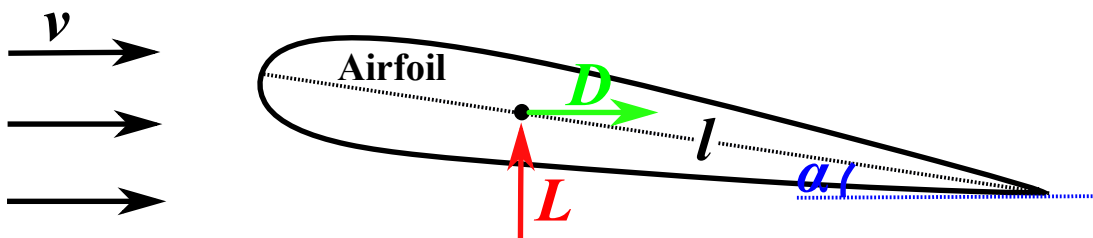


Fig. 3 Schematic view for the mechanical distribution on airfoil free stream velocity.

The attributes of the database are shown in Table 1, from which one could obtain that there are five attributes that are taken into consideration in the experiments: Frequency, Angle of Attack, ..., Suction side displacement thickness. The value of these attributes with their relation with Scaled sound pressure level is shown in Figure 4, where Scaled sound indicates the airfoil's noise.

Frequency [Hertz]	
Angle of attack [degrees]	
Chord length [meters]	1503 (data) X 5 (sets)
Free-stream velocity [meters/second]	
Suction side displacement thickness [meters]	
Scaled sound pressure level [decibels]	1503 (data)

Input Dataset **Output Dataset**

Tab. 1 The basic information and attributes of the airfoil dataset.

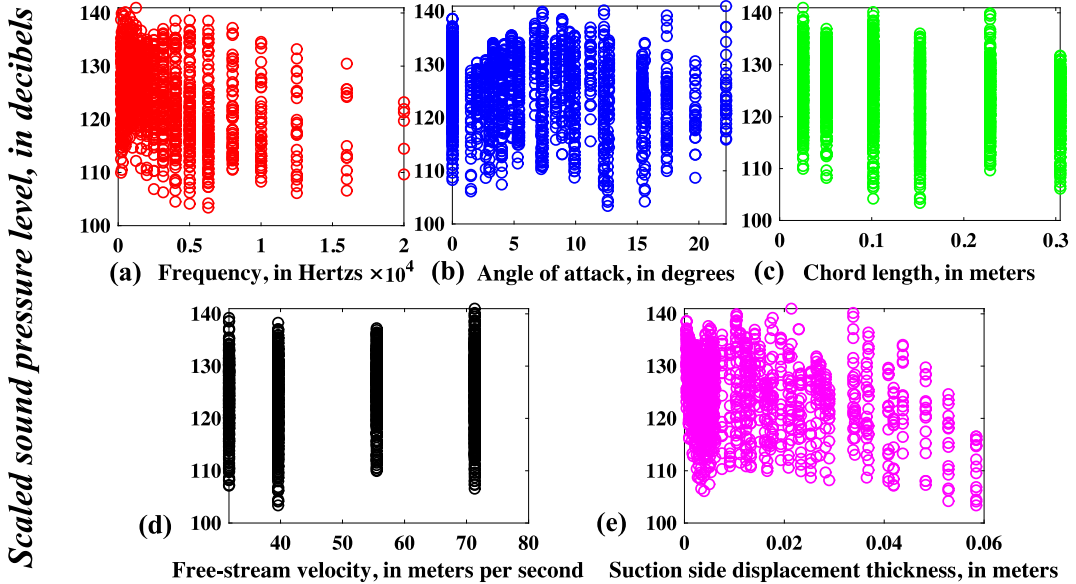


Fig. 4 The diagram of data attributes of the airfoil data. (a) Sound Pressure-Frequency diagram. (b) Sound Pressure-Attack Angle diagram. (c) Sound Pressure-Chord Length diagram. (d) Sound Pressure-Velocity diagram. (e) Sound Pressure-Displacement Thickness diagram.

Decision Tree

When estimating the purity of data sets, we often choose information entropy as a metric. First, let us first set D to represent the database, the proportion of the k^{th} sample in the data is $p_k(k=1,2, \dots, |y|)$, then the information entropy D can now be defined as

$$Ent(D) = - \sum_{k=1}^{|y|} p_k \log_2 p_k$$

In which the smaller the value of $Ent(D)$, the higher the purity of entropy D .

Now assume that the discrete attribute a has V possible values $\{a^1, a^2, \dots, a^V\}$, and now divide the sample set D for the general attribute a , then there will be V branch nodes (the v^{th} branch node contains D where the sample with the value a^v on the attribute a is denoted as D^v). based on the entropy definition, the number of different samples included in different branches can be considered where the branch node is given as $|D^v|/|D|$. then it can be inferred that the samples' numbers correlate with the branch node influence. Hence, the information gain of attribute a for sample D can be calculated:

$$Gain(D, a) = Ent(D) - \sum_{v=1}^V \frac{|D^v|}{|D|} Ent(D^v)$$

When selecting classification indices for the sample set, there are many classification methods. In this paper, Gini index are used for classification and calculation. First, the Gini index is applied to analyze the purity of the data set D :

$$Gini(D) = \sum_{k=1}^{|y|} \sum_{k' \neq k} p_k p_{k'}$$

Among which the $Gini(D)$ are randomly drawing two samples from the data set D , and their categories are respectively marked or represent different probabilities. Therefore, the smaller the calculated $Gini(D)$ value, the higher purity of the data set D , where the attribute a Gini index is defined as

$$Gini_index(D, a) = \sum_{v=1}^V \frac{|D^v|}{|D|} Gini(D^v)$$

In the paper, to simplify the calculation process, I deviate the scaled sound pressure in to two values, 0 and 1, which is distinguished by the mean value of sound

pressure. According to the attributes in Table 1, the equation of the decision tree calculation is shown in Equation 5.

$$\left\{ \begin{array}{l} Gini_index(D, Frequency) = \frac{value_1(v)}{1503} \left\{ 2 \cdot \frac{value_{1(noise_1)}}{value_1} \cdot \left(1 - \frac{value_{1(noise_1)}}{value_1} \right) \right\} \\ + \frac{value_2}{1053} \left\{ 2 \cdot \frac{value_{2(noise_1)}}{value_2} \cdot \left(1 - \frac{value_{2(noise_1)}}{value_2} \right) \right\} + \dots + \frac{value_n}{1503} \left\{ 2 \cdot \frac{value_{n(noise_1)}}{value_n} \cdot \left(1 - \frac{value_{n_1}}{value_n} \right) \right\} \\ Gini_index(D, Angle of attack) = \frac{v_1(angle of attack)}{1503} \left\{ 2 \cdot \frac{v_1(n-1)(\alpha)}{v_1(\alpha)} \cdot \left(1 - \frac{v_1(n-1)}{v_1} \right) \right\} + \dots \\ Gini_index(D, Chord length) = \frac{v_1(l)}{1503} \left\{ 2 \cdot \frac{v_1(n-1)(l)}{v_1} \cdot \left(1 - \frac{v_1(n-1)}{v_1} \right) \right\} + \dots \\ Gini_index(D, Free stream velocity) = \frac{v_1(v)}{1503} \left\{ 2 \cdot \frac{v_1(n-1)(v)}{v_1} \cdot \left(1 - \frac{v_1(n-1)(v)}{v_1} \right) \right\} + \dots \\ Gini_index(D, Suction side displacement thickness) = \frac{v_1(\delta)}{1503} \left\{ 2 \cdot \frac{v_1(n-1)(\delta)}{v_1} \cdot \left(1 - \frac{v_1(n-1)(\delta)}{v_1} \right) \right\} + \dots \end{array} \right.$$

Linear Regression

Initially, for a dataset with d attributes (independent variables), where we express as $\mathbf{x} = (x_1; x_2; \dots; x_d)$. Where x_i is the value of x in the i^{th} attribute. Hence, a linear model for function can be predicted by building a linear model

$$f(\mathbf{x}) = \omega_1 x_1 + \omega_2 x_2 + \dots + \omega_d x_d + b$$

For the multiple linear regression problem of the data set D with d attributes, we use the general vector form to express

$$f(\mathbf{x}) = \boldsymbol{\omega}^T \mathbf{x}_i + b, \text{ where } f(\mathbf{x}_i) \cong y_i$$

Subsequently, we can use the least square method to estimate $\boldsymbol{\omega}$ and b . For convenience, the vector form $\hat{\boldsymbol{\omega}} = (\boldsymbol{\omega}; b)$ is introduced. Therefore, the dataset D can be represented as a matrix \mathbf{X} of size $m \times (d + 1)$, where each row corresponds to an example, and the top d elements of the row correspond to d attribute values in the instance, the element value in the last row is always 1.

$$\mathbf{X} = \begin{pmatrix} x_{11} & x_{12} & \dots & x_{1d} & 1 \\ x_{21} & x_{22} & \dots & x_{2d} & 1 \\ \dots & \dots & \dots & \dots & \dots \\ x_{m1} & x_{m2} & \dots & x_{md} & 1 \end{pmatrix} = \begin{pmatrix} \mathbf{x}_1^T & 1 \\ \mathbf{x}_2^T & 1 \\ \dots & \dots \\ \mathbf{x}_m^T & 1 \end{pmatrix}$$

in which the attribute \mathbf{y} takes the form

$$\mathbf{y} = (y_1; y_2; \dots; y_m)$$

We set the vector $\hat{\boldsymbol{\omega}}^*$ as given:

$$\hat{\boldsymbol{\omega}}^* = \underset{\hat{\boldsymbol{\omega}}}{\operatorname{argmin}} (\mathbf{y} - \mathbf{X}\hat{\boldsymbol{\omega}})^T(\mathbf{y} - \mathbf{X}\hat{\boldsymbol{\omega}})$$

Now we set $E_{\hat{\boldsymbol{\omega}}} = (\mathbf{y} - \mathbf{X}\hat{\boldsymbol{\omega}})^T(\mathbf{y} - \mathbf{X}\hat{\boldsymbol{\omega}})$, by derivation of $\hat{\boldsymbol{\omega}}$ one get:

$$\frac{\partial E_{\hat{\boldsymbol{\omega}}}}{\partial \hat{\boldsymbol{\omega}}} = 2\mathbf{X}^T(\mathbf{X}\hat{\boldsymbol{\omega}} - \mathbf{y})$$

Let the value of Equation 11 be zero, one get the optimal solution of $\hat{\boldsymbol{\omega}}$. When $\mathbf{X}^T\mathbf{X}$ is a full rank matrix and a positive definite matrix, let $\frac{\partial E_{\hat{\boldsymbol{\omega}}}}{\partial \hat{\boldsymbol{\omega}}}$ be zero one get:

$$\hat{\boldsymbol{\omega}}^* = (\mathbf{X}^T\mathbf{X})^{-1}\mathbf{X}^T\mathbf{y}$$

where $(\mathbf{X}^T\mathbf{X})^{-1}$ be the inverse matrix of $\mathbf{X}^T\mathbf{X}$. Let $\hat{\mathbf{x}}_i = (\mathbf{x}_i; 1)$, hence eventually one get the linear regression model:

$$f(\hat{\mathbf{x}}_i) = \hat{\mathbf{x}}_i^T(\mathbf{X}^T\mathbf{X})^{-1}\mathbf{X}^T\mathbf{y}$$

For the estimated dataset specifically, the \mathbf{X} matrix is given considering the five attributes of the dataset:

$\mathbf{X}_{variables}$

$$= \begin{pmatrix} Frequency & Attack Angle & Chord length & Free velocity & Suction displacement \\ value_{v1} & value_{\alpha 1} & value_{l1} & values_{v1} & value_{\delta 1} \\ \dots & \dots & \dots & \dots & \dots \\ value_{v1503} & value_{\alpha 1503} & value_{l1503} & values_{v1503} & value_{\delta 1503} \end{pmatrix}$$

Similarly, the \mathbf{y} vector is given based on the dataset as:

$$\mathbf{y}_{Scaled sound pressure level} = (value_1; value_2; \dots; value_{1503})$$

Results

Mechanical Distribution

Based on the preceding introduction of airfoil's mechanical distribution, one could carry out a simulation of NACA 0012 in thence obtain its pressure and velocity distribution, which are shown in Figure 5 and Figure 6, respectively.

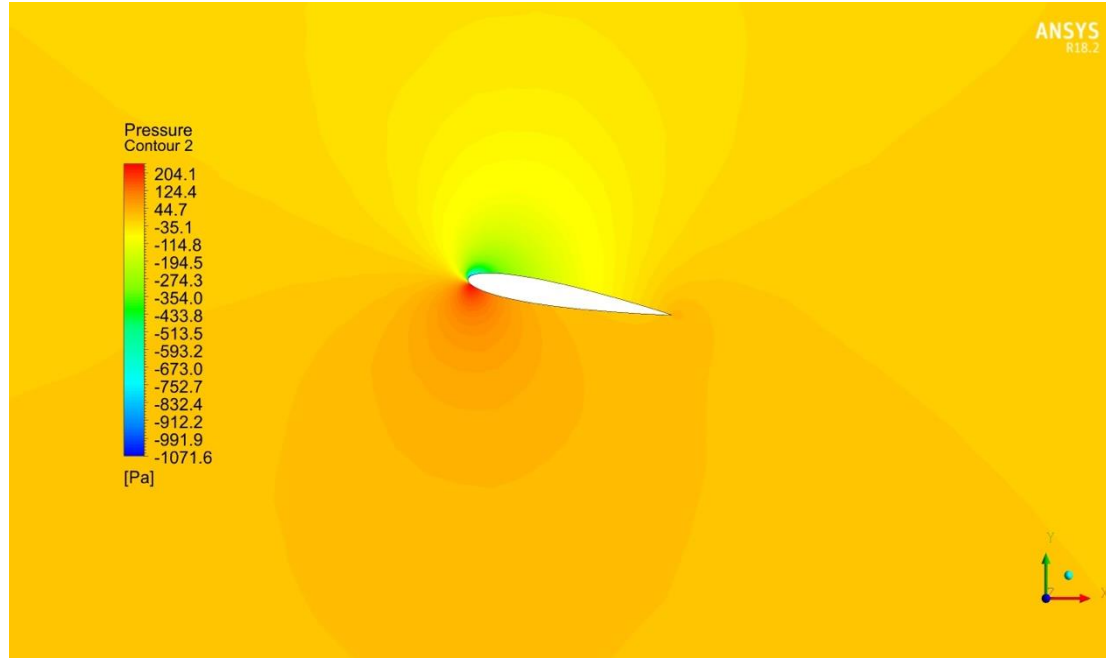


Fig. 5 The simulation results of the pressure on airfoil [NACA 0012].

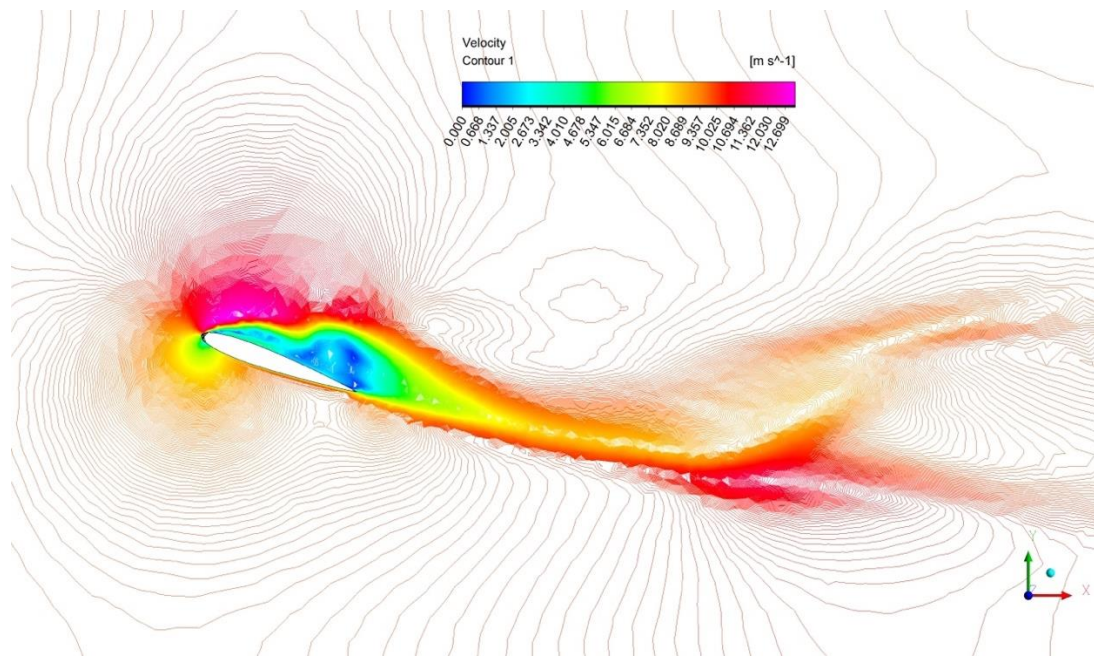


Fig. 6 The simulation results of the velocity on airfoil [NACA 0012].

From such distributions in Figure 5, one could deduce that the pressure on the lower surface is higher than which on the upper surface, which explains the lift force on an airfoil with the existence of angle of attack. Similarly, with the estimation of velocity distribution, one could observe a vortex that exists on the upper surface of the airfoil, in which velocity value is approximately zero indicating the drift-away of the boundary layer.

As introduced in the preceding chapter, there are lift, drag, and the moment on the airfoil when encountered free stream flow (Figure 3). These mechanical variables are denoted by dimensionless coefficients C_L , C_D , C_M , respectively. They correlate to the angle of attack (α), and Reynold's number (Re). The relations of these mechanical coefficients to α and Re is shown in diagrams (Figure 7).

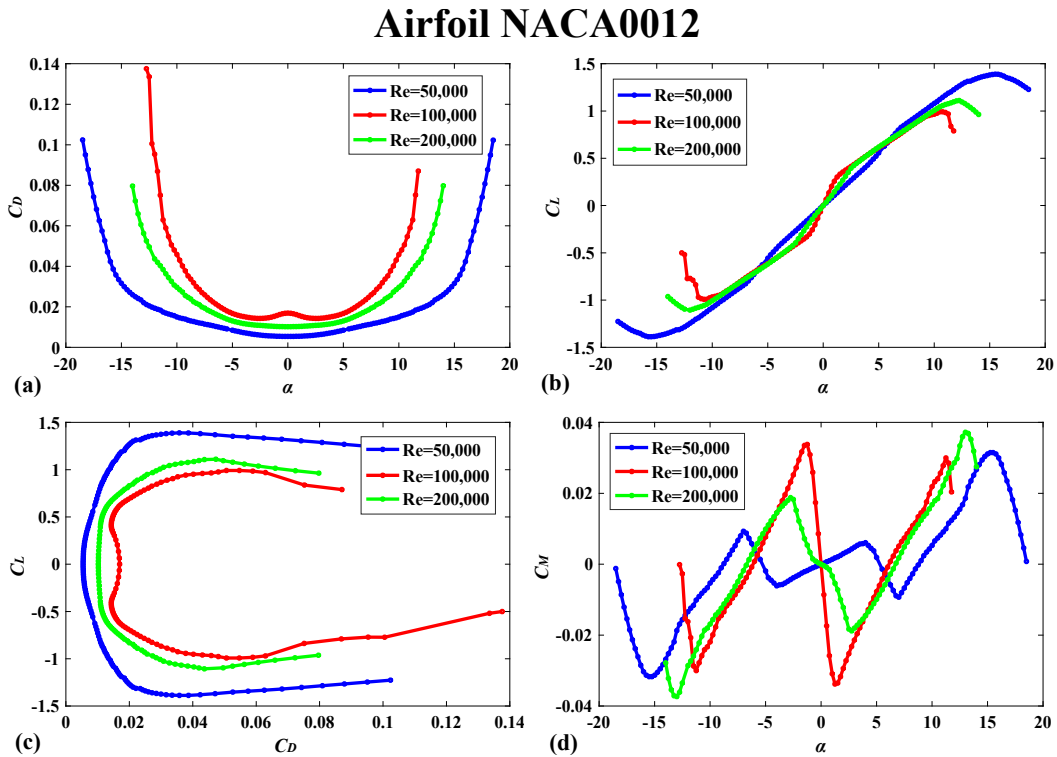


Fig. 7 Mechanical distribution of the airfoil [NACA 0012]. (a) The α - C_D diagram. (b) The α - C_L diagram. (c) The C_D - C_L diagram. (d) The α - C_M diagram. In which α is the angle of attack, C_D is the drag coefficient, C_L is the lift coefficient, C_M is the moment coefficient.

From Figure 7 one can observe that NACA 0012 mechanical coefficients generally have a complicated relation to α and Re . The drag coefficient is the highest when $Re = 100,000$ compared to applied Re . The coefficients fluctuate with no clear positive or negative correlation presented.

Decision Tree

Based on the Gini index as mentioned (Equation 4). The decision tree judging the dataset with the sound pressure value of 0 and 1 can be obtained through the given algorithm and presented as schematic as shown in Figure 8.

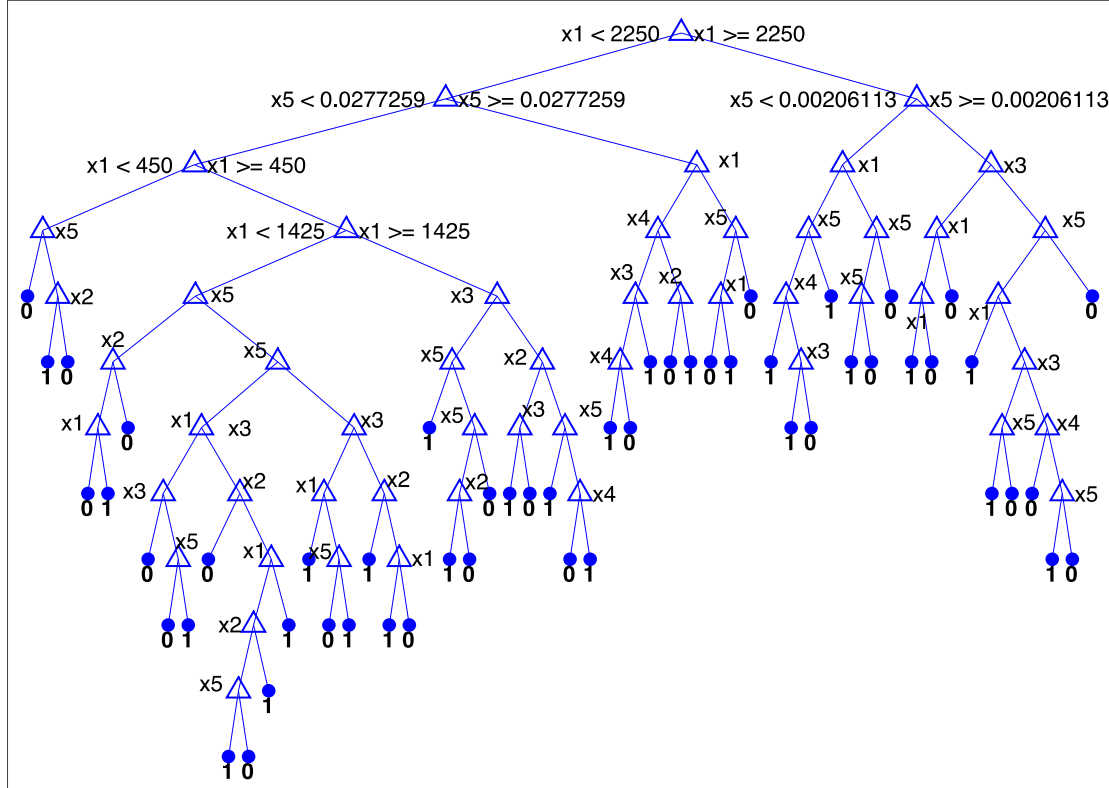


Fig. 8 Schematic view for the decision tree calculated from the dataset.

The presented schematic view shows how the attributes in the dataset help us assess the value of the sound pressure (0 and 1), in which x_1, x_2, \dots, x_5 represents the attributes of Frequency, Angle of Attack, ..., Suction displacement, respectively. The decision tree also indicates that a robust correlation of the attributes in the dataset as the generally numerous branches.

Linear Regression

As presented (Equation 13) we already attain the relation between the input data attributes and the sound pressure (noise), a linear regression model could be built with the algorithms as presented in Figure 9. As shown in the figure the model could be simplified as an equation: $y = 151.563x$, in which x contains information of the tested variables.

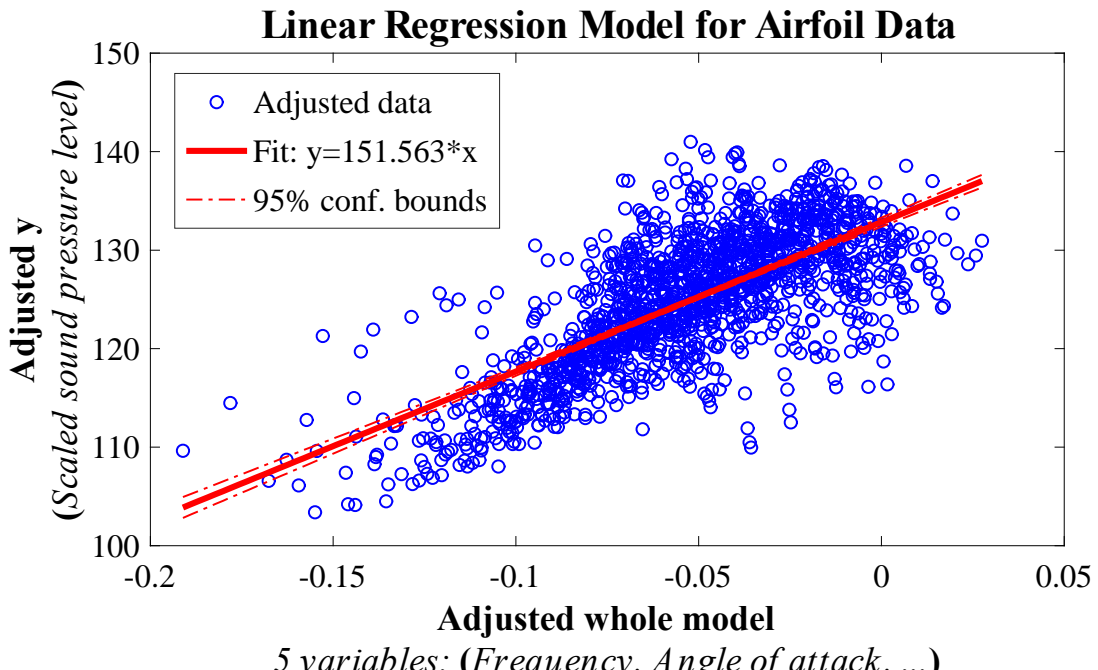


Fig. 9 Fitting diagram of linear regression model fitted for airfoil dataset.

Based on the algorithms, we can build two linear regression models of the dataset. One is a perfectly linear model as shown in Table 1, in which the relation of the five variables to the sound scaled pressure is perfectly linear. In the table the variables x_1, x_2, \dots, x_5 represents the attributes of Frequency, Angle of Attack, ..., Suction displacement, respectively.

Linear regression model: $y \sim 1 + x_1 + x_2 + x_3 + x_4 + x_5$

	Estimate	SE	tStat	pValue
(Intercept)	132.833805778378	0.544700692398831	243.865681891069	0
x_1	-0.00128220710890557	4.21054737495061e-05	-30.4522665279502	6.42181698991263e-159
x_2	-0.421911705948041	0.0388960909748539	-10.8471492989052	1.92337642119333e-26
x_3	-35.6880012257975	1.63043191185934	-21.8886792917952	2.28683899975858e-92
x_4	0.0998540448518054	0.00813225943082764	12.2787579148398	4.34063619837972e-33
x_5	-147.30051877787	15.0146684410392	-9.81044099350586	4.61724441831751e-22

Tab. 2 Calculation results for linear regression model fitted for airfoil dataset.

Based on the parameters shown in Table 1, one get the linear model of the scaled sound pressure representing in equation:

$$P_{sound} = -1.28 \times 10^{-3}\nu - 4.22 \times 10^{-1}\alpha - 35.69l + 9.99 \times 10^{-2}\nu - 1.47 \times 10^2\delta$$

In which v is the Frequency, α is the angle of attack, l is the Chord length, v is the Free-stream velocity, δ is the Suction side displacement thickness; P_{sound} is the Scaled sound pressure level.

Howbeit as shown before (Figure 4) one can deduce that the relation of the variables to the sound pressure is more complex than perfectly linear. Thence we implemented a coupled linear regression model.

Linear regression model: $y \sim 1 + x_2 + x_1 \cdot x_3 + x_1 \cdot x_5 + x_3 \cdot x_4 + x_4 \cdot x_5$

	Estimate	SE	tStat	pValue
(Intercept)	131.107551175829	0.83173887119001	157.630664764107	0
x1	-0.000207045198598631	6.57024552883535e-05	-3.15125511961396	0.00165798968352487
x2	-0.263028545763508	0.0348685726211137	-7.54342739009164	7.91349422142312e-14
x3	-26.5717945260154	4.15373708361991	-6.39708146931113	2.11398122204992e-10
x4	0.0393744358643762	0.0152452412749828	2.58273615708457	0.00989645186584277
x5	-147.282535654558	30.7278529952379	-4.79312810033891	1.8056401215327e-06
x1:x3	-0.00507495827908918	0.000354198419409863	-14.328009389609	1.00696658701296e-43
x1:x5	-0.0669843797917566	0.00406323583715607	-16.4854767176498	3.17903990160932e-56
x3:x4	0.244926722625617	0.0777389551739563	3.15063049249305	0.00166151544042849
x4:x5	2.09267395321099	0.555892284068762	3.7645313906752	0.000173330833429639

Tab. 3 Calculation results for optimized linear regression model fitted for airfoil dataset.

Based on such the equation could be written as:

$$P_{sound} = 1 - 0.26\alpha - 5.07 \times 10^{-3}vl - 6.70 \times 10^{-2}v\delta + 2.45 \times 10^{-1}lv + 2.09v\delta$$

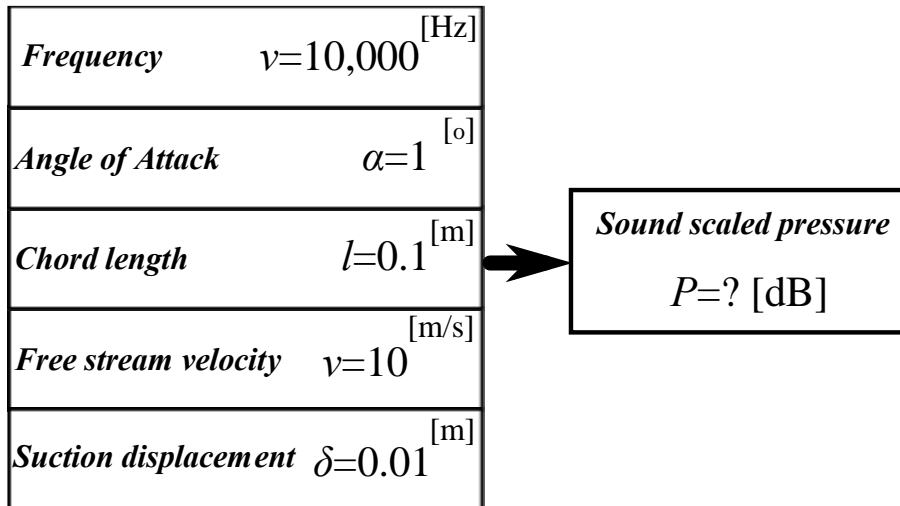
In which v is the Frequency, α is the angle of attack, l is the Chord length, v is the Free-stream velocity, δ is the Suction side displacement thickness; P_{sound} is the Scaled sound pressure level.

Noise Prediction

Therefore, as the model obtained, we could implement tested data to predict the noise of airfoil NACA 0012. With regard to the range of data in the trained dataset, I set a group of data to predict the possible noise with existed input data.

When implemented on the obtained decision tree (Figure 8), distinguished by the attributes' data of x_1 , x_3 and x_5 (Frequency, Chord length, Suction displacement), we

obtain the final judgement of x5 (Sound pressure) is 0. Hence, we can conclude the noise of such data is below the mean value, which is $P_{sound} \leq 125.721$ [dB].



Tab. 4 The process of obtained the predicted sound noise of airfoil NACA 0012.

When implemented such data on perfect linear regression (Equation 16) one obtain $P_{sound} = 115.5466$ [dB]. The coupled linear regression (Equation 17) one obtain $P_{sound} = 137.7693$ [dB]. The predicted noise of the coupled linear regression does not correlate with the decision tree judgement, which indicate that errors exists in the coupled linear tree and the accuracy is not high with the input data.

Conclusion

NACA 0012 is a classical airfoil (Figure 1) created by NASA (Figure 2) used for research in the field of fluid mechanics. The airfoil will take lift, drag forces and moment undergoing free stream velocity (Figure 3). The mechanical distribution on the airfoil could be investigated through decent simulations (Figure 5 and Figure 6) and the drag, lift and moment coefficients with their relations to angle of attack and Reynolds's number could be presented in diagrams (Figure 7).

Specifically, the free flow interacting with the airfoil will generate noise that can be represented by the sound scaled pressure. The mechanism behind such interaction is complex and there are hardly widely accepted equations representing such relation. Notwithstanding with the application of machine learning, which including decision tree (Equation 1-Equation 5) and linear regression (Equation 6-Equation 15) we could discern such relation. An experimental dataset containing information of NACA 0012 related mechanical variables and sound pressure is implemented for the algorithms

(Table 1, Figure 4). With the application of decision tree algorithm, a schematic diagram of the decision tree could be obtained (Figure 8). Plus, the perfectly and coupled linear regression model is presented as given (Table 2, Table 3, Equation 16, Equation 17). Based on such results, we can implement a set of testing data to predict the possible value of the sound pressure. When inputting a set of data containing certain values of mechanical variables (Table 4), we obtain the predicted level of noise from decision tree is 0, which mean it below the mean value ($P_{sound} \leq 125.721$ [dB]). With the application of perfectly linear model, the predicted sound scaled pressure is $P_{sound} = 115.5466$ [dB]. The predicted sound pressure for coupled linear regression model is $P_{sound} = 137.7693$ [dB].

Discussion

The mechanism of the airfoil's noise is still complex and yet to be depicted by detailed equations. Howbeit, we present a possible application of noise prediction by inputting the airfoil mechanical data. Albeit errors more or less existed as distortions shown in the results of the decision tree and coupled linear regression model, the method still provide an approximate scale of the noise generated by the airfoil. The pedigree of the noise includes shift-away of the boundary layer, vortex collision, etc. These phenomena are arduous to be depicted by equations when they are coupled with each other.

In fine, the presented methodologies could provide guidelines and decent insights for manufacturing and designation of airfoil, further, plane wing.

Acknowledgements

The airfoil's dataset [NACA0012] implemented for linear regression and the decision tree training is obtained from UCI Machine Learning Repository from Dr. Roberto Lopez [Dua ,D. et al 2019]. The simulation of airfoil NACA 0012 is generated from B. Liang and the contribution of the modelling is greatly acknowledged.

References

- [1] Dua, D. and Graff, C. (2019). UCI Machine Learning Repository [<http://archive.ics.uci.edu/ml>]. Irvine, CA: University of California, School of Information and Computer Science.

- [2] Antonio Fazzolari, Dott. in Fisica. An aero-structure adjoint formulation for efficient multidisciplinary wing Optimization. Conference Paper · January 2005. Datum der Promotion (Tag der mdl. Prüfung): 12.12.2005.
- [3] D. Funda Kurtulus, Alain Farcy, Nafiz Alemdaroglu. Unsteady Aerodynamics of Flapping Airfoil in Hovering Flight at Low Reynolds Numbers · January 2005. DOI: 10.2514/6.2005-1356
- [4] A.R. Davari, M.R. Soltani, F. Askari, H.R. Pajuhande. Effects of wing geometry on wing-body-tail interference in subsonic flow. *Scientia Iranica B* (2011) 18 (3), 407–415. doi:10.1016/j.scient.2011.05.031
- [5] Hui Liang, Xijun Wang, Li Zou, Zhi Zong. Numerical study of two-dimensional heaving airfoils in ground effect. *Journal of Fluids and Structures* 48 (2014) 188–202. dx.doi.org/10.1016/j.jfluidstructs.2014.02.009
- [6] W.R. Graham, C.A. Hall, M. Vera Morales, The potential of future aircraft technology for noise and pollutant emissions reduction, *Transport Policy*, Volume 34,2014,Pages 36-51,ISSN 0967-070X
- [7] J.H.S. Fincham, M.I. Friswell. Aerodynamic optimisation of a camber morphing aerofoil. *Aerospace Science and Technology* 43 (2015) 245–255. dx.doi.org/10.1016/j.ast.2015.02.023
- [8] Wang, Xiaole, et al. Reduction of aircraft engine noise by covering surface acoustic metamaterials on sidewalls[C]. Proceedings of the 24th International Congress on Sound and Vibration (ICSV), London, UK. 2017.
- [9] Yunpeng Qin ,Peiqing Liu,Qiulin Qua,Tianxiang Hua.Wing/canard interference of a close-coupled canard configuration in static ground effect .*Aerospace Science and Technology*.DOI: <http://dx.doi.org/10.1016/j.ast.2017.06.012>
- [10] Johan Boutet, Grigoris Dimitriadis. Unsteady Lifting Line Theory Using the Wagner Function for the Aerodynamic and Aeroelastic Modeling of 3D Wings. *Aerospace* 2018, 5, 92. doi:10.3390/aerospace5030092
- [11] Nathanael J. Curiale, David W. Zingg. Morphing Wings: A Study Using Aerodynamic Shape Optimization. AIAA 2018-1910. Session: Aerodynamic Shape Optimization II. 7 Jan 2018 doi.org/10.2514/6.2018-1910.
- [12] Sun J Q , Xiong F R , Schütze, Oliver, et al. Multi-objective Optimal Airfoil Design[J]. Cell Mapping Methods. 2019, 10.1007/978-981-13-0457-6(Chapter 12): 191-202.
- [13] T Rajesh Senthil Kumar, Sivakumar Venugopal, Balajee Ramakrishnananda, S. Vijay. Aerodynamic Performance Estimation of Camber Morphing Airfoils for Small Unmanned Aerial Vehicle. *J. Aerosp. Technol. Manag.*, São José dos Campos, v12, e1420, 2020.

- [14] D. Durante,E. Rossi,A. Colagrossi.Bifurcations and chaos transition of the flow over an airfoil at low Reynolds number varying the angle of attack. Journal Pre-proof .DOI: <https://doi.org/10.1016/j.cnsns.2020.105285>
- [15] Lorenzo Battisti, Luca Zanne 4, Marco Raciti Castelli .", Alessandro Bianchinib, Alessandra BrighentiC.A generalized method to extend airfoil polars over the full range of angles of attack .Renewable Energy. DOI: <https://doi.org/10.1016/j.renene.2020.03.15>
- [16] Li Yong,Wang Xunnian,Zhang Dejiu .Control strategies for aircraft airframe noise reduction.Chinese Journal of Aeronautics. DOI:<http://dx.doi.org/10.1016/j.cja.2013.02.001>
- [17] Suwin Sleesongsom, Sujin Bureerat. Aerodynamic Reduced-Order Modeling without Static Correction Requirement Based on Body Vortices. Article in Journal of Engineering. April 2013. DOI: 10.1155/2013/326496
- [18] Antonio Filippone, Aircraft noise prediction, Progress in Aerospace Sciences, Volume 68, 2014, Pages 27-63,ISSN 0376-0421
- [19] Antonio Filippone, Options for aircraft noise reduction on arrival and landing, Aerospace Science and Technology, Volume 60, 2017, Pages 31-38, ISSN 1270-9638
- [20] Misol, Malte. Experiments on noise reduction in aircraft with active sidewall panels[C]. Proceedings of the 25th International Congress on Sound and Vibration (ICSV), Hiroshima, JP. 2018.
- [21] Heininen, Arttu, et al. Equations of State in Fighter Aircraft Oleo-pneumatic Shock Absorber Modelling[C]. FT2019. Proceedings of the 10th Aerospace Technology Congress, October 8-9, 2019, Stockholm, Sweden. No. 162. Linköping University Electronic Press,
- [22] T.F. Brooks, D.S. Pope, and A.M. Marcolini. Airfoil self-noise and prediction. Technical report, NASA RP-1218, July 1989.
- [23] K. Lau. A neural networks approach for aerofoil noise prediction. Masterâ€™s thesis, Department of Aeronautics. Imperial College of Science, Technology and Medicine (London, United Kingdom), 2006.
- [24] R. Lopez. Neural Networks for Variational Problems in Engineering. PhD Thesis, Technical University of Catalonia, 2008.
- [25] NACA Airfoil. Wikipedia.
- [26] NACA 0012 AIRFOILS (n0012-il). AirfoilTools.

SECTION VI

An optimized algorithm for the prediction of the water emptying time on BPNN

H. Zhai[†], K. Wang[‡], Z. Liu[¶]

[†] *Department of Mechanics, School of Mechanics and Engineering Science, Shanghai University, Shanghai, PRC*

[‡] *Process Equipment and Control Engineering, College of Energy Engineering, Zhejiang University, Zhejiang, PRC*

[¶] *Mechanical Engineering, School of Mechanical Engineering, Zhejiang University, Zhejiang, PRC*

Abstract

The water discharge problem is a classic fluid mechanics problem yet hard to resolve due to its complex nature involves water-air interactions that generate air bubbles and vortex. Here, we analytically show that for water discharge in a square pipe, the water emptying time is quadratically proportional to water height and pipe length, and the solution is distributed on a “solution surface” in the $t - h - l$ space. Also, we found out that the water emptying time is shorter with bigger angles, and the water discharge rate is the highest for the Nongfu spring bottle and lowest for the Pocalri bottle. We explain such by bottle shape, depicted by the bottleneck shape and bottle-body trough. We qualitatively show that with a bottle shape depicted by $n > 1$ with our equation, or with a trough on the bottle-body, there is more likely to generate vortex and friction to slow the discharge. For what is more, the bottle-body trough plays a major in our approach. Inspired by the preceding approaches to solving fluid mechanics problems with machine learning, specifically using neural networks, we build a regression model based on our experimental data of the water discharge with BPNN to obtain the satisfied network through a strategy we called “Lucky-Draw”. We obtain that for our data the best BPNN parameters are: $\xi = 1$ and $\alpha = 10^{-3}$. Henceforth, we generate the satiated network with our algorithm shows good accuracy. We also implement a randomly generated dataset to get a prediction from our network.

Keywords: fluid mechanics; water discharge problem; BPNN; machine learning

Introduction

The water discharge is a phenomenon that is rather common in our daily life and a classic fluid mechanics problem. Such a problem, while may seems simple and common, is difficult to resolve due to its complex essence. The two-phase flow of water and air involves slippery water-air interactions and inter-surface contact, which requires a complicated mathematical model [1]. Therefore, a purely analytical approach is time-consuming and inefficient. For what is more, preliminary experimental approaches are more widely adopted for students to investigate [2] and statistical estimation of the experimental data could provide a valuable message as to elucidate the water discharge mechanism [3]. The process of explaining such problem with experimental approaches is presented as examples for analysis by H. Mayer [4], who coupled with the experimental data with the traditional mathematical model and contends that the water emptying time is positively proportional to bottle volume, maximum diameter, bottle height and negatively proportional to neck diameter, which is similar to out approaches.

However, with the fast-growing technology, due to its efficiency and viability, simulation is a more widespread approach nowadays, especially for fluid mechanics problems. As mentioned in the previous paragraph, the two-phase flow is a knotty issue engaged in the water discharge, while Liu *et al.* [5] present a CFD approach for the macroscopic water discharge for the flood. For what is more, the numerical approach also elucidated that the specific bottle dropping water discharge problems involves a generation of an air bubble between in the bottleneck area, the pressure around such area is wavy with time and the fluctuation is more intense with the bigger bottle outlet diameter [6]. Furthermore, the air bubble involved is one of the most important characteristics in the water discharge problem, as studied both from the dynamical perspective and the vibrational perspective ([7], [8]). Subsequently, other approaches such as image estimation with high speed camera is also implemented in investigating such a problem and provide valuable information about how the air bubble evolves [9].

Aside from the analytical, experimental, numerical, and image approaches, currently, machine learning is widely adopted in the study of fluid mechanics. Specifically, neural networks are especially suitable for studying complex fluid mechanics problems to reveal the mechanisms beneath the complex experimental data. In 1989, the NASA scientists already provide a feasible approach using an algorithm to predict the noise of a NACA airfoil as a regression model [10]. Later on, in the 21st century, neural network approaches have been implemented on the same database and all generate satiated results ([11], [12]).

Inspired by such exciting and promising results, we implement the neural networks approaches on the water discharge problem, to see whether we can obtain satisfying results as presented with the traditional approaches. Our basic strategy is to consider the water discharge experimental data as a regression model, in which the bottle's parameters and angles are input data and the water emptying rate is the output data. We implement a BPNN with

our algorithms and predict the water emptying time compared with our experimental data to check the accuracy.

Method

2.1 Problem formulation

As discussed in §0, the water discharge problem is a classic fluid mechanics yet rarely studied in modern scientific researches. The problem, while may seem simple and rather common in daily life, considering the complex two-phase fluid interaction and the interfacial problems involved between water and air, the problem is intricate and even difficult for simulations. Hence, a new strategy is being adopted, coupling statistics with fluid mechanics knowledge, one could discern certain scientific nature with the experimental approach.

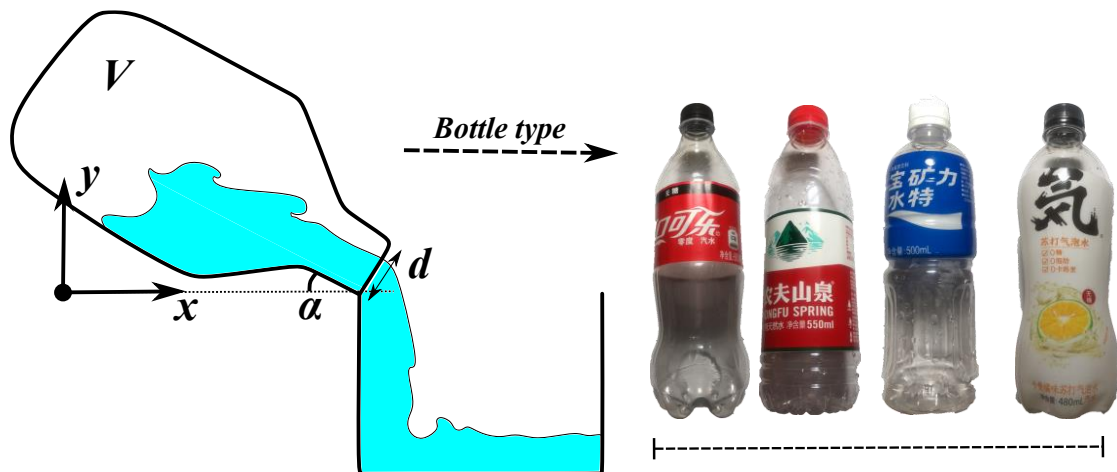


Fig. 1 Schematic illustration for the water discharge problem and the experimental method. Note that the bottles are named coke, Nongfu spring, Pocalri, soda bottle, from left to right.



Fig. 2 Picture for the experimental setup.

The schematic view for the experiments is shown as in Fig. 1, in which we change four different types of bottles having different bottleneck diameter, volume, and shape; changing tilted angles, one could obtain different water emptying time. Here, we measure the time with the same parameter (i.e. angle, diameter, volume, etc.) for ten sets to increase the accuracy as possible. Note that the angles are set to be at three values, i.e. 30, 45, 60, in degrees.

Here, we present a picture showing how we approach the experiment in Fig. 2. In the process, we control the angle with specific rulers and anchor the lower part of the bottle with our hands. We measure the emptying time when water started to drop out of the bottle and measured ten times with the same groups of parameters. The data is recorded matched with each's corresponding parameters.

2.2 Mathematical model

Here, we try to present a way to obtain the analytical solution as a simplified model for the water discharging problem. Now we consider a horizontal bottle as shown in Fig. 3, with a square cross-section of side length a . Provided that the water is flowing out at a steady-state and the water-air interaction is neglected.

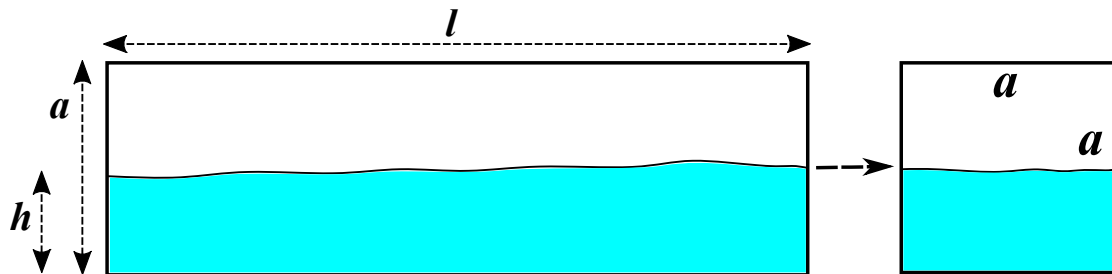


Fig. 3 Schematic view for the water flow problem, in assumed conditions.

Now let us consider the momentum and the flow volume of the water:

$$\left\{ \rho g \frac{h}{2} \cdot ah \cdot dt = dm \cdot V = ah dx \rho \cdot \frac{dx}{dt} \right. \quad (1)$$

$$\left. dQ = dh \cdot l \cdot a = ah \cdot dx \right. \quad (2)$$

Where $dx = \frac{dh l}{h}$ in (2).

Substitute such into Eq. 1:

$$\frac{gh}{2} = \frac{dx \cdot dx}{dt \cdot dt} \quad (3)$$

Which can be reduced to

$$\sqrt{\frac{gh}{2}} = \frac{dx}{dt} = \frac{l dh}{h dt} \quad (4)$$

Hence, one can deduce the water discharge time:

$$dt = \frac{ldh}{h} \sqrt{\frac{2}{gh}} \quad (5)$$

Here, we integrate Eq. 5, the water emptying time can thence be calculated as

$$\int dt = \int \frac{1}{h} \sqrt{\frac{2}{gh}} dh \quad (6)$$

Thence, the emptying time is obtained:

$$t = -2 \sqrt{\frac{2}{g}} l h^{-\frac{1}{2}} + C \quad (7)$$

Where C is an indeterminate constant.

Based on our analytical solution (Eq. 7), we can provide a visualization as shown in Fig. 4. Although the model is greatly reduced and based on very special conditions, the solutions can still provide decent guidelines for our estimation of the water discharge problem.

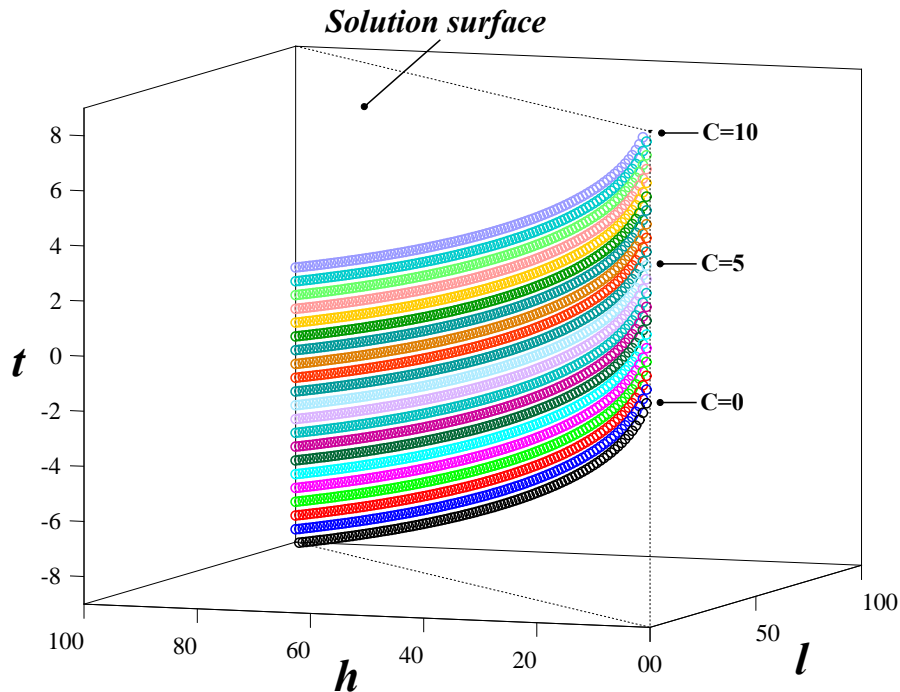


Fig. 4 Visualization of the analytical solution corresponding water emptying time with length and water height.

As it is shown in Fig. 4, in the solution space $(t - h - l)$, all the solutions are concentrated on a surface that I nominated “Solution surface”. The height and length are linearly proportional to each other; the emptying time has a quadratic relation with water height and length. For what is more, as the constant changes, the solution “steepness” or shape is not changed in the solution surface.

2.3 Algorithm approach

As mentioned in §2.1, we adopted an experimental method obtaining a $[12 \times 4]$ database. Notwithstanding, as given in the latter chapter §3.1, the water bottleneck’s shape and bottle-body’s trough also may influence the water discharge rate. Hence, we consider such two attributes as: if water bottleneck shape function parameter $n > 1$, then the value is 1, else 0; if water bottle-body has a trough, then the value is 0, else 1. Henceforth, we expand the database to $[12 \times 6]$.

Estimating the database one can discern that the calculation of the water emptying time can be regarded as a regression model, in which the input data involves 5 sets: bottle type, bottle volume, ... as shown in Fig. 5. The water emptying time is calculated as the mean value.

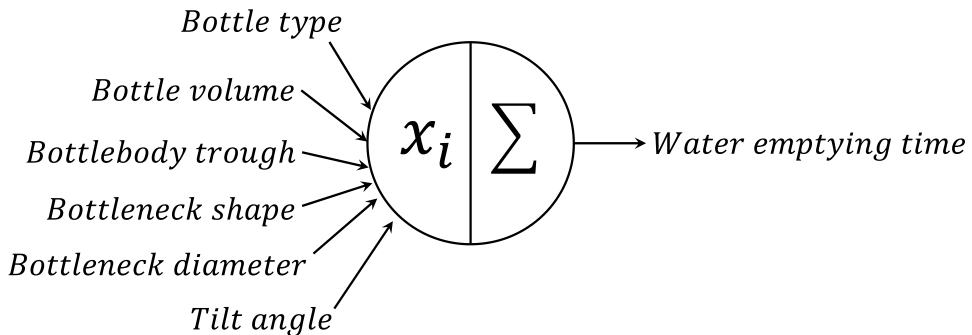


Fig. 5 Illustration for the regression problem based on the experimental data.

There are various ways of building a regression model and providing solutions. The simplest one is a linear regression model. However, considering the relatively few data and the complex nature of such a problem as mentioned in §2.1, such a model might not provide accurate predictions. Here, we provide a neural network method, for the prediction of the water emptying time. A simple BPNN parameter deciding process is shown as in Algorithm 1.

As shown beyond, Algorithm 1 gives an approach of finding the best neuron numbers ζ and learning rate α , which are the two parameters that might greatly influence the network’s performance, for the generation of the neural network with best efficiency and accuracy.

Algorithm 1: Determining the Parameters of Original BPNN

Set the initial value of sum of the determining factor $R_{\text{sum}}^2 = 0$; and sum of the relative error $\varepsilon_{\text{sum}} = 0$.

For a loop running with 10^3 iterations:

Clear all the remaining values of the last iteration;

1: Importing and operating the data.

2: Generate the network:

Change the specific parameters:

i. Set the neuron numbers $\xi \rightarrow$ change from 1 to 20.

ii. Set the training epochs $= 10^5$.

iii. Set the training goals $= 10^{-3}$.

iv. Set the learning rate $\alpha \rightarrow$ change from 10^{-1} to 10^{-5} .

Training the data with given parameters and creating simulation.

3: Calculate the results:

The sum of determining factor $R_{\text{sum}}^2 = R_{\text{sum}}^2 + R^2$, the sum of the relative error $\varepsilon_{\text{sum}} = \varepsilon_{\text{sum}} + \varepsilon$.

The mean value of R^2 and ε is calculated by $\frac{R_{\text{sum}}^2}{\text{Iterations}}$, $\frac{\varepsilon_{\text{sum}}}{\text{Iterations}}$.

Calculate the CPU running time t_{run}

End the loop.

Algorithm 2: Obtain the BPNN model

For a loop running with 10^5 iterations:

Clear all the remaining values of the last iteration;

1: Operating the data:

Import the water discharge experimental data to define the input and output data, and set the training and testing sets.

Normalize the input dataset.

2: Generate the network:

Set the given parameters obtained from Algorithm 1.

Training the data with given parameters and creating simulation.

3: Calculate the results:

Obtaining errors and deciding parameter R^2 ;

Outputs the results as comparing the testing data and simulation results, and calculate the relative error ε .

4: Generate a condition to break the loop:

If a value of R^2 that beyond 0.95 is detected, then plot the errors distribution and break the loop.

End the loop.

After obtaining the best parameters that fit the data for the BPNN with the highest performance, we need to generate the network satisfies our standard ($R^2 > 0.95$) as shown in Algorithm 2. Hence, we create a loop with a large circulation number (10^5 in our approach) to find such a condition. When the condition is detected, the loop is break and the results are obtained, which we nominate as “Lucky-Draw”. Note that the calculation is carried out by

Lenovo ThinkPad E480 with CPU: intel CORE i5 8th Gen. The code is running in MATLAB R2017A with system: Windows 10.

Results and discussion

3.1 Experimental estimation

Based on experimental operations as given in §2.1, we obtain results as shown in the following figures. To show the range and deviation of the datasets, we plotted the graphs as the form of a boxplot.

Here in Fig. 6, one observes that for the coke bottle, as the angle increases, the water emptying time evidently reduced. For what is more, the deviation is larger for the angle of 60, in degrees. Such results indicate that for the coke bottle, larger angles give a more discretized data distribution. This may cause by the air bubble or air-water interactions in an increasing steepness. While it also may cause by the specific shape of the coke bottle.

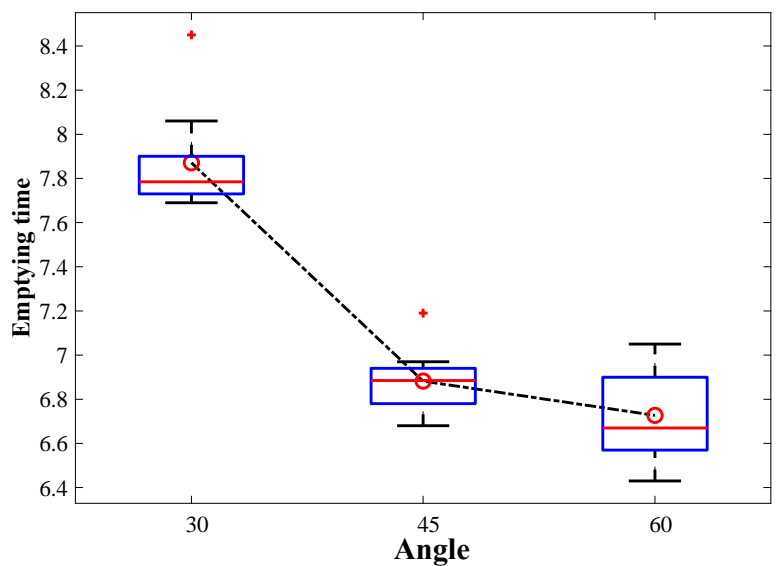


Fig. 6 The Emptying time-angle boxplot diagram of the coke bottle.

However, the same nature does not apply to the Pocalri bottle or the soda bottle as shown in Fig. 7 and Fig. 8. As shown, for Pocalri and soda bottle the emptying time does not show an evidently higher deviation with larger angles. Moreover, the error distribution does not increase eminently with bigger angles. Such results could be explained by the specific shape of the Pocalri and soda bottle. Notably, the emptying time dropping patterns both follows an approximately linear mode for Pocalri and soda bottle (Fig. 7 and Fig. 8), yet dropping either slower or faster for coke bottle and Nongfu spring (Fig. 6 and Fig. 9).

But if we neglect the emptying time dropping patterns, the data distribution is very similar for coke and Nongfu spring bottle. Both have an eminently higher deviation with the increasing angles, and both have a larger error bar with the increasing angles (Fig. 6 and Fig. 9).

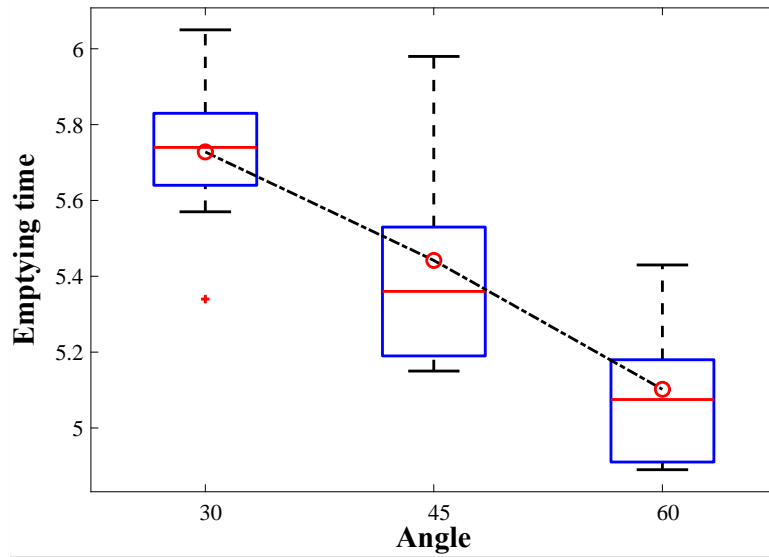


Fig. 7 The Emptying time-angle boxplot diagram of the Pocalri bottle.

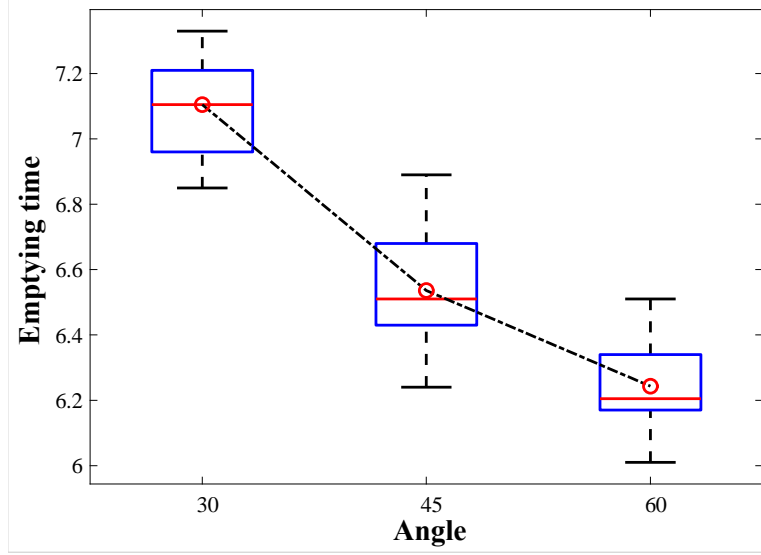


Fig. 8 The Emptying time-angle boxplot diagram of the soda bottle.

From the previous discussions, we know that the bottle shape may play an important role in determining the water emptying time. To investigate such, we need to obviate the effect of the bottle volume difference. Henceforth, we define water discharge rate τ as the division of the water emptying time t to bottle volume V :

$$\tau = \frac{V}{t} \quad (8)$$

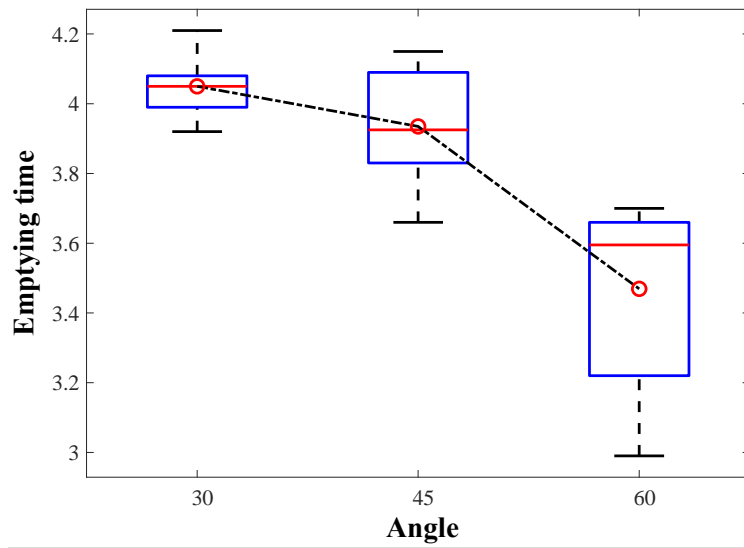


Fig. 9 The Emptying time-angle boxplot diagram of the Nongfu spring bottle.

Here, Fig. 10 shows us how angle affects the water discharge rate for different types of bottles. From the relations, the water discharge rate is positively correlated with the angle. Notwithstanding, the Nongfu spring bottle has an evidently larger discharge rate than other types of bottles as shown. The Pocalri bottle has the least discharge rate comparing with others.

The bottle shape could provide guidelines for the explanation of such a discharge rate difference, which is shown in Fig. 11 and Fig. 12.

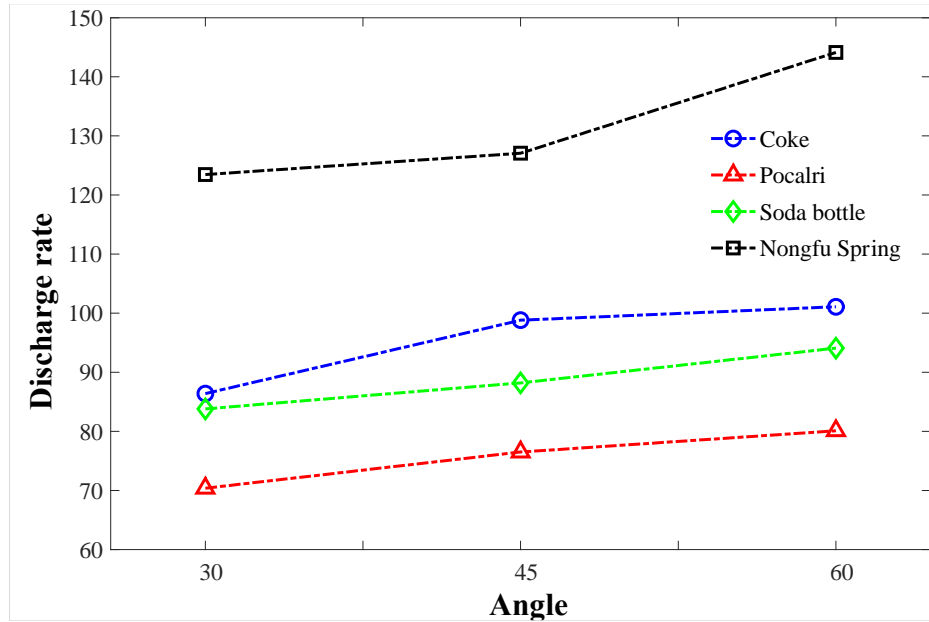


Fig. 10 The discharging rate calculated as a mean value comparing the four bottles.

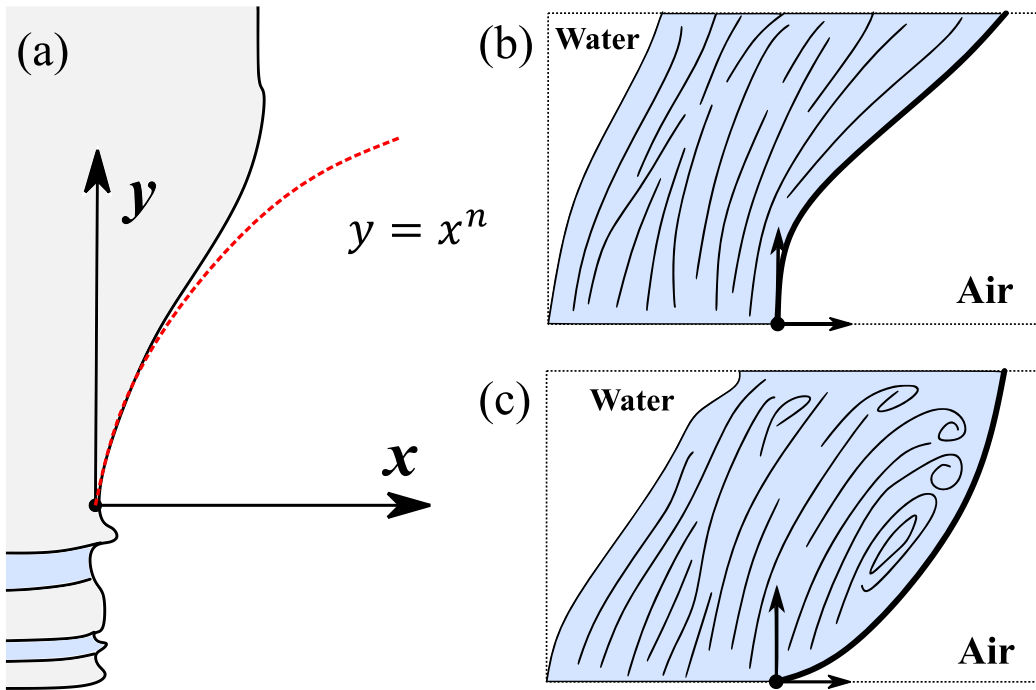


Fig. 11 Schematic of the provided explanation of the water discharge rate considering the bottleneck shape. (a) Basic strategy for mathematical description of the bottle shape. (b) The schematic of water emptying process when $n < 1$. (c) The schematic of water emptying process when $n > 1$.

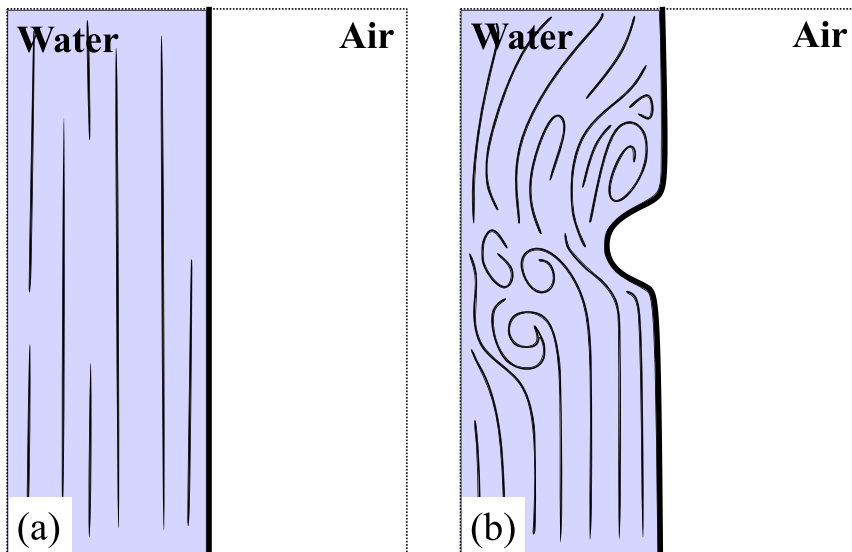


Fig. 12 Schematic of the provided explanation of the water discharge rate considering the bottle-body shape. (b) The schematic of water emptying process when the bottle-body has no trough. (b) The schematic of water emptying process when the bottle-body has a trough.

In our studies, we try to depict that bottle shape with two main factors, the bottleneck shape and bottle-body trough. For the bottleneck shape, we try to delineate such with a function $y = x^n$ as shown in Fig. 11. When $n > 1$, the bottle shape is shown as in Fig. 11, which is correlated with the bottle shape of coke. Such a shape indicates a smoother flow, or, with less vortex or flow friction due to its streamlined shape. When $n < 1$, the bottle shape is

shown as in Fig. 11, where there is a larger possibility for flow to generate vortex and friction with the bottle inner surface. Such an effect might dissipate the energy and slow the water dropping process. The preceding theory might provide an explanation for the coke bottle has a higher discharge rate than Polcari and soda bottle. Yet the evidently higher discharge rate of Nongfu spring is not elucidated.

Observing the four bottle types, we find that both bottles have an evident trough on the bottle-body except the Nongfu spring. The bottle-body trough can create flow vortex and generate friction as shown in Fig. 12. Such a theory could explain why the Nongfu spring bottle has the highest water discharge rate. Moreover, coupled with experiments, we know that the bottle-body trough plays a more important role in influencing the water discharge rate.

Applied with the preceding theories, we could also explain why the Pocalri bottle has the lowest water discharge rate: the bottleneck shape could be depicted by $n > 1$ and has a larger n value than the other bottles. Such a shape generates vortex or even air bubbles that will robustly slow the discharge rate. For what is more, it has some trough on the bottle-body. Both characteristics will slow their discharge process. For the Nongfu spring bottle, although it does not have a streamline-like bottleneck shape as coke does, its smooth bottle-body explains its fast discharge rate compared with the trough-shaped bottle-body of a coke bottle.

3.2 BPNN algorithm

Running the Algorithm 1, with the set learning rate 10^{-2} [2:iv], from the process [Step 2:i], we obtain how the neuron numbers ξ will influence the neural network's performance as shown in Fig. 13, Fig. 14, and Fig. 15.

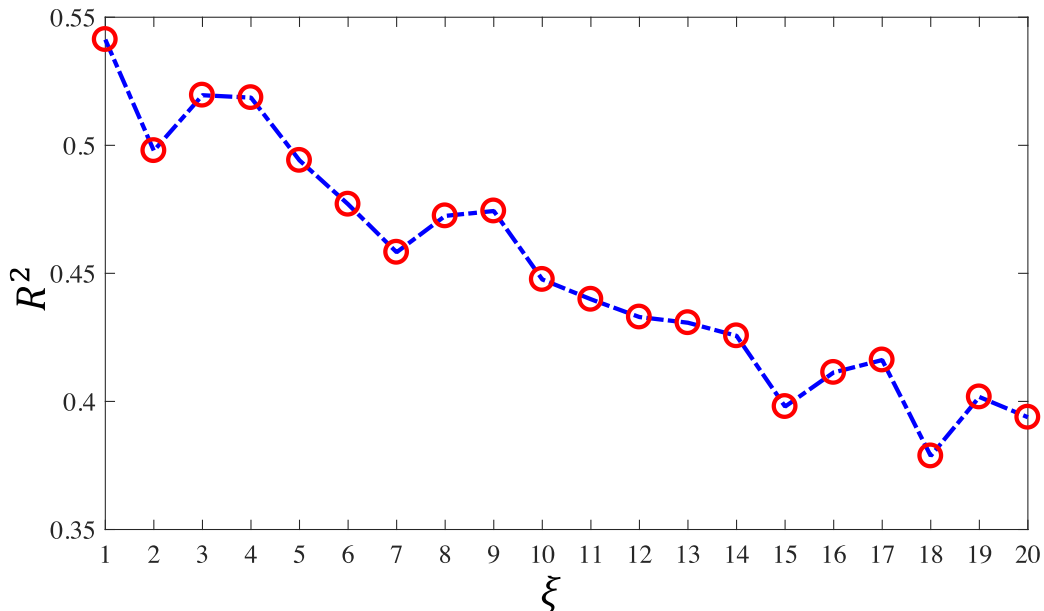


Fig. 13 The relations between the neuron numbers ξ to determining factor R^2 .

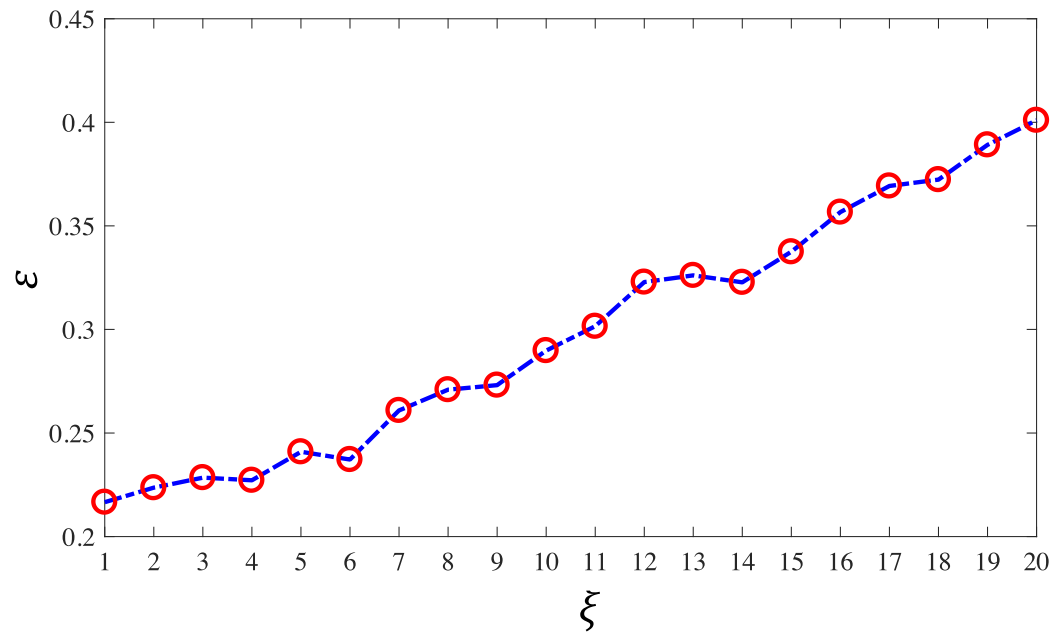


Fig. 14 The relations between the neuron numbers ξ to relative error ε .

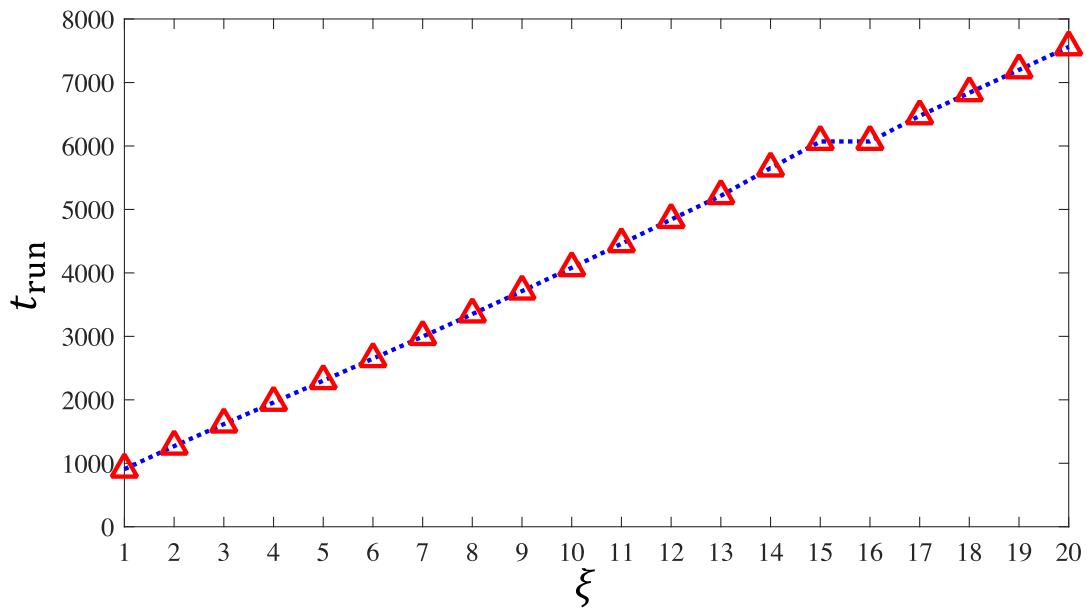


Fig. 15 The relations between the neuron numbers ξ to CPU time t_{run} .

Given that the equation for the determining factor R^2 :

$$R^2 = \frac{\sum T_{\text{sim}} \cdot T_{\text{test}} - \frac{(\sum T_{\text{sim}} \cdot \sum T_{\text{test}})^2}{(N \cdot \sum (T_{\text{sim}})^2 - (\sum T_{\text{sim}})^2) \cdot (N \cdot \sum (T_{\text{test}})^2 - (\sum T_{\text{test}})^2)}}{(9)$$

Where N is the size of the input testing data matrix, T_{sim} is the simulation results, T_{test} is the testing samples.

The relative error ε is calculated as:

$$\varepsilon = \frac{\|T_{sim} - T_{test}\|}{T_{test}} \quad (10)$$

From the running results, we observe that when the neuron number $\xi = 1$ we obtain the neural network that has the biggest determining factor values (R^2), smallest relative error values (ε), and the least CPU running time (t_{run}), which is identified as the best neural network performance. Such a result does not match with our past experience of neural network training. We attribute such specific behavior to the small scale of the database. To be specific, due to we only have four types of bottle and three sets angle values, 12 sets is the most data that we can obtain from the longitudinal scale (Rows).

Following a similar strategy, given the neurons $\xi = 1$, we also run Algorithm 1 [2:iv] to determine the best learning rate α and obtain results as shown in Fig. 16 and Fig. 17.

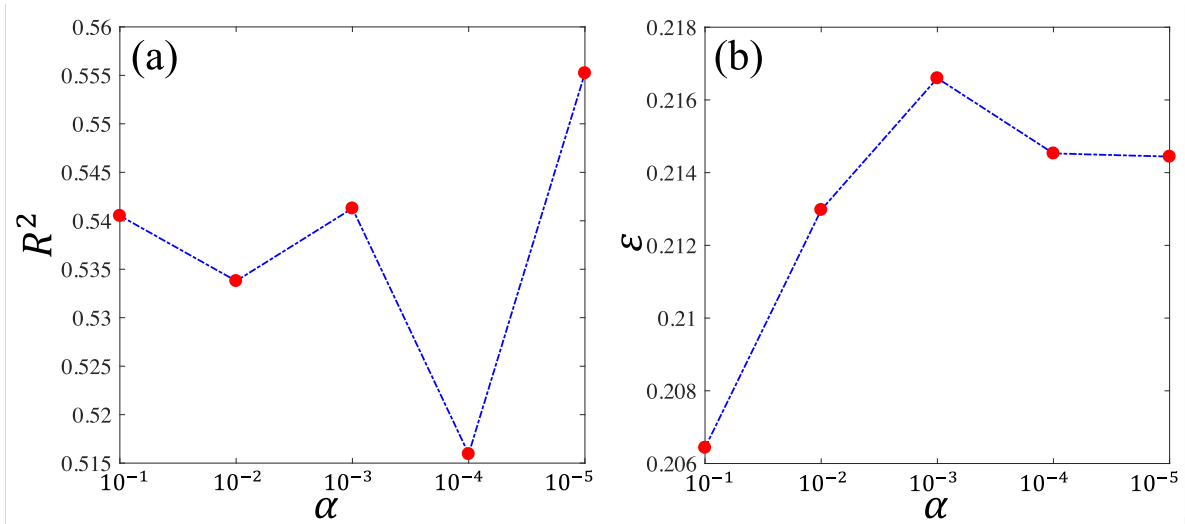


Fig. 16 The learning rate α effect on the network's performance. (a) The learning rate (α) – determining factor (R^2) diagram. (b) The learning rate (α) – relative error (ε) diagram.

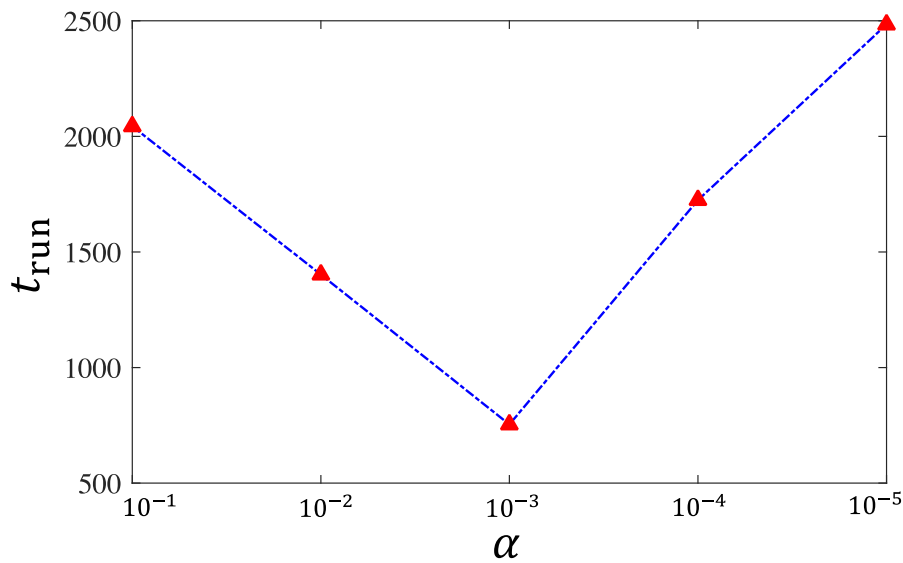
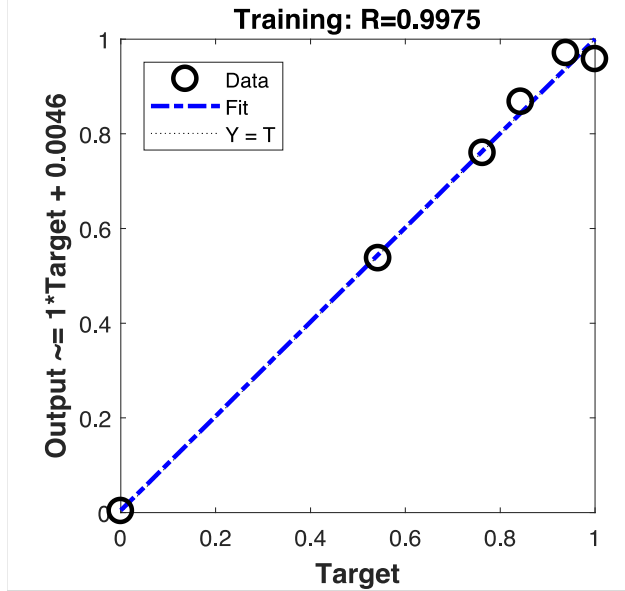
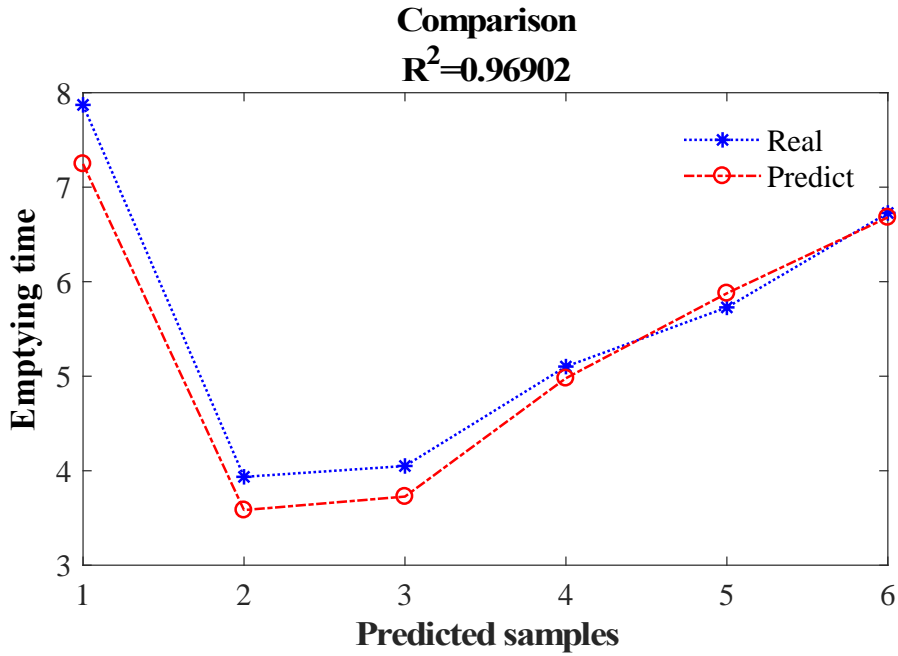


Fig. 17 The relations between the learning rate α to CPU time t_{run} .

From Fig. 16 we observe that both the determining factor R^2 and the relative error ε does not indicate a specific learning rate. Yet Fig. 17 indicates that when $\alpha = 10^{-3}$ we obtain the smallest CPU running time t_{run} . Such a phenomenon indicate that $\alpha = 10^{-3}$ generate a network that has a better performance.

Set the parameters $\xi = 1$ and $\alpha = 10^{-3}$, we now run Algorithm 2 to obtain the desired neural network, the results is shown in Fig. 18, Fig. 19, and Fig. 20.

**Fig. 18** The regression model of the generated network.**Fig. 19** The comparison between the testing samples T_{test} and the neural network's simulation results T_{sim} .

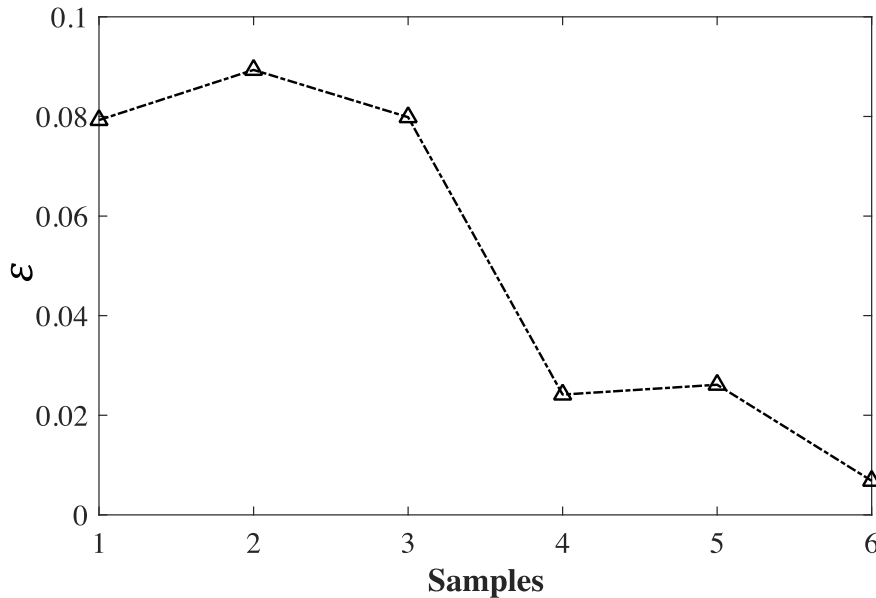


Fig. 20 The distribution of the relative errors ϵ with the testing samples.

Both Fig. 18 and Fig. 19 shows that the obtained neural network has valid performance, with determining factor $R^2 = 0.96902$ and small relative errors $\epsilon < 0.1$. Here, we also provide an example: A Pocalri bottle with Bottleneck diameter: 2.5 cm; Volume: 500mL; Bottleneck shape: $n > 1$ with a bottle-body trough; with tilted angle 45°. The predicted water emptying time: 3.2541s.

Conclusion

We investigate the water discharge problem three approaches, creating an experiment, and qualitatively estimate the experimental data, providing an analytical mathematical solution, and implement the experimental data on a BPNN model to predict water emptying time-based on our experimental parameters. We design experiments with two controlled parameters for the study: bottle type and angles as shown in Fig. 1, note that involve various parameters involved in bottle types. The bottle's body is anchored by rulers and hand as shown in Fig. 2. Subsequently, we present a water discharge mathematical model of a square pipe (Fig. 3). With the equation of momentum and the flow equation we reason out an analytical solution, pointing out that time is quadratically proportion to height and length, while the solution is distributed on a “solution surface” in the $t - h - l$ space as shown in Fig. 4. As introduced in §0, we consider the experimental database as a regression model, in which a schematic is shown in Fig. 5. To build such a model with the BPNN method, we provide two algorithms as shown in Algorithm 1 and Algorithm 2.

Experimentally we visualize our data of the water emptying time with regards to angles for four bottles as shown from Fig. 6 to Fig. 9. Such results show that both the bottles have shorter emptying time with larger angles. Howbeit for coke and Nongfu spring bottle, with larger angles, the data deviation is evidently larger with larger error bars (Fig. 6 and Fig. 9);

yet such a pattern does not apply to Pocalri and soda bottle (Fig. 7 and Fig. 8). When we investigate the bottle shape effect on water discharge, we need to neglect the bottle volume, as we calculate the water discharge rate to depict the water dropping speed as shown in Eq. 8. Results indicate that the Nongfu spring bottle has the highest water discharge rate and the Pocalri bottle has the lowest. To explain such a phenomenon, we try to depict the bottle with two characteristics: the bottleneck shape and bottle-body trough. The bottleneck shape is depicted by $y = x^n$ as shown in Fig. 11. Qualitative analysis shows that with a $n > 1$ bottleneck shape water is more likely to be slowed when discharging (Fig. 11) and with a body trough water discharge are more likely to be slowed due to the vortex and friction (Fig. 12).

With the implementation of the Algorithm 1 of BPNN, we found out that for the experimental data, it is most efficient to take neuron numbers $\xi = 1$ (Fig. 13, Fig. 14, Fig. 15) and learning rate $\alpha = 10^{-3}$ (Fig. 16, Fig. 17) comparing the determining factor, relative error, and the CPU time of the neural network. With specified parameters, we run the BPNN model with Algorithm 2 and obtain the satiated network. Our obtained NN indicates good fitting (Fig. 18), acceptable accuracy with $R^2 = 0.96902$ and $\varepsilon < 0.1$ (Fig. 19 and Fig. 20). For what is more, as we input a randomly generated samples, we obtain a prediction from the network.

Our works applying BPNN with a small set of data are just preliminary approaches of combining machine learning with fluid mechanics, future works may involve optimization of the BPNN with the implementation of a bigger database.

Acknowledgement

The authors would like to thank R. Alam, W. Liang, S. Tan, and D. Kong for the valuable discussions and insightful suggestions.

References

- [1] P. B. Whalley. Flooding, slugging and bottle emptying. *Int. J. Multiphase Flow* **13**(5), 723 (1987).
- [2] Chunyang Ding. An Increasing Flow of Knowledge: Investigating Torricelli's Law, or the Effect of Height on Flow Rate. Physics Internal Assessment: Experiment Report. May 2014.
- [3] C. I. Ossai. Pump-off identification with time series analysis of transient water T discharge rate. *Journal of Petroleum Science and Engineering* **181** (2019) 106203
- [4] H. Mayer. Bottle Emptying: A Fluid Mechanics and Measurements Exercise for Engineering Undergraduate Students. *Fluids* **2019**, 4, 183
- [5] G. Liu, F. Tong, B. Tian, J. Gong. Finite element analysis of flood discharge atomization based on water-air two-phase flow. *Applied Mathematical Modelling* **81** (2020) 473–486.

- [6] F. Geiger, K. Velten, and F.-J. Methner. 3D CFD simulation of bottle emptying processes. *J. Food Eng.* **109**(3), 609 (2012).
- [7] C. Clanet and G. Searby. On the glug-glug of ideal bottles. *J. Fluid Mech.* **510**, 145 (2004).
- [8] G. B. Deane and H. Czerski. A mechanism stimulating sound production from air bubbles released from a nozzle. *J. Acoust. Soc. Am.* **123**(6), EL126 (2008).
- [9] L. Rohilla, A. K. Das. Fluidics in an emptying bottle during breaking and making of interacting interfaces. *Phys. Fluids* **32**, 042102 (2020).
- [10] T.F. Brooks, D.S. Pope, and A.M. Marcolini. Airfoil self-noise and prediction. Technical report, NASA RP-1218, July 1989.
- [11] K. Lau. A neural networks approach for aerofoil noise prediction. Masterâ€™s thesis, Department of Aeronautics. Imperial College of Science, Technology and Medicine (London, United Kingdom), 2006.
- [12] R. Lopez. Neural Networks for Variational Problems in Engineering. PhD Thesis, Technical University of Catalonia, 2008.

Authorship contribution statement

H. Zhai contributes to drafting the manuscript, providing the algorithms (BPNN) and conceive the results; K. Wang contributes to designing and carrying out the experiments; Z. Liu contributes to providing the analytical solution and carrying out the experiments.

Appendix. Code, data and supplementary materials

The code including Algorithm 1 and Algorithm 2, the raw and the operated database, and other related materials is uploaded on <https://github.com/hanfengzhai/WaterDischargeNN>.